Structure-based analysis and evolution of a monomerized red-colored chromoprotein from the *Olindias formosa* jellyfish for bioimaging

By

Zhai Le

March 2023

A thesis submitted to
graduate school of frontier biosciences
Osaka university for
the degree of
Doctor of Philosophy
Academic year 2022

ABSTRACT

GFP-like chromoproteins (CPs) with non-fluorescence ability have been used as bioimaging probes. Existing CPs have blanks in the optical absorbing window, which limiting their extensibility. To cope with this situation CPs with new color are required. Previously, Nagai laboratory cloned CPs from the jellyfish, *Olindias formosa*, and developed a completely non-fluorescent monomeric red CP, R-Velour, with an absorption peak at 528 nm. To analyze the photophysical properties from a structural aspect, I determined the crystal structure of R-Velour at a 2.1 Å resolution. R-Velour has a *trans*-chromophore similar to Gamillus, a green fluorescence protein (GFP) derived from the same jellyfish. However, in contrast to the two coplanar chromophoric rings in Gamillus, R-Velour has a large torsion inducing non-fluorescence property. Through site-directed mutagenesis, I surveyed residues surrounding the chromophore and found a key residue, Ser155, which contributes to the generation of four-color variants with the bathochromic and hypsochromic shift of the absorption peak, ranging from 506 to 554 nm. Based on the recently proposed spectrum shift theory, I explained the spectrum shift with the difference in the state of the hydrogen bonds from the chromophore phenolate oxygen. That was further supported by disruption of the hydrogen bond in the new crystal structure of the variants M-Velour-554 with the bathochromic shift. To further expand the color palette of CP ranging from 420-480 nm, yellow CP dimTFPs and Y-Velour were successfully created under the mutagenesis study. And Y-Velour has been demonstrated as the best acceptor of Förster resonance energy transfer (FRET) to Sumire, a violet fluorescence protein (VFP) under the *in vitro* and cellular experiment by two-photon fluorescence lifetime imaging (FLIM). These findings may support further development of CP variants with useful absorption characteristics for bioimaging, including intensiometric FRET imaging, FLIM and photoacoustic imaging (PAI).

TABLE OF CONTENTS

LIST OF ABBREVIATIONS

Symbols/Abbreviations	Terms
ATP	Adenosine triphosphate
BFP	Blue fluorescence protein
B-GECO	Blue Genetically Encoded Ca2+ Indicators
CFP	Cyan fluorescence protein
Ca^{2+}	Calcium ion
CP	Chromoprotein
cDNA	complement DNA
DNA	deoxyribonucleic acid
DMEM/F12	Dulbeccco's modified Eagle's medium mixture F-12
E. coli	*Escherichia coli*
EC	Extinction coefficient
EDTA	Ethylenediaminetetraacetic acid
FBS	Fetal bovine serum
FP	Fluorescent protein
FI	Fluorescence intensity
FLIM	Fluorescence lifetime imaging microscopy
FRET	Förster resonance energy transfer
GFP	Green fluorescent protein
HEPES	4-(2-hydroxyethyl)-1-piperazineethanesulfonic acid
mTFP1	Monomeric teal fluorescence protein

NTA	Nitrilotriacetic acid
LED	Light emitting diode
OFP	Orange fluorescence protein
PAI	Photoacoustic imaging
PBS	Phosphate buffered saline solutions
PCR	Polymerase chain reaction
PEI	Polyethylenimine
QY	Quantum yield
REACh	Resonance Energy-Accepting Chromoprotein
R-Velour	Red GFP-like chromoprotein with very low quantum yield and visible color
RFP	Red fluorescence protein
ROI	Region of interest
SD	Standard deviation
SDS-PAGE	Sodium dodecyl sulfate–polyacrylamide gel electrophoresis
StEP	Staggered extension process
VFP	Violet fluorescence protein

CHAPTER 1
GENERAL INTRODUCTION

1.1 GFP-like non-fluorescent chromoprotein

The green fluorescent protein (GFP) present in *Aequorea victoria*, avGFP, was the first reported genetically encodable fluorescent tag for bioimaging. Since then, protein engineering of fluorescent proteins (FPs) has evolved markedly to modify their photophysical properties, resulting in diverse FP variants with notable features [1]. Non-fluorescent chromoproteins (CPs) homologous to FPs have also attracted attention. Owing to their high light absorption efficiency and non-fluorescence properties, CPs have been preferentially applied as an acceptor of genetically encoded indicators for FRET (Förster resonance energy transfer) imaging [2], FLIM (Fluorescence lifetime imaging microscopy)-based FRET [3,4], which requires only donor fluorescence for FRET detection [5]. Additionally, CPs have been applied to probes for PAI (Photoacoustic imaging) with deepening visualization depth in biological tissues compared to fluorescent imaging.

Currently reported CPs were either developed from CPs inherently existing in some organisms or were derived from FPs with reduced quantum yield through mutagenesis (Table 1). Inherent CPs derived from naturally existing *Anthozoa* exhibit yellow green to orange light absorption (560–610 nm), which is sufficiently long to develop red fluorescent proteins (RFPs) with longer emission in the visible light range [6]. The first report of cloned inherent CP was the anthozoan *Pocillopora damicornis*-derived pocilloporin in vivid pink color with two absorption peaks at 390 nm and 560 nm [7]. CPs from other anthozoan species were also reported, such as the vivid purple hcCP (λ_{max}= 578 nm) from *Heteractis crispa* [8], blue aeCP597 (λ_{max}= 597 nm) from *Actinia equina* [9], and blue cjBlue (λ_{max}= 610 nm) from *Cnidopus japonicus* [10]. Subsequently, blue CP Ultramarine derived from coral *Montipora efflorescens* was developed by introducing mutations for monomerization into the inherent CP Rtms5 (λ_{max}= 592 nm) [11]. The structure of the inherent CPs is composed of eleven-stranded β-barrel and two internal α-helices that embed the *trans*-chromophore with the same

topology as the FPs with β-barrel fold so-called β-can [10,12–14]. Generally, FPs adopt highly coplanar p-hydroxybenzylideneimidazolinone chromophore with *cis* or *trans* conformation, while the inherent CPs generally have a *trans*-chromophore. For instance, chromophores in the reported crystal structure of CPs, Rtms5 [12], cjBlue [10], sgBP from *Stichodactyla gigantea* [13], and shCP from *Stichidacyla haddoni* [14], adopted *trans* configuration. In the instance of the hcCP-derived far-red fluorescent mutant HcRed, chromophore in the X-ray structure contained two components *cis* coplanar and a *trans* non-coplanar chromophores suggesting the coexistence of the residual fluorescent *cis* coplanar chromophore of the hcCP in the non-fluorescent *trans* non-coplanar chromophore [15].

Additionally, regarding the CPs developed from the FPs, those with lower quantum yield (0.02 to 0.05), such as REACh (λ_{max}= 517 nm) [3], dimVenus (λ_{max}= 508 nm) [2,4], and darkmCherry (λ_{max}= 590 nm) [16] were developed from popular FPs for bioimaging: EYFP, Venus, and mCherry, respectively (Table 1). CPs with improved applicability to FLIM-FRET measurements have been developed by improvement from REACh. REACh was improved with regards to the expansion of the absorption optical window and further elimination of the residual fluorescence leading bleed-through into the fluorescence of the FRET donor. The color variants, ShadowG (λ_{max}= 486 nm) [17] and ShadowY (λ_{max}= 519 nm) [18], have been developed as acceptors of GFPs with much lower quantum yields (0.005 and 0.01, respectively) than parental REACh. ShadowR (λ_{max}= 585 nm) [19] was developed from Ultramarine as the FRET acceptor for RFPs. Non-specific interactions with cytosolic proteins that influence the localization of target proteins were also suppressed in ShadowR.

Table 1. List of photophysical properties of representative reported CPs

CPs	Orangnism	EC Ɛ ($M^{-1}cm^{-1}$) [a]	$\lambda_{max, abs}$ [b] (nm)	Φ[c]	Ref[d].
Pocilloporin	*Pocillopora damicornis*	No data	560 nm	No data	[7]

hcCP	*Heteractis crispa*	No data	578 nm	No data	[8]
aeCP597	*Actinia equina*	110,000	597 nm	＜0.001	[9]
cjBlue	*Cnidopus japonicus*	66,700	610 nm	＜0.001	[10]
Rtms5	*Montipora efflorescens*	80,000	592 nm	0.004	[11]
sgBP	*Stichodactyla gigantea*	122,000	608 nm	No data	[13]
shCP	*Stichidacyla haddoni*	No data	574 nm	No data	[14]
Ultramarine	*Montipora efforescens*	64,000	586 nm	0.001	[11]
dimVenus	Synthetic	55,400	508 nm	0.03	[2,4]
darkmCherry	Synthetic	79,000	590 nm	0.03	[16]
sREACH	Synthetic	115,000	517 nm	0.07	[18]
ShadowG	Synthetic	89,000	486 nm	0.005	[17]
ShadowY	Synthetic	136,000	519 nm	0.01	[18]
ShadowR	Synthetic	106,000	585 nm	＜0.001	[19]

[a]Molar extinction coefficient determined by alkali-denaturation method. (See 2.2 Materials and methods for more details)

[b]Maximum absorbance wavelength.

[c]Absolute fluorescence quantum yield measured by integrating sphere.

[d]References.

1.2 Application of CPs in Intensiometric FRET imaging, FLIM-FRET and PAI

1.2.1 Intensiometric FRET imaging

Imaging using the technique of FRET has been used extensively in the process of developing many kinds of genetically encoded fluorescent indicators [20]. The conventional approach for designing genetically encoded FRET-based indicators calls for two FPs with distinct excitation and emission wavelengths to serve as the donor and acceptor for FRET, as well as a sensor domain that detects a factor of interest, such as ions (e.g. Ca^{2+}, Mg^{2+}, K^{+} and H^{+}) [21–25], protease enzymes [26] or biological molecules (e.g. ATP) [27]. Upon excitation of the FP donor, the excited-state energy is transferred in different degrees to the acceptor, ultimately leading to the emission of fluorescence by the FRET pair. The longer the distance between the donor and the acceptor, the less this energy transfer efficiency becomes. The efficiency of FRET is depending on parameters such as donor-acceptor distance and relative orientation. If the conformation of the sensor domain alters in response to the detection of a factor, a change in distance or relative orientation is anticipated, resulting in a change in the fluorescence intensities of the donor and acceptor. Changes in the FRET efficiency are usually monitored through the donor-acceptor fluorescence intensity ratio images. The simple design of the FERT-based indicators composed of the donor and acceptor FPs interlinked with a sensing domain has high adaptivity for a wide variety of detection by replacing the sensing domain. Generally, the combination of CFP and YFP, with which high dynamic range indicators have been reported, is frequently used [28]. Alternative FRET pairings between GFP and RFP have been developed [5,29,30]. This pair has the merit of well-separated emission wavelength, which can prevent spectral contamination caused by the bleed-through of GFP fluorescence to the channel for RFP fluorescence.

CPs have been preferentially applied as acceptor or quencher for genetically encoded indicators in intensiometric FRET imaging, which acquires only donor fluorescence for FRET detection. This is because CPs have a high light absorption efficiency and are non-fluorescent. Photoactivatable Ca^{2+} indicators (PA-TNXL) have been shown to employ photoactivatable GFP (PA-GFP) as FRET donor and CP (a

YFP mutant with weak fluorescence, cp173DimVenus) as a FRET quencher, allowing for intensiometric FRET measurement (Table 2) [2]. In their study, a number of RFPs were first tried, all of which had only slight overlap in absorption and emission spectra with activated PA-GFP. Regrettably, however, all constructions responded rather weakly to Ca^{2+} response with good dynamic signal change. In addition, because all RFPs had extended absorption spectra into shorter wavelengths, RFP fused constructions exhibited weak fluorescence at red channel even before photoactivation of PA-GFP. To acquire an appropriate acceptor protein, quencher of CPs with high light absorption efficiency and non-fluorescent become the candidates for their selection.

1.2.2 FLIM-FRET

One of the applications by using CPs is FLIM-based FRET measurement (FLIM-FRET) (Table 2). FLIM imaging produces an image based on the differences in the excited state decay rate from a fluorescent sample. FLIM-FRET is applied to detect the intracellular protein-protein interaction [31]. GFP and RFP are frequently used as a pair of donor and acceptor in FLIM-FRET due to its well separated emission spectra [5,29,30]. One of the characteristics in FLIM-FRET is that it only detects the donor fluorescence, not the acceptor fluorescence. However, it is challenging to simultaneously use multiple FLIM-FRET FP pairs, since each FP pair with an emission spectra range of two FPs occupies a wide range of emission wavelengths. That means the number of targets events in a single cell that can be simultaneously monitored by the FPs-based FRET sensor is practically limited. FRET with the combination of FP donor and non-fluorescence CP acceptor is advantageous to narrow the emission for multicolor FLIM-FRET imaging. And there is no need for spectral separation between donor and acceptor fluorescence, which will be convenience and easy for the filter selection.

1.2.2 PAI

CPs have been applied to probes for PAI, enhancing visualization depth in biological tissues compared to fluorescent imaging (Table 2). The energy of light-

excited molecules release through nonradiative relaxation has the potency to increase intracellular local temperature and that causes pressure change resulting in the propagation of photoacoustic waves. PAI is a bioimaging technique that enables the visualization of optical absorbers inside biological tissues by monitoring the ultrasonic signal that is generated from the optical absorbers by light pulse irradiation [32]. CPs also show higher efficiency of photoacoustic signal generation due to the absence of radiative relaxation and significantly increased photostability [32,33].

PAI reporter genes can be classified as two categories. One is the genetic expression of enzymes, such as *β*-galactosidase, tyrosinase and violacein biosynthesis enzyme which can react with some of the endogenous agents and form a chromophore [34]. The newly synthesized chromophore inside the target group can be a source of the photoacoustic signal. The other is genetic expression of exogenous FPs and CPs as reporter genes which can generate photoacoustic signals under the certain light irradiation. This approach is well accepted by researchers, since the expression and generation of FPs and CPs are not limited by substrate availability and enzyme kinetics compared with enzymatic reporter genes [35].

EGFP and mCherry, specifically expressed in fruit fly and adult zebrafish, are the first FPs probes demonstrated in photoacoustic imaging in 2009·[36]. And near-infrared fluorescent protein, BphP iRFP713, also has been applied as probes in PAI in recent years [37–39]. However, the low photostability due to photobleaching and transient absorption effects is one of the drawbacks of FPs and BphP iRFP in photoacoustic imaging [40,41]. Furthermore, fluorescent emission with relatively high QY of FPs and BphP iRFP leads low PA signal generation efficiency which also hinder the probe development in PAI. Compared with FPs and BphP iRFP, CPs are advantageous candidates for photoacoustic imaging because of their high photostability, low QY and high photoacoustic signal generation efficiency [34]. Using ShadowG, ShadowY, and ShadowR, the Ishihara M Group at National Defense Medical College has recently demonstrated multicolor photoacoustic microscopic imaging of intracellularly expressed chromoproteins. They developed an optical-resolution photoacoustic microscopy using a supercontinuum light source. The multicolor imaging of multiple chromoproteins was performed with combination of bandpass filters under the stimulation of broadband supercontinuum light pulses [42].

Table 2. List of some CPs for intracellular applications

CPs	Source	Demonstrated applications	Ref.
dimVenus	Venus	Intensiometric photoactivatable Ca^{2+} indicators	[2,4]
ShadowG	sREACh	FLIM-FRET acceptor for GFP	[17]
ShadowY	sREACh	FLIM-FRET acceptor for GFP	[9]
darkmCherry	mCherry	FLIM-FRET acceptor for RFP	[16]
ShadowR	Ultramarine and mCherry	FLIM-FRET acceptor for RFP	[19]
E2-Crimson NF	*Discosoma striata*	Assessment of PAI Spectra and Photobleaching *in vitro*	[34]
aeCP597	*Actinia equina*	Assessment of PAI Spectra and Photobleaching *in vitro*	[34]
cjBlue	*Cnidopus japonicus*	1. Assessment of PAI Spectra and Photobleaching *in vitro*. 2. Using PAI as a screening tool, they identified a variant (cjBlue2) that has a PAI signal that is twice as strong as the original.	[33, 34]
Ultramarine	*Montipora efforescens*	1. Assessment of PAI Spectra and Photobleaching *in vitro*. 2. Evaluation of tdUltramarine2 as a FRET acceptor *in vitro* using PAI. 3. Ultramarine or tdUltramarine2 expressing *Escherichia coli* (*E. coli* cells, ~10^6 of them) were injected into rat ears, and *in vivo* imaging was performed under PAI	[11, 33]

Ref. stands for references.

1.3 3D structure of CP

For FP engineering, structural information obtained by crystal structure analysis has contributed to color-tuning [43], monomerization[44], enhancement of quantum yield[45], and the study of photoswitching mechanisms[46]. There are also reports in the literature investigating the conversion of CPs to FPs [14,47,48], such as fluorescent mutants of Rtms5 and shCP [48]. Moreover, strategy of color tuning for extending the color palette of FPs and CPs [13,43,49,50] based on their crystal structure has been previously reported. Therefore, understanding the structure information of the novel GFP-like protein in advance is one of the essential steps to improve the efficiency of protein engineering. Moreover, researchers have utilized crystal structures to explore the difference between FPs and CPs. For example, structural analysis for blue CP Rtms5 revealed its non-planar chromophore with *trans* configuration [12]. The composition of Rtm5 tripeptides chromophore (Gln-Try-Gly) is identical to that of the DsRed with well planar *cis* configuration (**Figure 1A**). In a conclusion, the chromophore in Rtms5 has the observably different in comparison with the DsRed chromophore despite the chemical structure of chromophore is being identical. A recent study on the acid tolerance GFP “Gamillus” with enhanced brightness revealed that Gamillus that Gamillus' chromophore hydroxyphenyl ring is in the *trans* configuration, while all previously published structures of GFPs show the *cis* configuration in the fluorescence state [51,52] (**Figure 1B**). Therefore, it might be reasonable to conclude that the planarity between FPs and CPs is a dominant characteristic difference to explain dim fluorescence of CPs.

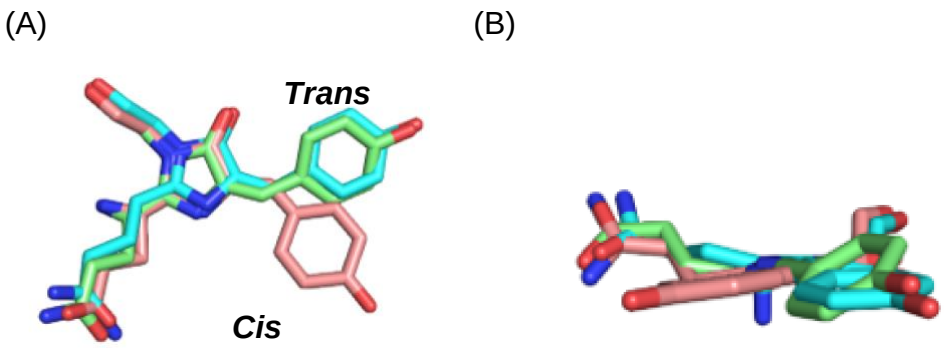

Figure 1. Molecular structure of DsRed, Rtms5 and Gamillus. (A) *Cis* conformation in DsRed (Pink; PDB:1G7K) chromophore and *trans* conformation in that of Rtms5 (Green; PDB: 3VK1) and Gamillus (Cyan; PDB: 5y00). **(B)** Well planar chromophore in Gamillus (Cyan; PDB: 5y00) and DsRed (Pink; PDB:1G7K) in comparison with non-planar chromophore in Rtms5 (Green, PDB: 3VK1). Chromophores are represented as a stick model.

CHAPTER 2

Structure-based analysis of a monomerized red-colored chromoprotein from the *Olindia formosa* jellyfish

2.1 Introduction

In the previous study, Shinoda H et al. investigated the FP expressed in the tentacles of the flower hat jellyfish, *Olindias formosa* [51,52]. Initially, the tentacle segments of the flower hat jellyfish were examined for the presence of unidentified GFP genes. These tentacle sections emit a strong green fluorescence. And they isolated FP from the green fluorescent section of the tentacles and developed a novel GFP, Gamillus with the enhanced brightness and acid-tolerance [51]. Non-fluorescent red-violet sections are also present at the distal portions of the green, fluorescent sections in the tentacles. Thus, we expected the existence of a new red-violet CP with the potential to expand the CP absorption spectrum window. An unidentified CP gene were cloned from the tentacle sections of the flower hat jellyfish, *Olindias formosa*, with red-violet color and no fluorescence. A synthetic cDNA library was constructed using the mRNA extracted from the excised red-violet section of the jellyfish tentacle and cloned into the bacterial expression vector. Among the ~450,000 colonies of *E. coli* expressing the library, one red-violet colony and three faint red colonies were isolated. The CP with the highest extinction coefficient in the purified solution was selected as a novel red non-fluorescent CP and was designated as “ofCP” for further study. The ofCP is composed of 229 amino acid residues and displays 49% and 42% amino acid sequence homology to dfGFP (origin of Gamillus) and anm2CP (origin of KillerRed), respectively. (The detailed of cDNA library screening method is in the core reference paper of my doctoral thesis [53]).

The photophysical properties were evaluated of *the E. coli* recombinant protein. The purified CP protein solution was red-violet in color, with no evident fluorescence under blue light irradiation. The optical absorption spectrum peak of ofCP at 528 nm was 24 nm longer than that of Gamillus. The molar extinction coefficient of ofCP at 94,000 mM^{-1} cm^{-1} was slightly larger than that of Gamillus (**Table 3**). Interestingly,

although both adopt the same chromophore tripeptide amino acid sequence, their optical properties differed. The undetectable quantum yield of ofCP implies its non-fluorescence emission property. The pH titration result indicated that ofCP was tolerant under weakly acidic physiological conditions (p*Ka* = 4.7), similar to that of Gamilllus (p*Ka* = 3.4) (**Table 3**). The result of the size-exclusion chromatography indicated that ofCP tended to dimerize at high concentration in the overexpressed condition of the recombinant proteins in *E. coli* or mammalian cells (**Figure 2d**). Homodimerization hinders the normal function of the target protein and occasionally hampers its subcellular localization [54]. To address this potential complication, ofCP was monomerized. As a result, the L154T mutation was introduced to reduce the hydrophobic interaction, as with the monomerization of Gamillus (**Figure 2A, B**). To restore the molar extinction coefficient, a DNA library was created by random mutagenesis and screened for bacterial colonies with the desired dark red-violet color. Subsequently, a secondary DNA library was generated from the screened variants by DNA shuffling using the staggered extension process (StEP). The monomeric ofCP2 with restored molar extinction coefficient (91,000 M^{-1} cm^{-1}) was successfully obtained (**Figure 2C, D**). I designated it as R-Velour abbreviated from "Red GFP-like chromoprotein with very low quantum yield and visible color". The unmeasurable level of quantum yield and peak absorption wavelength of CP were preserved in R-Velour. The weaker acid resistance of light absorption (pK_a = 4.8) than that of Gamillus was also preserved **(Table 3**). In this study, I determined 3D structure of R-Velour by X-ray crystallography and elucidated the photophysical differences with Gamillus, based on the crystal structures. Based on the structural information, Phe140 was considered a key factor influencing non-fluorescent properties. Replacement of Phe140 and its adjacent residue with other amino acids caused R-Velour to fluoresce.

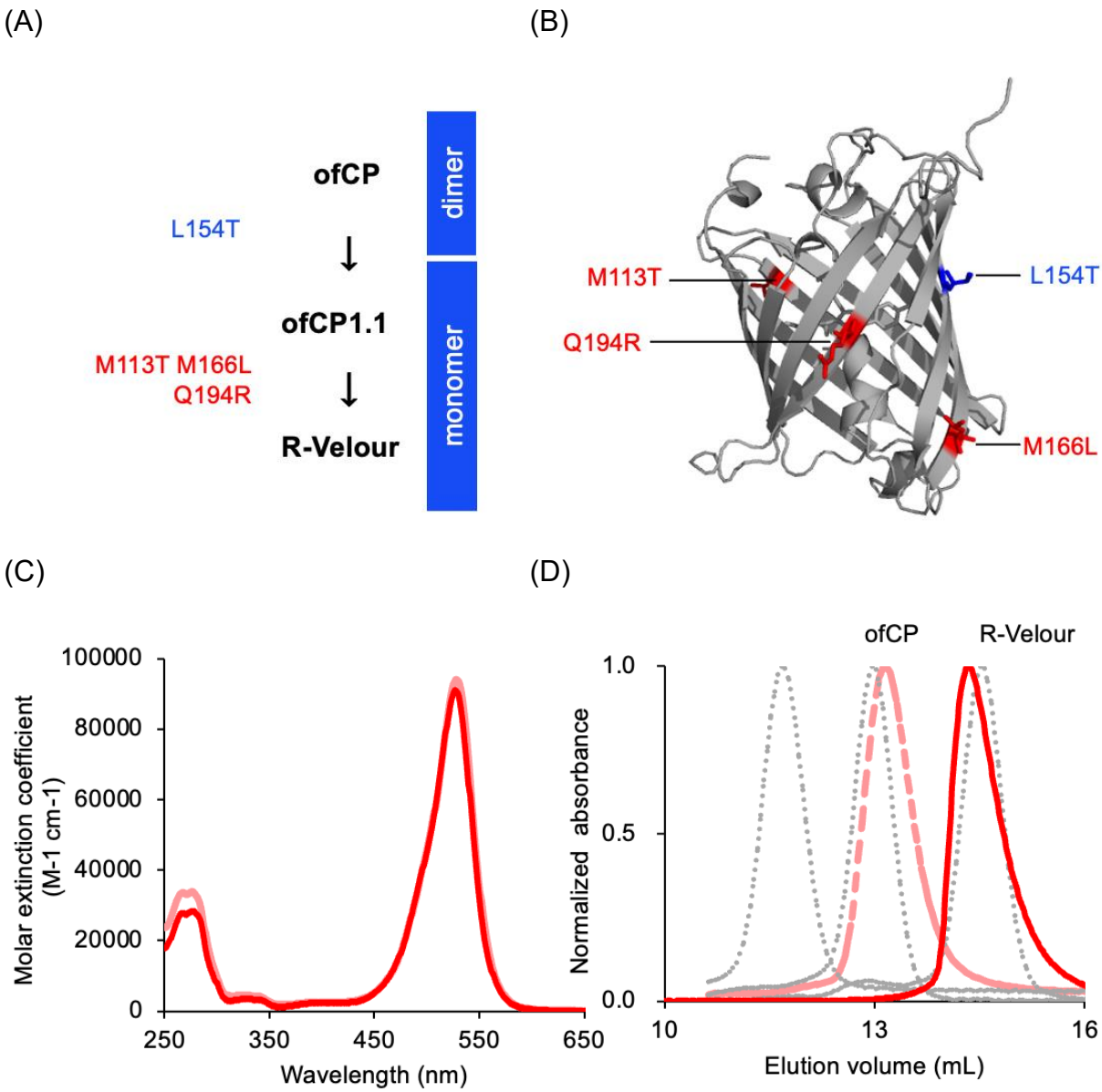

Figure. 2 Engineering of R-Velour from ofCP, and in vitro characterization of ofCP and R-Velour. (A) R-Velour lineage. **(B)** Positions of mutant amino acids during the directed evolution process were depicted on the X-ray crystal structure of R-Velour. The mutation for monomerization is represented in blue, and those for improved light absorption in red. **(C)** Molar extinction coefficient spectra of ofCP (rose dash line) and R-Velour (red solid line), measured at 30 μM, pH7.5 at 25°C. **(D)** Size-exclusion chromatography for protein oligomerization analysis of ofCP (rose dash line) and R-Velour (red solid line). The dash gray lines from left to right represent the standard curves of the tetramer (DsRed), the dimer (KillerRed), and the monomer (mCherry), respectively.

Table 3 Photophysical properties of ofCP, R-Velour, M-Velour-F and Gamillus

Protein	$\lambda_{max, abs}$[a] (nm)	λ_{ex} / λ_{em}[b] (nm)	ε[c] ($M^{-1}cm^{-1}$)	Φ[d]	pK_a[e]
ofCP	528	-	94,000	< 0.001	4.7
R-Velour	528	-	91,000	< 0.001	4.8
M-Velour-F	392, 532	502/518	39,000, 7,900	0.12	9.3
Gamillus	504	504/519	83,000	0.90	3.4

[a]Maximum absorbance wavelength.

[b]Excitation and emission peak wavelength.

[c]Molar extinction coefficient determined by alkali-denaturation method.

[d]Absolute fluorescence quantum yield determined by integrating sphere.

[e]pH at which absorption value becomes its half-maximal value.

2.2 Materials and methods

Phylogenetic analysis. Amino acid identification and similarity assessment of CP and R-Velour was performed using the BLAST server (https://blast.ncbi.nlm.nih.gov/Blast.cgi?PROGRAM=blastp&PAGE_TYPE=BlastSearch&LINK_LOC=blasthome). The sequence was aligned with hydrozoan FP sequences using the Clustal Omega online server, and sequence alignment graphics were generated using JalView software. The GenBank accession numbers for the aligned and sequence analyzed FPs are: dfGFP (**BBC28143**), Gamillus (**BBC28144**), anm2CP (**AAR85352**), and KillerRed (**AAY40168**).

Protein expression and purification. The gene encoding the CPs was inserted into the pRSET$_B$ vector, which is a plasmid vector for high protein expression with a cleavable polyhistidine tag. The plasmid was then transformed into *E. coli* JM109(DE3) and spread over the surface of LB agar medium with 100 ug/ml ampicillin using a sterile glass spreader. After overnight incubation at 37°C, single colonies were picked and inoculated into 200 ml of LB liquid medium containing carbenicillin (100 μg/ml), and cultured with vigorous shaking in an incubator at 37°C for 69 h. Bacterial cells were harvested by centrifugation at 8,000 rpm for 5 min. The harvested bacterial cell pellet was suspended in 10 ml of 20 mM 4-(2-hydroxyethyl)-1-piperazineethanesulfonic acid (HEPES, pH7.4) buffer and lysate by French Press G-M (Glen Mills Inc.). The suspension was centrifuged at 8,000 rpm for 20 min and the cell lysates were clarified. The supernatant containing the expressed recombinant protein was purified using Ni-NTA agarose affinity columns (QIAGEN). The purified protein was eluted with 2 ml of 200 mM imidazole buffer. A PD-10 desalting column (Cytiva) was used for buffer exchange of purified protein from 200 mM imidazole to 20 mM HEPES at a pH of 7.4. Size-exclusion chromatography (SEC), using ÄKTA (GE Healthcare) equipped with a Superdex200 10/30 (GE Healthcare) column, was used for further purification and buffer exchange of purified protein from 200 mM imidazole/TN buffer to 20 mM HEPES and 150 mM NaCl. Filtration using a 0.2 μm pore filter was conducted in advance to remove the impurities before loading the proteins onto the column. Approximately 500 μl of ~300 μM protein was injected into the column and eluted with 10 mM HEPES and 150 mM NaCl, at a pH of 7.4. The same procedure was followed to identify the

oligomerization status. Then, 500 µl of ~10 µM diluted protein was injected into the column and eluted with 10 mM HEPES and 150 mM NaCl, pH7.4.

Protein concentration, molar extinction coefficient (ε), quantum yield (Φ) determination and spectrum measurement. The GFP-like protein concentration was determined by the alkaline denaturation method, in which the absorption spectrum was recorded using a Bio UV-Vis spectrophotometer (V-630 BIO, Jasco). Then, ε was calculated from the determined protein concentrations. For the GFP-like protein concentration measurement, 500 µl of 10 µM purified protein was prepared in a polystyrene cuvette (SANYO) and mixed with 500 µl of 2 M NaOH using quick pipetting. The absorption spectrum was measured at 430-460 nm and the maximum absorption (~447 nm) of the denatured GFP chromophore corresponds to an ε of 44,000 M^{-1} cm^{-1}, which is equivalent to that of avGFP. According to Beer-Lambert's law, ε can be determined as: ($A_{peak\text{-}FP}/A_{447nm\text{-}denenatured}$) × 44,000 M^{-1} cm^{-1}. The determination of absolute fluorescence Φ, excitation, and emission spectra required a low-absorption protein sample (< 0.05). Accordingly, Φ was determined by integrating the sphere measurements (Absolute PL quantum yield spectrometer, C11347, Hamamatsu). The excitation and emission spectra of M-Velour-F were measured using a fluorescence spectrometer (F-7000, Hitachi High-Technologies).

Crystallization and structure determination. After protein purification of R-Velour, sodium dodecyl sulfate–polyacrylamide gel electrophoresis (SDS-PAGE) was performed to determine the degree of purification. To load protein onto the gel for SDS-PAGE analysis, 10 µl of 0.5 mg/ml target protein was mixed with 10 µl of 2 × sample buffer (0.5 M Tris-HCl pH6.8, 4% SDS, 10% β-mercaptoethanol, 10% glycerol, 0.2% bromophenol blue), followed by heating the samples at 95°C for 5 min and cooling on ice for 1 min. I then loaded a 10 µl denatured protein sample onto an SDS-PAGE gel and started electrophoresis that was performed for 90 min at 370 V and 35 mA current. Next, the gel was immersed and stained with Coomassie Brilliant Blue (CBB) staining buffer (0.1% CBB, 50% CH_3OH, 7% CH_3COOH). After shaking for 1 h, the stained SDS-PAGE gel was destained by incubating overnight with a destaining buffer (10% CH_3OH and 10% glacial acetic acid). Then, destained gel images were taken using an

LAS-1000 (FUJIFILM). To prepare the protein concentration gradient for the crystallization experiment, the purified protein was collected and concentrated using a centrifugation column (Millipore). The concentrated protein aqueous solution was then separately diluted to 10 mg/ml, 15 mg/ml, and 20 mg/ml and prepared for further use. The crystallization condition for the purified protein sample was initially selected using broad range screening according to a sitting-drop vapor diffusion method and optimized by a hanging-drop vapor diffusion method. Optimal R-Velour crystals were obtained in buffer containing 14% PEG 3350, 200 mM tri-sodium citrate pH5.4, 600 mM NaCl, and 20 mM HEPES at a temperature of 20°C. The crystallization drops contained 15 μM R-Velour. The crystals were immersed in 20% (v/v) glycerol as a harvesting buffer for cryoprotection and frozen in liquid nitrogen. Diffraction data were collected by applying the BL44XU beamline at SPring-8, with an Eiger X 16M (Dectris) detector at 100 K. The diffraction data were processed and scaled using the XDS program package[55]. Initial phasing of the crystals was performed by molecular replacement using KillerRed (PDB ID:3GB3) as the search model. The structures were refined and remodelled using the programs REFMAC[56] (CCP4)[57] and *Coot*[58]. Figures were prepared using PyMOL software (https://www.pymol.org/). The dihedral angle of "tilt" (τ) and "twist" (φ) angles were calculated through measurement in PyMOL software. Hydron bond interactions are characterized by interatomic distances between 2.5 and 3.3 Å. van der Waals (vdW) interactions are characterized by distances between atoms less than 3.9 Å. The chemical structure of the R-Velour chromophore was determined using the ChemiDraw online server (https://chemdrawdirect.perkinelmer.cloud/js/sample/index.html#). The B-factors were standardized using the following equation:

$$B_{norm} = (B - \langle B \rangle)/\sigma$$

; where B is the original B-factor value, ⟨B⟩ is the average of the B-factor (raw value) considered in a given structure, and σ represents the standard deviation [59].

pH Sensitivity Measurement and p*K*a Determination. Because the pH buffer solution resists pH changes when a small amount of acid, alkali, or other sample solutions are added, different pH buffer solutions were prepared to evaluate the pH sensitivity and to determine the apparent p*K*a of CPs and M-Velour-F. The following

solutions were selected as pH buffers: a 30 mM trisodium citrate and 30 mM borate solution, ranging from 2 to 4; a 30 mM trisodium citrate and 30 mM sodium tetraborate solution, ranging from 5 to 8; a 30 mM CHES and 30mM CAPS solution, ranging from 9 to 11; and a 10 mM trisodium phosphate solution, ranging from 12 to 13. The absorption spectrum was recorded using a Bio UV-Vis spectrophotometer (V-630 BIO, Jasco). The fluorescence spectrometer (F-7000, Hitachi High-Technologies) was applied for recording the fluorescence spectrum of M-Velour-F. The intensities of measured absorption and fluorescence were plotted against pH. Using Origin8 software (OriginLab), the p*K*a was calculated by fitting the data to the following generalized Henderson-Hasselbalch equation:

$$\mathrm{A} = \frac{\mathrm{A_1}}{1 + 10^{\mathrm{n_{H1}(pK_a - pH)}}}$$

(A_1 is the absorption intensity of the anionic chromophore at the maximum plateau. n_{H1} is the apparent Hill coefficient.)

Site directed- and saturation mutagenesis, and screening of libraries. Site-directed mutagenesis and saturation mutagenesis based inverse polymerase chain reaction (PCR) were performed to generate the R-Velour fluorescence mutant (M-Velour-F). Primers used in inverse PCR were oriented in the opposite direction compared to conventional PCR. Degenerate primers with randomized codons used in saturation research were purchased from Hokkaido System Science. The degenerate codon of NNK can randomly encode all 20 amino acids which was used for the design of the primers for saturation mutagenesis. The primers were supplied as non-phosphorylated. Amplified DNA fragments without the 5' phosphate terminal cannot be used for DNA ligation. Therefore, the primers need to be phosphorylation in advance before inverse PCR. Primers for inverse PCR were mixed with the following reagents: 2 µl of 10×T4 PNK buffer (alkaline phosphatase), 2 µl of 100 µM ATP, 2 µl of 10 U/µl T4 PNK and 13.5 µl of dH_2O, to phosphorylate the primers and incubated at 37°C for 1 h. DNA amplification was performed by inverse PCR: 1.5 µl of DNA template (< 50 ng) was mixed with 25 µl of 2x PCR buffer for KOD FX Neo (Toyobo Life Sciences), 10 µl of 2 mM dNTPs, 1.5 µl of 10 µM forward and reverse primer respectively, 1 µl of 1 U/µL KOD FX Neo, and 9.5 µl of dH_2O. The DNA library was amplified as follows: 94°C for 2 min, 98°C for 10 s, (Tm of primer)°C for 30 s, 68°C for 2.5 minutes, 68°C

for 5 min, and steps 2–4 were repeated for 30 cycles. To avoid transformation of the template DNA into *E. coli* JM109(DE3), the restriction enzyme, *Dpn*I, was used to digest the methylated template DNA under incubation at 37°C for 2h. The synthesized linear DNA plasmid was purified by phenol-chloroform extraction and ethanol precipitation. TE (20 µl of TE was used to dissolve the purified plasmid pellets. For ligation, 2 µl of single strand purified plasmid was mixed with 0.5 µl of T4 ligase (Promega), 2 µl of 2× Rapid Ligation Buffer (Promega), and 1.5 µl of H_2O, at room temperature. After incubation for 15 min, 8 µl of the ligation solution was transformed into *E. coli* JM109(DE3). The transformed bacteria were disseminated on LB agar plates containing 0.1 mg/ml carbenicillin and incubated overnight at 37°C. Approximately 15,000 colonies were prepared and screened with the naked eye under ambient light in each round of mutagenesis to check the CP color variants. M-Velour-F was checked based on fluorescence emission under blue light illumination from LightEngine SPECTRA (Lumencor), in which the illumination system was equipped with a 475/28 nm excitation filter (Semrock) and a 535 AF26 nm emission filter (OMEGA OPTICAL). ImageJ was utilized in order to perform the analysis on the imaging data (http://imagej.net/Fiji/Downloads). Screened colonies with novel color or fluorescence were cultured in 2 ml LB media with 100 µg/ml carbenicillin, followed by mini-scale preparations and sequencing determination.

Data Availability Statement. The nucleotide sequence data of ofCP and R-Velour was deposited on DNA Data Bank of Japan (DDBJ) with accession number of **LC663961** and **LC663962** respectively. The crystallographic data for R-Velour is deposited on worldwide Protein Data Bank (wwPDB) with the deposition numbers 7cao.

2.3 Results and discussion

2.3.1 R-Velour structure

The complete R-Velour gene is composed of 690 base pairs and encodes 229 amino acid residues. R-Velour shares 51% amino acid sequence homology with Gamillus, suggesting chromophore formation with the 60th to 62nd residues (**Figure. 3**). Purified R-Velour protein with an N-terminal 6xHis-tag was crystalized and the 3D structure was determined using X-ray crystallography. The crystal belonged to $I4_122$ space group, and the structure was refined to a final R_{factor}/R_{free} of 19.43/21.99%, at a resolution of 2.1 Å (PDB: 7cao; **Table 4**). R-Velour has the typical β-can fold of FP and is composed of an 11-stranded β-barrel, with each β sheet linked by a loop region and the circularized chromophore consisting of a tripeptide (Gln60-Try61-Gly62) located in the middle part of the α2-helix motif penetrating the central axis of the β-barrel (**Fig. 4A**). Apparently, the two-ring chromophore of the R-Velour 4-(p-hydroxybenzylidene)-5-imidazolinone group consisted of a central imidazolinone moiety with *a p*-hydroxybenzylidene substituent and adopts a *trans*-conformation between the Cα2-Cβ2 bond, as with Gamillus (**Figure. 4B**). Similar to other GFP-like proteins [60–63], the five-membered ring heterocyclic imidazolinone is presumed to be generated by a nucleophilic attack at the carbonyl group of Gln60, from the amide nitrogen of Gly62. Subsequently, the π-electron conjugated system is extended by further oxidation of the Cα2-Cβ2 bond in the Try61 moiety.

Figure 3. Alignment of the amino acid sequences of GFP-like proteins of R-Velour and Gamillus from *Olindias formosa*. Identical residues between R-Velour with Gamillus are boxed in gray. The residues in the tri-peptide chromophore are indicated by the green frame. The secondary structure elements based on R-Velour are included above the alignment.

Table 4 Data collection and refinement statistics

	R-Velour
PDB code	7cao
Data collection	
Light source	SPring-8 BL44XU
Wavelength (Å)	0.9000
Space group	$I4_122$
Cell dimensions	
a, b, c (Å)	116.48, 116.48, 161.44
α, β, γ (°)	90, 90, 90
Resolution (Å)	49.57-2.05(2.16-2.05)
R_{merge}	0.039(0.540)
R_{meas}	0.041(0.571)
$R_{p.i.m.}$	0.016/0.197
$I/\sigma I$	31.29(3.65)
$CC_{1/2}$	1.000(0.917)
Completeness (%)	98.3(95.2)
Multiplicity	9.1(9.2)
Refinement	
Resolution (Å)	49.57-2.05
Number of reflections	
Observed	315105/(48925)
Unique	34497/(5324)
R_{work}/R_{free}	0.1922/0.2109
Number of atoms	
Protein	1768
Ligand/ion	0
Water	60
B-factors (Å^2)	
Protein	48.7
Ligand/ion	-
Water	44.3
R.m.s. deviations	
Bond lengths (Å)	0.0164
Bond angles (°)	2.0963
Ramachandran plot (%)	
Most favored	98.2
Allowed	1.8
Outliers	0

(A)

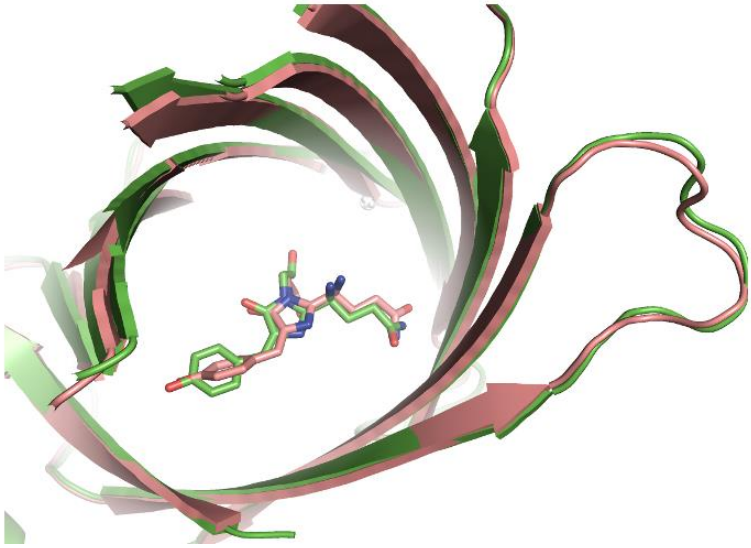

(B)

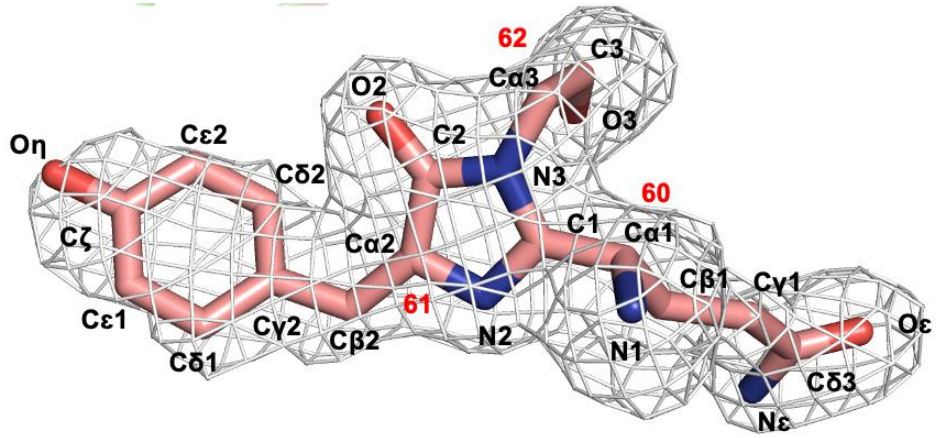

Figure 4. Molecular structure of R-Velour determined by X-Ray crystallography.

(A) Superimposed structure of R-Velour (salmon; PDB:7cao) and Gamillus (green; PDB:5y00). **(B)** The omit map (*F*o-*F*c), contoured at 3.0σ, is depicted as a gray mesh; the R-Velour chromophore is represented as a stick model (Salmon, carbon; Red, oxygen; Blue, nitrogen). Bold red numbers indicate the locations of Cα atoms in the amino acids Gln-60, Try-61, and Gly-62 of R-Velour.

2.3.2 Chromophore environment of R-Velour

I investigated the chromophore environment of R-Velour, which involved hydrogen bond network and van der Waals contacts (Figure. 5-7, and Table 5). The phenolate oxygen of the chromophore directly formed hydrogen bonds with a water molecule and Ser155 in the β8-strand. Hydrogen bonds similar to that of the chromophore phenolate oxygen exist in Gamillus as bonds with a water molecule and Ser166 (**Figure. 5A, B**). These hydrogen bonds suggest stabilization of the *trans* chromophore. In addition, the bulky Phe140 side chain of R-Velour prevents chromophore placement in the *cis*-conformation, additionally stabilizing the *trans*-conformation (**Figure. 8**). Meanwhile, extended hydrogen bond networks via the water molecule toward Met153 in the β8-strand, and Ser173 in the β9-strand, further stabilized the chromophore phenolic ring (**Figure. 5A**). Because the water molecule is separated from bulk water and protects the protonation of chromophore phenolate oxygen by hydrogen bond formation in Gamillus (**Figure. 5B**), it is considered to tolerate low pH (p*Ka* = 3.4). A similar, but weakened effect was also present in R-Velour (p*K*a = 4.8). Moreover, both R-Velour and Gamillus have an identical arrangement of the highly conserved Arg89 and 99, and Glu212 and 223 residues, which form hydrogen bonds with O2 and N2 in the imidazolidone moiety (**Figure. 5C, D and Figure. 6, 7**).

The remarkable structural feature of the R-Velour chromophore is the small number of hydrogen bonds relative to that of Gamillus. The hydrogen bond network between the chromophore and the 12 adjacent amino acids (Phe47, Ser67, Pro68, Arg99, His113, Tyr115, Ser124, Leu164, Ser166, Cys184, Gln221, and Glu223) that contribute to chromophore stabilization are formed in Gamillus. In contrast, only 9 amino acids (His10, Ser56, Ser 64, Arg89, Met153, Ser155, Ser173, Tyr175, and Glu212) were involved in R-Velour (**Table 5**). The major difference is the lack of hydrogen bonds from the Nε atom of the Gln60 moiety in R-Velour, where hydrogen bonds network among the corresponding atom of the Gln70 moiety, Phe47 and water molecules are formed in Gamillus. Furthermore, the O3 atom of the Gly62 moiety in R-Velour, whose corresponding atom of the Gly70 moiety in Gamillus forms hydrogen bonds with Pro68, His113, Tyr115, Ser124, and a water molecule, links with only one

residue, Glu212, through a water molecule (**Figure. 5E, F**). Conversely, various residues (Phe37, Arg38, Met39, Pro57, Ser58, Tyr105, Phe140, Cys142, Val171, and Met210) clustered around the chromophore in R-Velour only formed van der Waals contacts with the chromophore without forming hydrogen bonds, in contrast to a small number of residues (Asn48, Met49, His74, Leu97, Val152, Gln182, Thr222) in Gamillus (**Figure 8**).

(A)

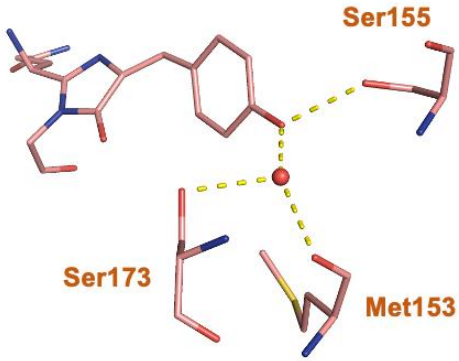
Ser155
Ser173
Met153

(B)

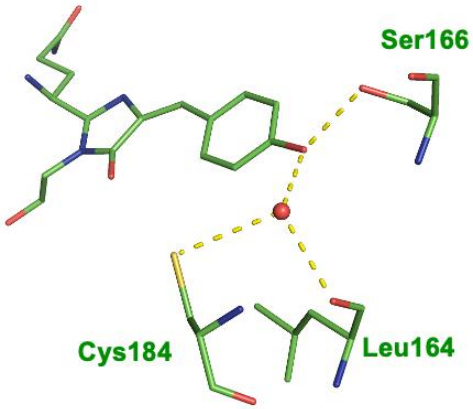
Ser166
Cys184
Leu164

(C)

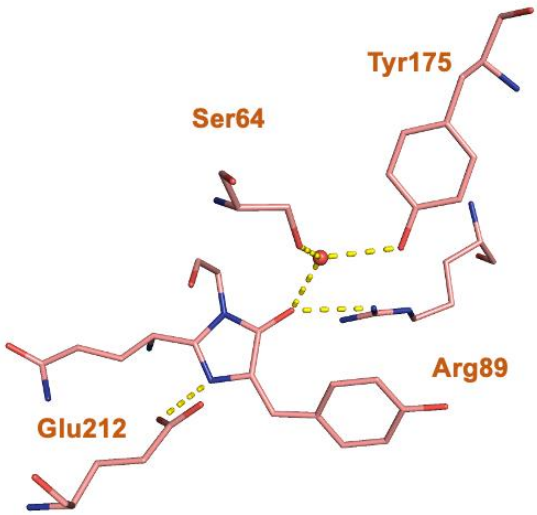
Tyr175
Ser64
Arg89
Glu212

(D)

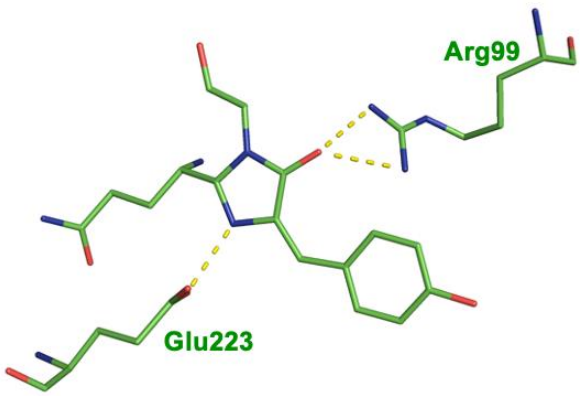
Arg99
Glu223

(E)

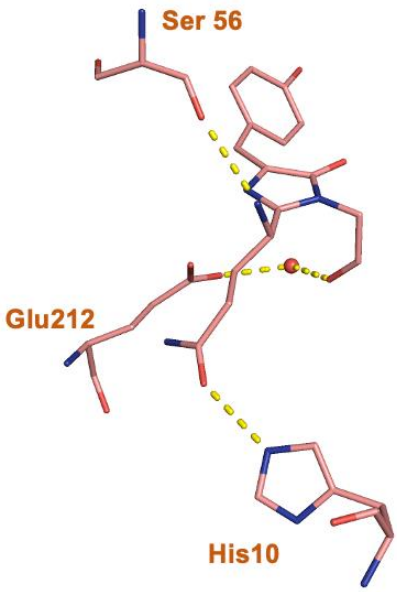
Ser 56
Glu212
His10

(F)

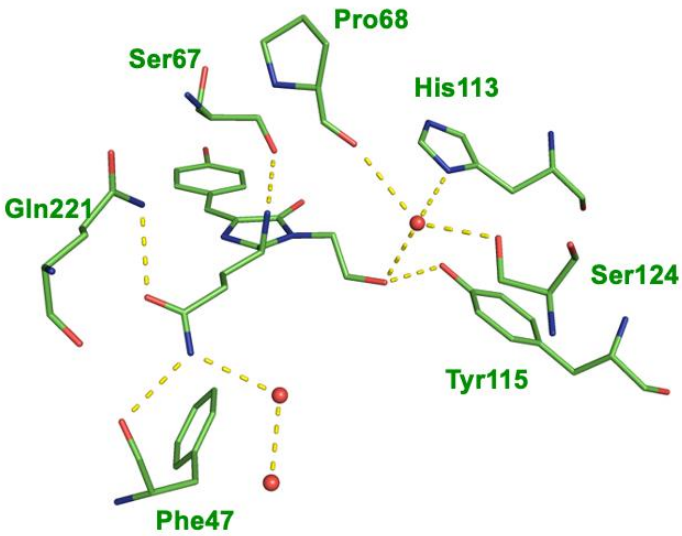
Pro68
Ser67
His113
Gln221
Ser124
Tyr115
Phe47

Figure 5. Hydrogen bond network of R-Velour (PDB:7cao) and Gamillus (PDB:5y00) in their nearest chromophore environment. (A, B) Hydrogen bond network in phenoxy moiety. **(C, D)** Hydrogen bond network in imidazolinone moiety. (**E, F**) Hydrogen bond network in glutamine and glycyl moiety. The chromophore environment is depicted in a stick representation for R-Velour (salmon) and Gamillus (green)**.** Hydrogen bond interactions are shown as yellow dashed lines and water molecules as red spheres. Insufficient hydrogen bond environment is indicated in the R-Velour chromophore.

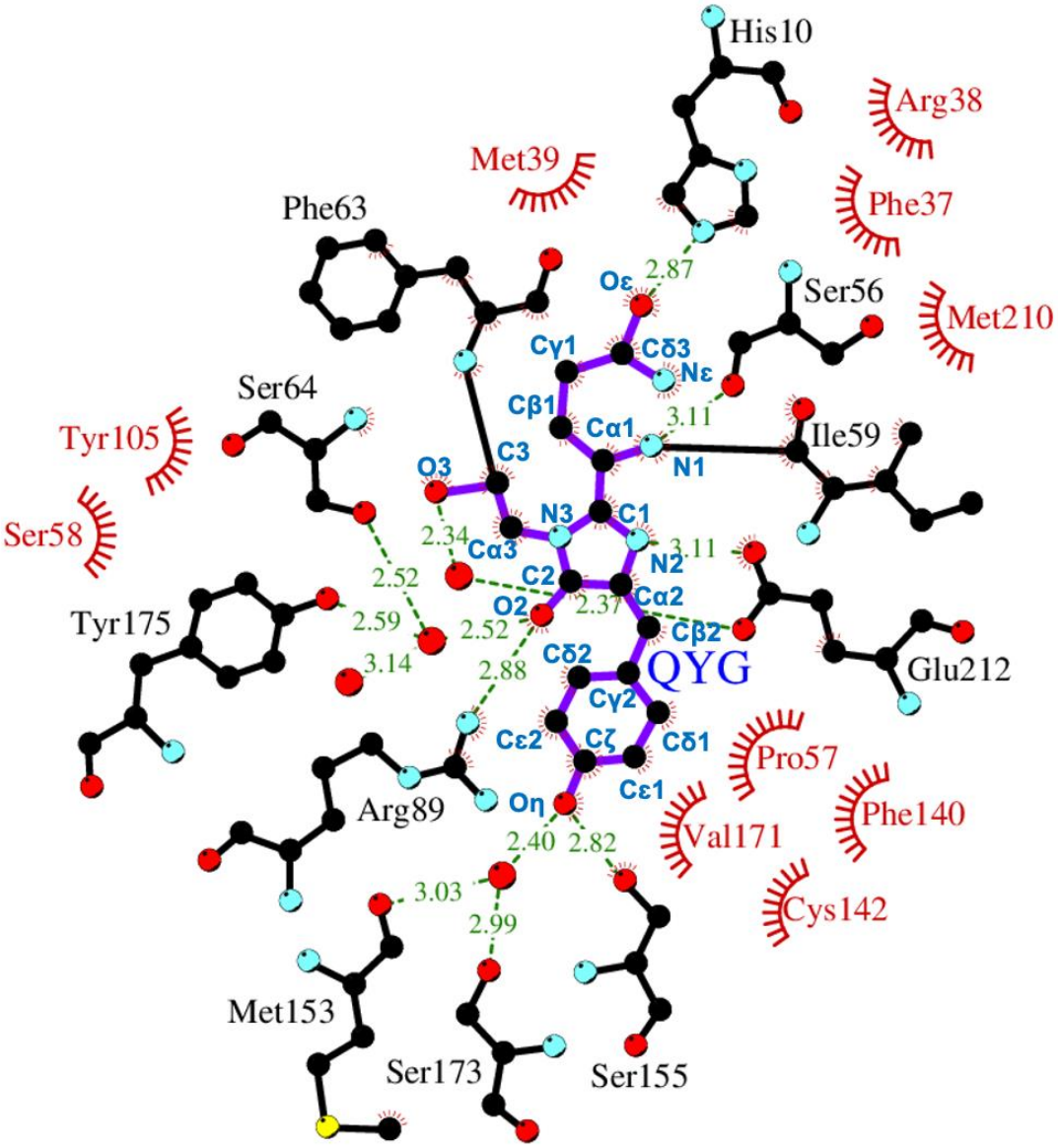

Figure 6. The schematic 2-D representations from LIGPLOT showing the nearest residues environment of the R-Velour chromophore. Hydrogen bonds (≤3.3 Å) are shown as green dashed lines, water molecules as red spheres, and van der Waals contacts (≤3.9 Å) as red “eyelashes”. The chromophore bonds are depicted in purple, meanwhile the surrounding residue bonds are depicted in black. The backbones of I59 and F63 that formed covalent bonds with the chromophore are shown in black. The chromophore and its surrounding 9 amino acids form a hydrogen-bond network (His10, Ser56, Ser 64, Arg89, Met153, Ser155, Ser173, Tyr175, and Glu212) are involved in R-Velour.

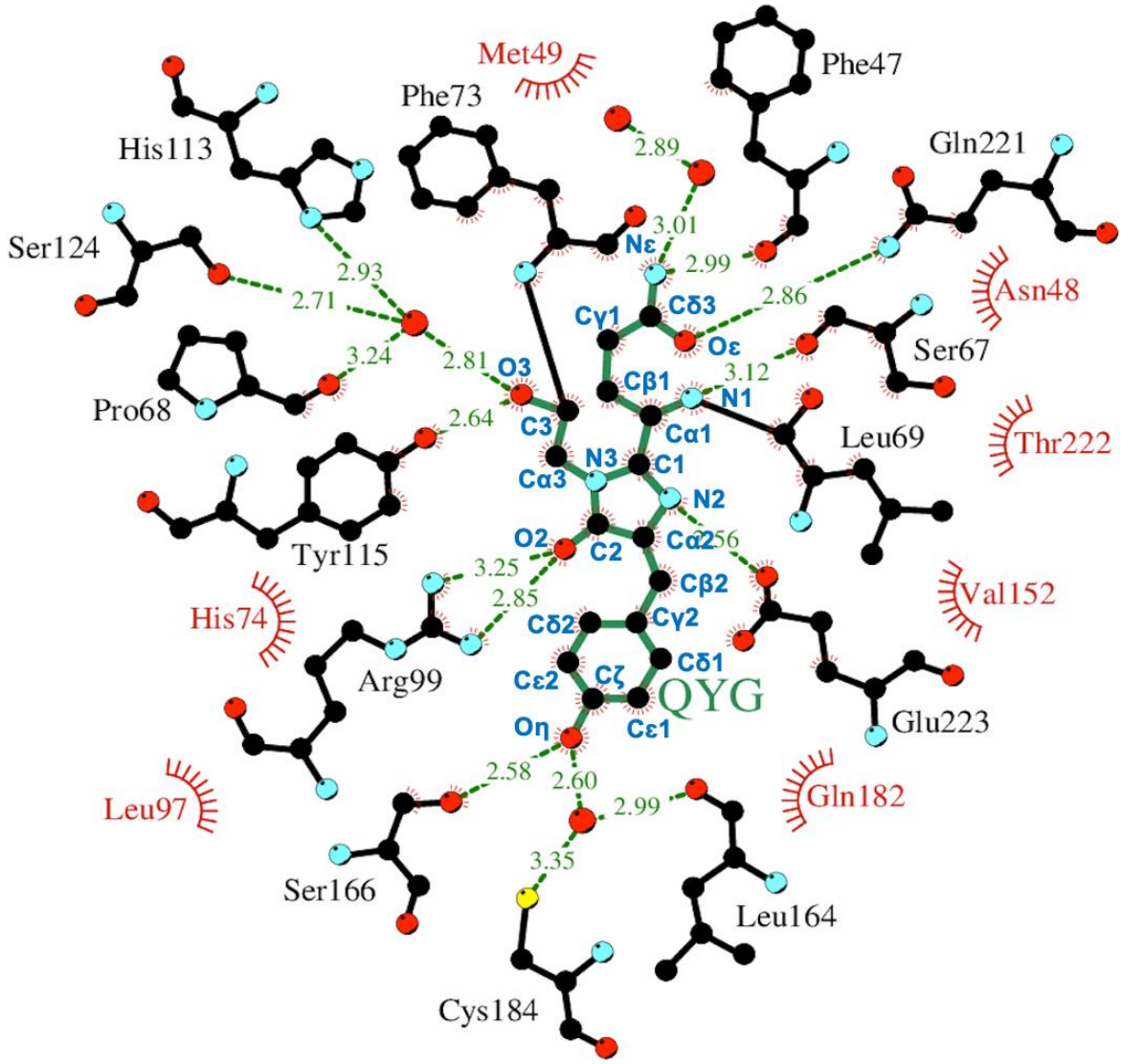

Figure 7. The schematic 2-D representations from LIGPLOT showing the nearest residues environment of the Gamillus chromophore. Hydrogen bonds (≤3.3 Å) are shown as green dashed lines, water molecules as red spheres, and van der Waals contacts (≤3.9 Å) as red “eyelashes”. The chromophore bonds are depicted in purple, meanwhile the surrounding residue bonds are depicted in black. The chromophore and its surrounding 12 amino acids formed a hydrogen-bond network (Phe47, Ser67, Pro68, Arg99, His113, Tyr115, Ser124, Leu164, Ser166, Cys184, Gln221, and Glu223) that contribute to chromophore stabilization are formed in Gamillus.

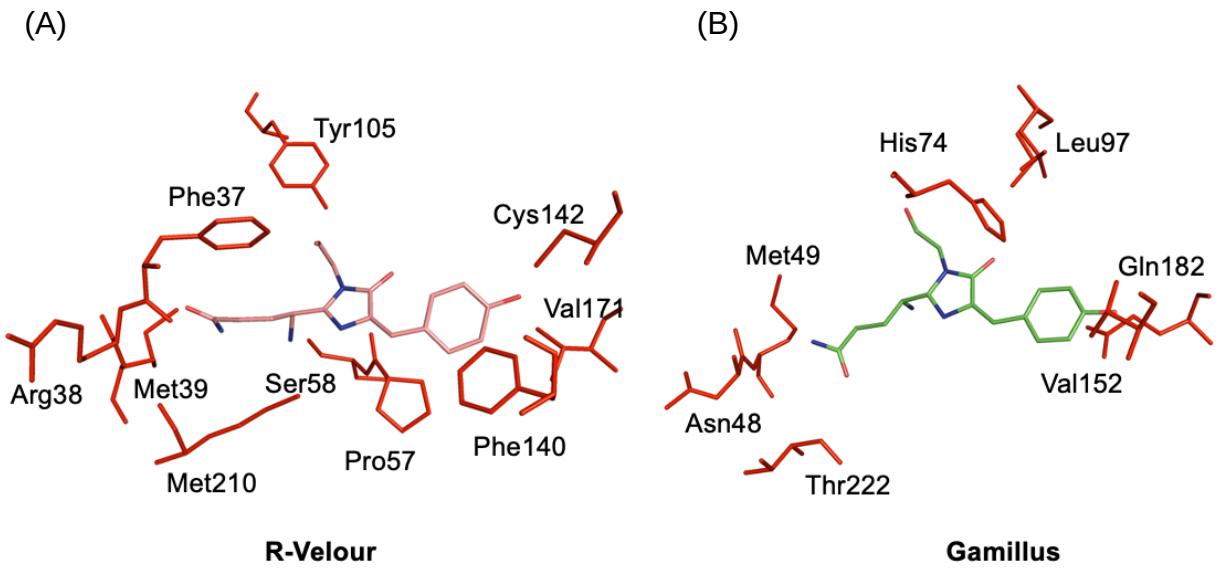

Figure 8. Van der Waals interactions in the chromophore of R-Velour (PDB:7cao) and Gamillus (PDB:5y00). (A, B) The residues gathered around the chromophores of R-Velour and Gamillus are marked in red. These residues only form van der Waals contacts with the chromophore and not hydrogen bonds. The chromophore is depicted in a stick representation for R-Velour (salmon) and Gamillus (green). Insufficient hydrogen bond environments are indicated in R-Velour chromophore compared with Gamillus. Various residues (Phe37, Arg38, Met39, Pro57, Ser58, Tyr105, Phe140, Cys142, Val171, and Met210) clustered around the chromophore in R-Velour only formed van der Waals contacts with the chromophore without forming hydrogen bonds, in contrast to a small number of residues (Asn48, Met49, His74, Leu97, Val152, Gln182, Thr222) in Gamillus.

Table 5. Chromophore contact in R-Velour and Gamillus

Chromophore (QYG)	Residues of R-Velour	Residues of Gamillus	Type of interaction
Phenoxy Moiety			
Cβ2	Pro57	Ser67, Glu223	van der Waals
Cγ2	-	Ser67	van der Waals
Cδ1	Pro57, Phe140	-	van der Waals
Cε1	Phe140, Ser155	Val152, Ser166, Gln182	van der Waals
Cδ2	Arg89	Arg99, His74	van der Waals
Cε2	Arg89, Met153	Arg99, Gln182	van der Waals
Cζ	Arg89, Phe140, Cys142, Ser155	Val152, Ser166, Gln182	van der Waals
Oη	Ser155	Ser166	Hydrogen bond
	Met153, Ser173	Leu164, Cys184	Water mediated hydrogen bond
	Cys142, V171	Val152, Gln182	van der Waals
Imidazolinone Moiety			
C1	Pro57, Glu212	Ser67, Phe73, Glu223	van der Waals
N2	Glu212	Glu223	Hydrogen bond
	Ser56, Pro57, Met210	Ser67	van der Waals
Cα2	Pro57	Ser67, Glu223	van der Waals
C2	Pro57	Ser67, Phe73, His74	van der Waals
N3	Pro57, Phe63	Pro57, Phe63	van der Waals
O2	Arg89	Arg99	Hydrogen bond
	Ser64, Tyr175	-	Water mediated hydrogen bond

	-	Ser67, His74, Leu97	van der Waals
Glutamine Moiety			
N1	Ser56	Ser67	Hydrogen bond
Cα1	Ile59	Ser67, Leu69, Phe73	van der Waals
Cβ1	Ile59, Met210, Glu212	Leu69, Gln221, Glu223	van der Waals
Cγ1	Ile59	Leu69, Gln221	van der Waals
Cδ3	Phe37, Met39	Phe47	van der Waals
Oε	His10	Gln221	Hydrogen bond
	Phe37, Arg38, Met39	Phe47, Glu223	van der Waals
Nε	-	Phe47	Hydrogen bond
	-	H_2O	Water mediated hydrogen bond
	Phe37, Glu212	Asn48, Met49, Gln221	van der Waals
Glycyl Moiety			
Cα3	Pro57, Phe63	Phe73	van der Waals
C3	Phe63, Ser64	Phe73	van der Waals
O3	-	Tyr115	Hydrogen bond
	Glu212	Pro68, His113, Ser124	Water mediated hydrogen bond
	Phe37, Phe63, Ser64	Phe73	van der Waals

Supported by these interactions with surrounding residues, the chromophore in R-Velour exhibited an apparent non-coplanar conformation with noticeable dihedral angle distortion, which is a typical CP feature. Torsion angles, “tilt” (τ) and “twist” (φ), calculated to evaluate the relative orientation of the two rings in the chromophore indicates that the trend of the off-coplanar chromophore of R-Velour is mainly due to the large φ (41.4°) angle, rather than the small τ (-9.1°) angle (**Fig. 9A**). The φ of R-Velour is much larger than that of Gamillus (9.5°), and the chromophore phenolic ring of the R-Velour is extruded from the plane of the imidazolinone moiety. This is due to steric hindrance from the bulky side chain of Phe140 in the β7-strand, and Arg89 in the β4-strand (**Fig. 9B**). As for Gamillus, the corresponding residues, Asn150 and Arg99, do not disturb the coplanarity of the chromophore (**Fig. 9B**). Additionally, the chromophore in R-Velour is sandwiched between Phe140, Val171, and Pro57, where Asn150, Gln182, and Ser57 are the corresponding residues in Gamillus (**Fig. 9B**). The relatively long distance between Val171 in the β9-strand and Pro57 in the α2-helix of R-Velour provides sufficient space to accommodate the distorted hydroxybenzylidene group. In Gamillus, Gln182 and Ser67 are in proximity through hydrogen bond interactions, which restricts chromophore torsion to maintain coplanarity. I also considered the chromophore flexibility by comparing the B-factors in the crystal structure (**Figure 10**). Most of the atoms in the phenoxy (Tyr61) moiety of the R-Velour’s chromophore showed a higher B-factor than other atoms. B-factors of Glycyl (Gly62) and Glutamine (Gln60) moieties follows that. The imidazolinone moiety with the smallest values exhibited a lower B-factor than the mean value of all atoms. For Gamillus, B-factors in all chromophore atoms were lower than the mean value of all atoms. These results suggest the higher motility of the phenoxy moiety of the R-Velour chromophore and the higher stability of the Gamillus chromophore. Taken together, the non-fluorescence property of R-Velour with almost zero quantum yield might be attributed to the combination of the large torsion of the two chromophoric rings and higher motility of the phenoxy (Tyr61) moiety.

(A) (B)

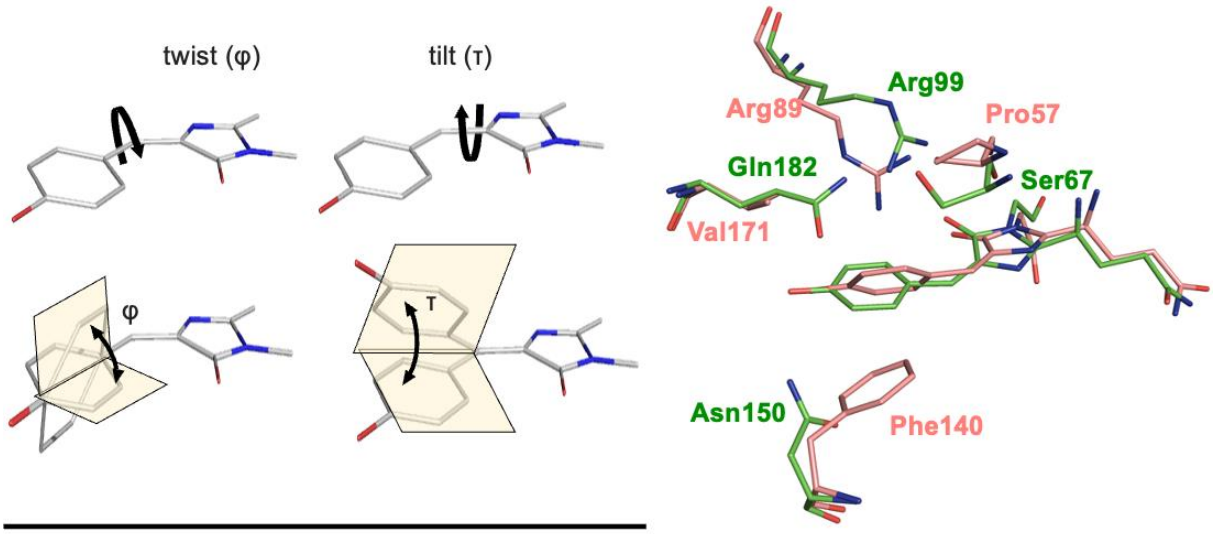

GFP-like protein	Angle (φ)	Angle (τ)
R-Velour	41.4	-9.1
Gamillus	9.5	-5.4

Figure 9. Structure analysis of R-Velour, compared with Gamillus, based on their crystal structure. (A) Schematic illustration of "tilt" (τ) and "twist" (φ) angles are shown in the upper part. Angle values of τ and φ in R-Velour and Gamillus are shown in the table blow. **(B)** Chromophore and closed residues of R-Velour (PDB:7cao) and Gamillus (PDB:5y00) are superimposed and colored in salmon and green, respectively.

(A)

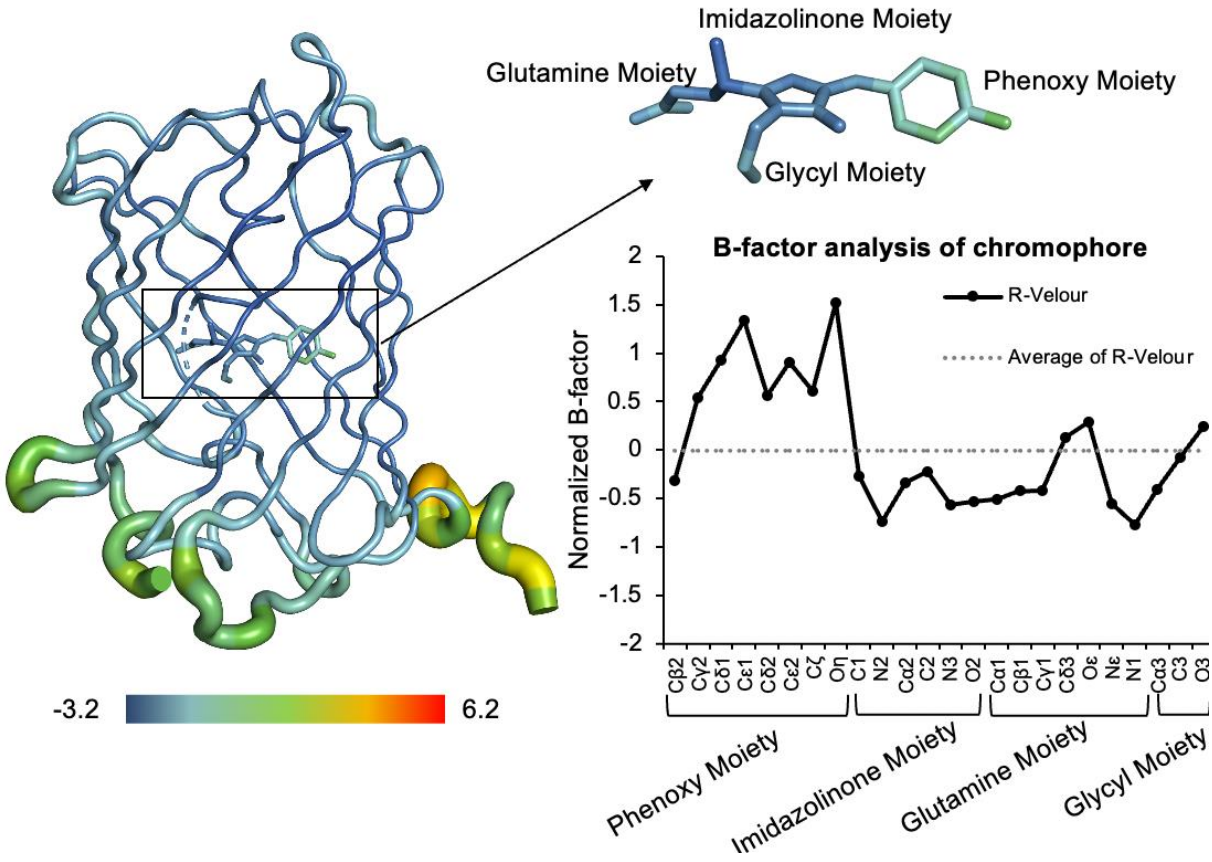
Imidazolinone Moiety
Glutamine Moiety
Phenoxy Moiety
Glycyl Moiety
B-factor analysis of chromophore
R-Velour
Average of R-Velour
Normalized B-factor
2
1.5
1
0.5
0
-0.5
-1
-1.5
-2
Cβ2 Cγ2 Cδ1 Cε1 Cδ2 Cε2 Cζ Oη C1 N2 Cα2 C2 N3 O2 Cα1 Cβ1 Cγ1 Cδ3 Oε Nε N1 Cα3 C3 O3
Phenoxy Moiety
Imidazolinone Moiety
Glutamine Moiety
Glycyl Moiety
-3.2
6.2

(B)

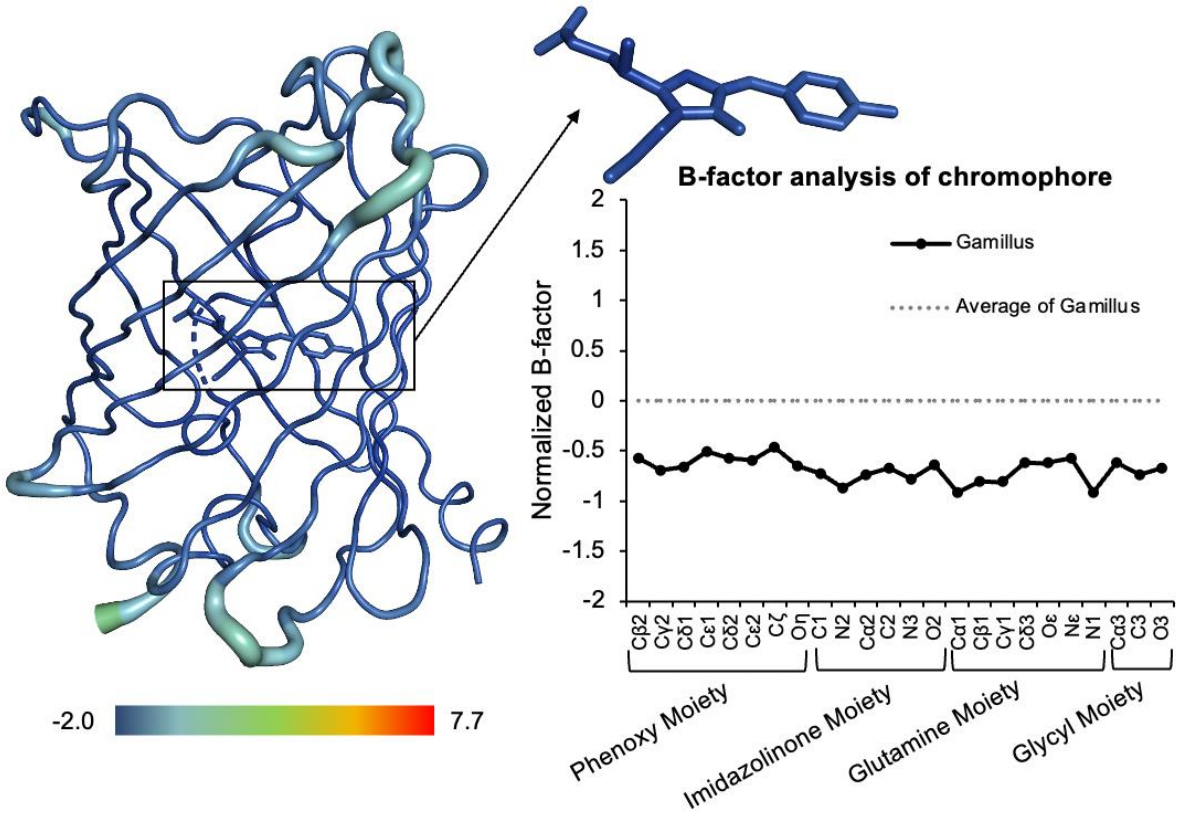
B-factor analysis of chromophore
Gamillus
Average of Gamillus
Normalized B-factor
2
1.5
1
0.5
0
-0.5
-1
-1.5
-2
Cβ2 Cγ2 Cδ1 Cε1 Cδ2 Cε2 Cζ Oη C1 N2 Cα2 C2 N3 O2 Cα1 Cβ1 Cγ1 Cδ3 Oε Nε N1 Cα3 C3 O3
Phenoxy Moiety
Imidazolinone Moiety
Glutamine Moiety
Glycyl Moiety
-2.0
7.7

Figure 10. B-factor analysis of the chromophores between R-Velour and Gamillus. (A) B-factors of backbone and chromophore atoms standardized across R-Velour, ranging from −3.2 (blue) to 6.2 (red). Its protein values are indicated by the thickness of the lines representing the protein backbone. The overall B-factors for the R-Velour chromophore were highest in the phenoxy moiety, followed by the glycyl- and glutamine moieties. Atoms in the imidazolinone moiety had the smallest B-factor values, lower than the mean value of all atoms in R-Velour. **(B)** Backbone and chromophore atoms of Gamillus are colored by normalized B-factor ranging from -2.0 (blue) to 7.7 (red). All atoms exhibited similar values of B-factor below average for all atoms of Gamillus.

2.3.3 Site-directed saturation mutagenesis for Phe140

We found that, based on the structural analysis of R-Velour, the angular distortion of the chromophore ring caused by Arg89 and Phe140 is responsible for the undetectable quantum yield in R-Velour. Arg89 is a key conserved residue that mediates the maturation process and corresponds to Arg96 in wild-type GFP [64]. Mutagenesis was therefore focused on Phe140 instead of Arg89. Phe140, which has a bulky side chain in the β7-strand, restricted the orientation of the phenolic ring of Tyr61, inducing the non-coplanar chromophore of R-Velour. To confirm this hypothesis, we investigated the influence of the mutation introduced into Phe140. Initially, expecting enhanced fluorescence from the chromophore with a reduced “twist” (φ) angle, we chose small sized amino acids and constructed F140A, F140L, and F140N mutants. However, mutant colonies lost the original red color under ambient light. The colorless Phe140 mutants hampered chromophore maturation. Chromophore cyclization might be prevented by the increased motility of chromophore formation residues in the space enlarged by smaller side chains.

Next, we attempted to introduce a bulkier aromatic mutation of F140W and simultaneous site-specific saturation mutagenesis to the 141st and 142nd residues. Inward Cys142 has a side chain directed to the chromophore phenolic ring, which is the closest residue to Phe140 (**Figure 11A**). We expected that the substitution of Cys142 with other smaller residues would leave enough free space for Typ140. We

used ofCP2.2 as the template. After screening ~2,000 colonies, we found one colony with the F140W/C142G mutation in ofCP2.2 (M-Velour-F), which exhibited fluorescence with a quantum yield of 0.12 (**Figure. 11B**). M-Velour-F has excitation and emission spectra peaks at 502 nm and 518 nm (**Figure 11B**), which is almost identical to that of Gamillus (504 nm and 519 nm). M-Velour-F exhibited two absorption peaks at 392 nm and 532 nm (**Figure. 11C**). Additionally, pH titration result indicated that M-Velour-F has an extremely alkaline pH response (pKa=9.3).

M-Velour-F with two mutations in F140W/C142G exhibited two absorption features. We considered that the peak absorption at 392 nm might be due to a non-fluorescent neutral state chromophore, identical to that of wild-type GFP and Gamillus. The broad absorption spectrum with a maximum of 532 nm did not correspond with the fluorescence excitation spectrum, with a peak of 502 nm (**Figure 11B, C**). A similar inconsistency was found for HcRed, a fluorescent mutant derived from the CP hcCP with an absorption maximum of 573 nm and an excitation maximum of 598 nm. The two components of the chromophore in the crystal structure of HcRed exhibited *cis* coplanar and *trans*-non-coplanar conformations suggesting the coexistence of fluorescent coplanar and non-fluorescent non-coplanar states [15]. Fluorescent excitation peak wavelength of HcRed 598 nm derived from coplanar chromophore is longer than that of absorption peak 573 nm derived from non-coplanar chromophore. However, the relationship is opposite in the case of M-Velour-F. The detailed differences could be verified by structural analysis.

In addition, I am surprised to find that the M-Velour-F has the photochromic property, which is similar but exhibited slightly different with an orange non-fluorescent photochromic protein, Phanta [65,66]. In its initial ON state, the absorption spectrum of Phanta peaks at 505 nm. With cyan irradiation, the absorption of 505nm species dropped, while the absorption peak at 390 nm increased. Phanta's subsequent exposure to UV light resulted in a decrease in the peak at 390 nm and an increase in the peak at 505 nm. The absorption spectrum of M-Velour-F also can be reversibly altered under the light irradiation (**Figure 12A**). In M-Velour-F equilibrium state (Turn-off state), it showed weak green fluorescent protein property. The principal peak is 532 nm and the secondary peak is 502 nm. After UV light irradiation, the absorption peak

at 532 nm increased, while the absorption peak at 400 nm decreased (**Figure 12B**). And M-Velour-F at this state (Turn-on state) showed chromoprotein property. In addition, the turn-on state can be restored to the original turn-off state under teal light irradiation.

(A)

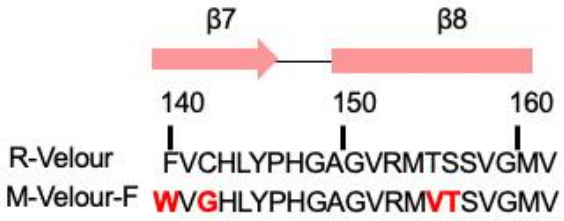

(B) (C)

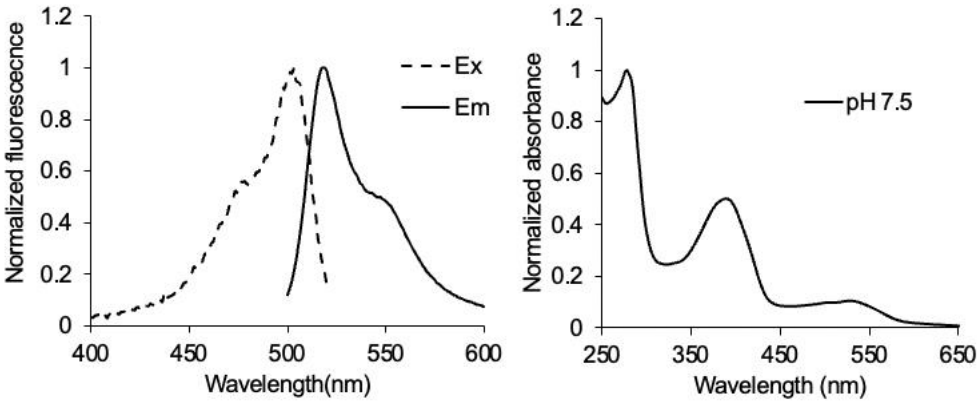

Figure 11. Evolution of M-Velour-F from R-Velour. **(A)** Amino acid sequence alignments (140th-160th) among R-Velour and M-Velour-F. Mutations are highlighted in bold red. **(B)** Normalized excitation/emission spectra at pH7.5. **(C)** Normalized absorption spectrum of purified M-Velour-F, which was measured under pH7.5, at 10 μM at 25°C.

(A)

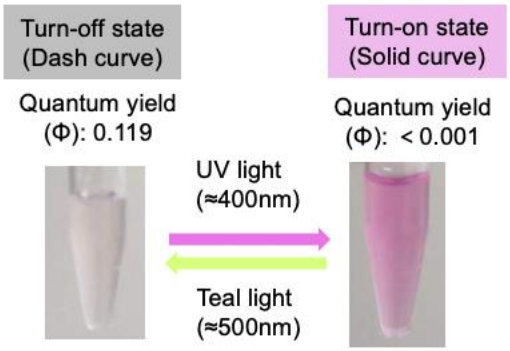

(B)

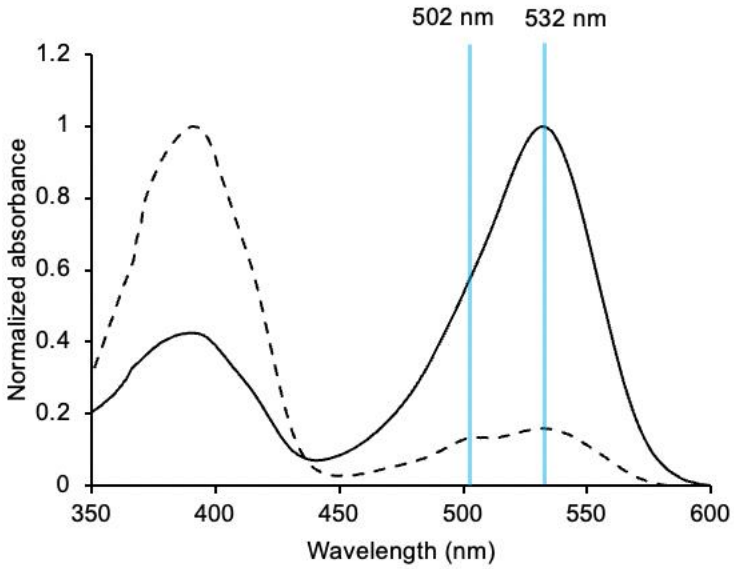

Figure 12. *In vitro* Characterization of M-Velour-F with photochromic property. **(A)** Illustration of photochromic protein switching under white light imaging. **(B)** Absorption spectrum of M-Velour-F with photochromic property.

2.4 Conclusion

I determined the crystal structure of one recently isolated, completely non-fluorescent red CP, R-Velour, to a 2.1 Å resolution. The R-Velour chromophore adopts a non-coplanar *trans*-chromophore. Structure-based mutagenesis of R-Velour revealed that the 140th and 142nd residues are vital to fluorescence properties. Additionally, M-Velour-F with green fluorescent emission property was developed. M-Velour-F with high pK_a also can be applied in the study of extreme alkaline and high pH physiological environments in Alkaliphiles [67–69] or other high pH ecological systems [70,71]. Furthermore, genetic report proteins with the far-red light absorption and photochromic behaviour has been reported to improve the resolution of PAI [72–74]. Taking advantage of photochromic property, the photoacoustic images can be subtracted between the two isomeric states, essentially erasing the dominant background signals while maintaining just the photoacoustic signals of the optical reporter gene. The development of the genetically encoded reporter of photochromic M-Velour-F with the visible light absorption will make it a possible to exploit and utilize multi-color high-resolution photoacoustic imaging at the cellular level in the near future.

CHAPTER 3

Expanding the CP diversity from R-Velour and mTFP1

3.1 Introduction

As stated earlier, directed evolution has been successful in producing CPs of multiple colors and further reducing quantum yield, such as ShadowG and ShadowY, both of which have light absorption between 480 nm and 520 nm in wavelength, and ShadowR, which has redder maximal absorption at 585 nm (Table 1). However, CPs with absorption maximum between 520 nm and 560 nm have not yet been discovered. R-Velour exhibits a maximum absorption spectrum at 528 nm, hence its mutation-induced spectral shift has the great potential to bridge the existing optical window gap. Investigation of the relationship between mutagenesis and spectrum shift will bring a helpful guideline for the diversification of CPs.

In addition, I also found that in the current optical window of existing CP libraries, a well-characterized CP with absorption wavelengths of 440 nm to 480 nm that can be used as a FRET acceptor for blue fluorescent protein (BFP) has not yet been identified [50]. Mutation-induced reductions in the quantum yields of CFPs with ideal absorption peak could lead to new color variations of CPs.

3.1.1 Exploring the mutations of R-Velour color variation

There is a report of mutations to red-shift wild-type *Aequorea Victoria* GFP on the residues proximal to the chromophore including Thr203. [75]. Wild-type GFP exhibits near-ultraviolet and visible absorption peaks around 397 nm and 477 nm, corresponding to the neutral and anionic forms of the chromophore, respectively. According to mutational studies of the wild-type GFP, the anionic form is susceptible to mutations in the residues proximal to the chromophore, in contrast to the neutral form. Substitution of Thr203 with the aliphatic mutations of Val and Ile, which possibly disturbed hydrogen bonds with the chromophore, caused a bathochromic shift in the absorption peak of the anionic chromophore, ranging from 477 nm to 502 nm (**Table 6**). Boxer et al. theoretically explained the trend in the absorption shift among GFP mutants, based on the resonance color theory derived from the Marcus–Hush model

[76,77]. The authors treated the anionic GFP chromophore as a mixed-valence compound with superposition of two resonance forms, the phenolate- and the imidazolinone ring, both of which have charged localization centers on the oxygen atom (**Figure 13A**). The authors concluded that the absorption peak shift of the anionic chromophore was related to the driving force, which is defined by the energy difference between the two resonance forms induced by the difference in electron affinity between the two chromophoric rings. They claimed that charge destabilization on the phenolate, caused by changes such as the decline of hydrogen bonds, π−π stacking, and attachment of electron-donating groups, leads to a bathochromic shift of the absorption peak by reduction of the driving force, which means the modulation of the affinity of rings for the negative charge becomes the same level (**Figure 13B**).

A similar absorption peak shift of the protein was also reported for yellow protein (PYP). For PYP with an absorption peak at 446 nm, *the p*-coumaric acid chromophore is entirely buried within the protein and hydrogen bonds are formed between chromophoric anionic phenolate oxygen and the side chains of Tyr42 and Glu46 [78]. Quantum-chemical analysis of PYP indicated that the formation of these hydrogen bonds induces electron localization on the phenolate oxygen of the *p*-coumaric acid chromophore and causes a hypsochromic shift of the absorption peak [79]. Therefore, the weakening or disruption of the hydrogen bond between Glu46 and chromophore may reduce the hypsochromic shift by delocalizing the electron from the chromophore phenolate oxygen, causing bathochromic-shifted absorption [80]. Supporting this, mutations in the comparable size of aliphatic amino acids, E46L, E46I, and E46V, which disrupt the hydrogen bond, caused a further bathochromic shift to 475 nm, 478 nm, and 478 nm, respectively [81] (**Table 6**).

To expand the CP color palette, I developed new color variants of O-Velour (λ_{max}= 392, 506 nm), M-Velour-537 (λ_{max}= 537 nm), M-Velour-553 (λ_{max}= 553 nm) and M-Velour-554 (λ_{max}= 554 nm) with orange, and magenta colors through site-directed mutagenesis and identified a key residue, Ser155, that confers the absorption-shift.

Table 6 Summery of Red-shifted FPs

Proteins	Residues	λ_{max} (nm)	Crystal structure
PYP-E46X	E	446	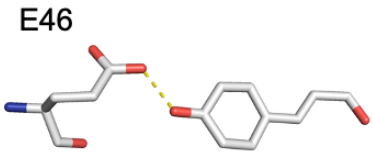
	Q	461	
	L	475	
	I	478	
	V	478	
Wild-type GFP-T203X	T	477	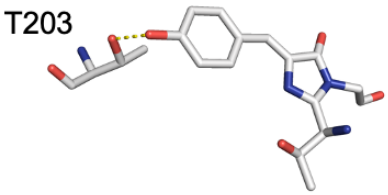
	I	501	
	V	502	
	F	506	
	Y	510	

Data of the absorption maximum of PYP and wild type GFP from references) [75–81]

(A)

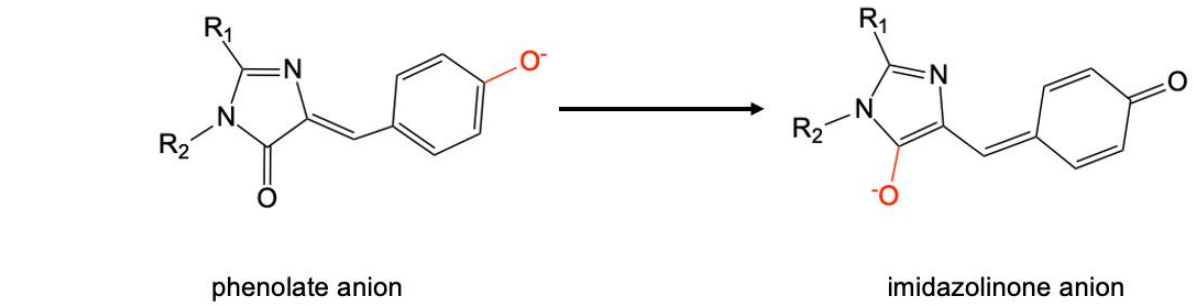

phenolate anion imidazolinone anion

(B)

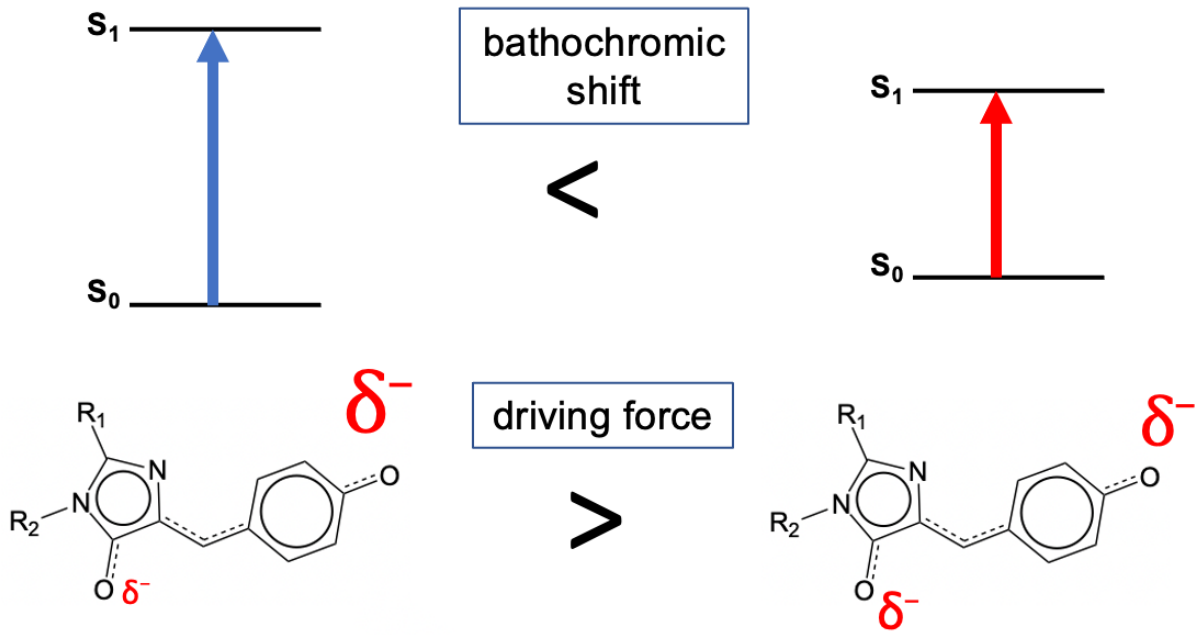

Figure 13. The two resonance forms and driving force in resonance color theory [76,77]. **(A)** The anionic GFP chromophore can adopt two resonance forms, whose negative charge lies either on the phenolate or the imidazolinone oxygen. **(B)** The ground state (S_0) of the chromophore exists as a superposition of two chromophore resonance forms. Driving force describes the difference in electron affinity between the two chromophore rings. As the driving force (blue arrow) decreases, the negative charge (size of δ^-) is less localized on each negative charge center.

3.1.2 Exploring the mutations to reduce quantum yield of mTFP1

The 440nm-480nm wavelength range has remained an optical window absence of the appropriate CP variants. The development of yellow CP with blue-cyan light absorption in this range is important to obtain CPs for the FRET acceptor of BFP to increase abatable FP-CP FRET pairs. CFPs that are excited and absorbed by blue-cyan light served as a suitable starting molecule for the development of new CPs for this purpose. Currently, there are two distinct families of CFPs: those that have a chromophore derived from the tyrosine (e.g. mTFP1 [82]) and tryptophan (e.g. ECFP [83]), respectively. Compared with mTFP1, extinction coefficients of existing CFPs with tryptophan-derived chromophore are always lower. This may be attributed to the intrinsic nature of chromophore structures [45,83–86]. mTFP1 was derived from cpFP484 from *Clavularia coral* by the process of selective directed evolution [82]. Although both *Aequorea* GFP and mTFP1 exploit chromophores generated from tyrosine, the emission peak wavelength of mTFP1 is 26 nm blue-shifted from that of EGFP. An X-ray crystallography study proposed that a positive charge on His202, which may restrict charge transfer in the excited state and cause the blue shift., is maintained by four residues (Arg75, Glu153, His202, and Glu220) of the critical quadrupole salt-bridge network [82,87]. In this study, I chose mTFP1, which exhibited higher extinction coefficient, as a starting point for mutation evolution to expand the CP color palette.

3.2 Materials and methods

Protein expression and purification. (See **Section 2.2** for details)

Protein concentration, molar extinction coefficient (ε), quantum yield (Φ) determination and spectrum measurement. (See **Section 2.2** for details)

Site directed- and saturation mutagenesis, and screening of libraries. Site-directed mutagenesis and saturation mutagenesis based inverse PCRs were performed to generate the CP color variants derived from R-Velour and to reduce the quantum yield of mTFP1, respectively. (See **Section 2.2** for details)

Crystallization and structure determination. Since the M-Velour-554 only have one mutation difference with R-Velour, Initially, the crystallization condition for the purified M-Velour-554 protein sample was completely same with that of R-Velour using hanging-drop vapor diffusion method. Optimal M-Veloiur crystals were obtained in buffer containing 17% PEG 3350, 200 mM tri-sodium citrate pH6.2, 600 mM NaCl, and 20 mM HEPES at 20°C. The crystallization drops contained 15 μM M-Velour-554. The crystals were immersed in 20% (v/v) glycerol as a harvesting buffer for cryoprotection and frozen in liquid nitrogen. See **Section 2.2** for other details. The determination of the side-chain direction of Thr155 was based on its electron density map. As a result, we conclude that the hydroxyl group of Thr151 is orientated to make a hydrogen bond with the oxygen atom of Val141 at a distance of 2.8 Å. Modeling the alternative side-chain structure of methyl carbon atoms of Thr155 oriented towards carbonyl oxygen atoms of Val141 increased the R-factor value by 0.43% and reduced the atomic distance between corresponding carbon atom and oxygen atom indicating that this model is not particularly accurate. In addition, all model structures of Thr 155 show non-hydrogen bonding distances with phenolate oxygen of M-Velour-554 chromophore.

Random mutagenesis and staggered extension process (StEP). Random mutations were introduced into the gene fragments employing error-prone PCR, followed by a staggered extension process (StEP) [88], in order to construct a library of dimTFP mutants with a lower quantum yield and restored extinction coefficiency.

DNA amplification was performed by error-prone PCR: 1 µl of DNA template (~ 200 ng) was mixed with 5 µl of 10x PCR Buffer (for Takara Taq $MgCl_2$ (+)), 5 µl of 10x dNTP mixture (dATP 2.5 mM, dTTP 9 mM, dCTP 9 mM,dGTP 2.5 mM), 2 µl of 25 mM $MgCl_2$, 2.5 µl of 8 mM $MnCl_2$ (Tris-HCl, pH8.0), 1.5 µl of 10 µM forward and reverse Primers respectively, 0.5 µl of Takara Taq (Takara Bio Inc), and 31 µl of dH_2O. The DNA library was amplified as follows: 94°C for 2 min, 94°C for 30 s, 60°C for 30 s, 72 °C for 50 s, 72 °C for 5 min, and steps 2–4 were repeated for 30 cycles. Approximately 15,000 colonies were prepared and screened with the naked eye under violet flashlight (GENUINE NICHIA LED), LED flash illuminator (WB-101, Wako) and ambient light. Colonies with more vivid yellow color with weak fluorescence were selected and inoculated in 2 ml LB media with 100 µg/ml carbenicillin, followed by mini scale preparations and sequencing determination. Mutants with better performance were selected and StEP [88], which is an *in vitro* DNA shuffling process, was performed to obtain highly diverse mutant libraries. This was done by combining 1 µl of total template plasmid DNA, 33.5 µl of dH_2O, 1.5 µl of 10 µM forward and reverse primers respectively, 5 µl 10x PCR Buffer (Takara Bio Inc), 4 µl of 2.5 mM dNTP solution (Takara Bio Inc), 3 µl of 25 mM $MgCl_2$, and 1 µl of Takara Taq (Takara Bio Inc). The DNA library was amplified as follows: 94°C for 2 min, 94°C for 30 s, 55°C for 5 s, and 4°C for 10 min, with steps 2–3 repeated for 99 cycles. The amplified dimTFP mutants were subsequently inserted into the $pRSET_B$ vector. The steps of bacterial expression and screening were consistent with those described for random mutagenesis.

pH Sensitivity Measurement and p*K*a Determination. (See **Section 2.2** for details**)**

3.3 Results and discussion

3.3.1 Site-directed saturation mutagenesis for color-alternation from R-Velour

According to the crystal structure of R-Velour mentioned in **Chapter 2**, the internal residues of Met153 and Ser155 adjacent to the chromophore form a hydrogen bond network with the phenolic oxygen of the Try61 moiety to stabilize the conformation of the trans chromophore (**Figure 5A**). Amino acid residues surrounding chromophore can affect its color properties [89]. Thus, I varied the 153rd to 155th residues in the β8-strand to explore the new R-Velour color variants by random mutagenesis. Among the ~10,000 colonies of *E. coli* expressing the library, colonies with new color were isolated followed by the sequencing and photophysical analysis. As a result, two novel CP mutants, ofCP2.2 and ofCP2.4, with visible magenta and orange colors were successfully obtained. The mutations introduced in ofCP2.2 and ofCP2.4 were T154V/S155T and M153A/T154L/S155G, respectively (**Table 7**). Because the residue, Thr154, with an outward side-chain is important to avoid dimerization of R-Velour, as previously mentioned, we introduced a 154T reverse mutation on ofCP2.2 and ofCP2.4. As a result, new color variants, M-Velour-554 and O-Velour, with mutations for only inward residues, were obtained (**Figure 14**). As with R-Velour, the quantum yields of both color variants were undetectable. M-Velour-554, with maximum absorption at 554 nm, has a 26 nm bathochromic shift from 528 nm of R-Velour. O-Velour, which mainly absorbed visible light at 506 nm, had a hypochromic shift of 22 nm, compared with R-Velour (**Figure.14B, Table 7**). The absorption peak at 392 nm of O-Velour could be attributed to the neutral chromophore, which is identical to wild-type GFP and Gamillus [51,60]. M-Velour-554 and O-Velour have visible absorption with decreased molar extinction coefficients (86,000 mM-1 cm-1 and 20,000 mM-1 cm-1) (**Table 6**). I introduced several amino acid substitutions at the 155th residue for further investigation to reveal the relationship between mutations and color change. Bathochromic-shifted mutants with magenta color were obtained by introducing alanine and valine to replace Ser155. The CP mutant of S155V (M-Velour-553) exhibited a similarly large bathochromic shift (25 nm) of absorption peak, while the S155A mutant (M-Velour-537) exhibited a smaller bathochromic shift (9 nm) (**Fig. 14B, Table 6**). Additionally, the colonies with mutation to residues that have a bulky

side-chain, such as isoleucine, leucine, methionine, or phenylalanine lost their original red color, suggesting that the alternation of these amino acids might easily impact the maturation of the R-Velour chromophore.

Table 7 Summary of R-Velour mutants

Protein	Abs[a] (nm)	Abs shift from R-Velour (nm)	Residue's site			ε[b]($M^{-1}cm^{-1}$)	Φ[c]
			153	154	155		
R-Velour	528	-	M	T	S	91,000	< 0.001
ofCP2.4	392, 506	-22	A	L	G	12,000, 15,000	< 0.001
ofCP2.2	554	+26	M	V	T	61,000	< 0.001
O-Velour	392, 506	-22	A	T	G	14,000, 20,000	< 0.001
M-Velour-537	537	+9	M	T	A	72,000	< 0.001
M-Velour-553	553	+25	M	T	V	72,000	< 0.001
M-Velour-554	554	+26	M	T	T	86,000	< 0.001

[a]Maximum absorbance.

[b]Molar extinction coefficient determined by alkali-denaturation method.

[c]Absolute fluorescence quantum yield determined by integrating sphere.

(A)

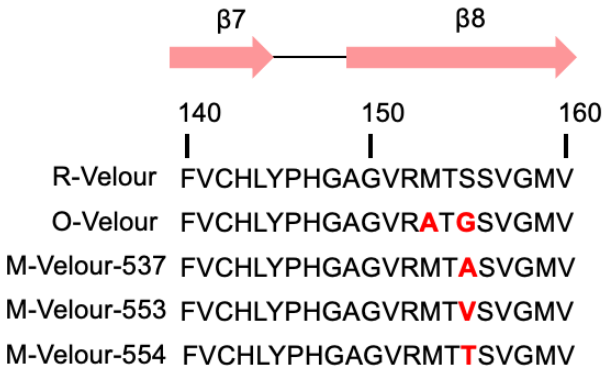

(B)

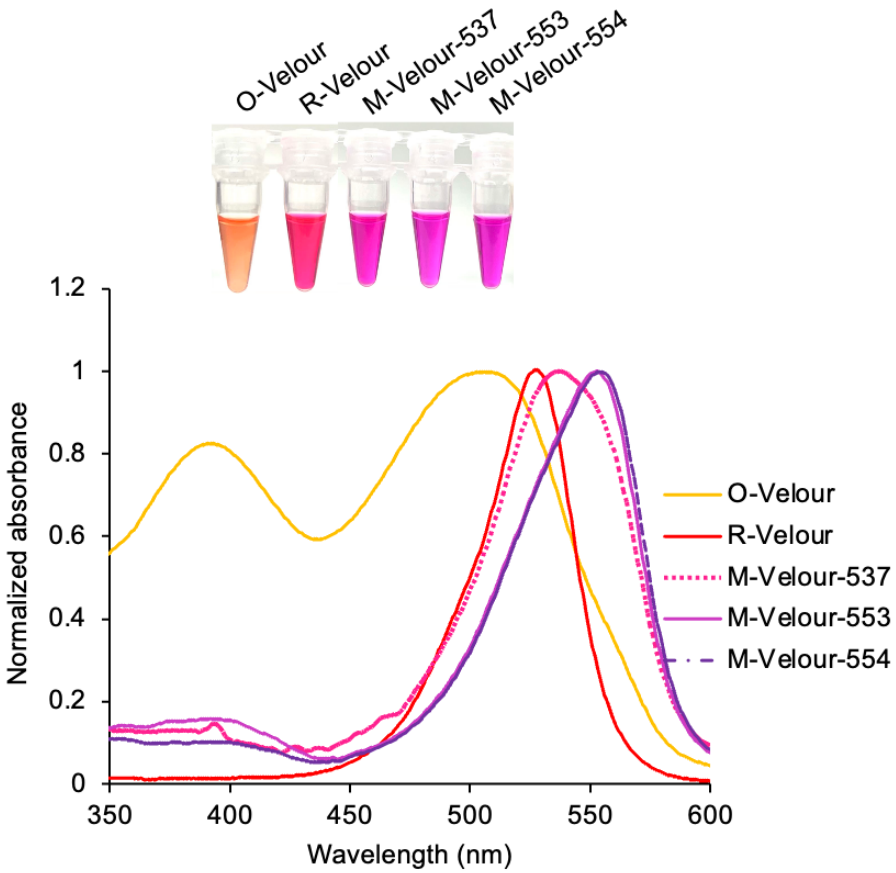

Figure 14. Evolution of new color variants of O-Velour, M-Velour-537, M-Velour-553, and M-Velour-554 from R-Velour. **(A)** Amino acids sequence alignment (140th-160th). The mutations are highlighted in bold red. **(B)** Normalized absorption spectra of purified of O-Velour, M-Velour-537, M-Velour-553, M-Velour-554, and R-Velour, which were measured at 10 μM, pH7.5 at 25°C.

3.3.2 Structural mechanism of color-tuned R-Velour variants, M-Velour-554

The mutational study showed Ser155 is a crucial residue for color change. For understanding the color alternation mechanism from the structural aspect, I crystalize the M-Velour-554 which is the red shifted mutant from R-Velour with single substitution S155T. Purified M-Velour-554 protein with an N-terminal 6xHis-tag was crystalized and the 3D structure was determined using X-ray crystallography. Different with R-Velour, the crystal of M-Velour-554 belonged to $P2_12_12_1$ space group, and the structure was refined to a final R_{work}/R_{free} of 20.92/24.63%, at a resolution of 2.5 Å (**Table 8**). The model comprised 4 protomers (**Figure 15**). Same with R-Velour, each protomer of M-Velour-554 within the asymmetric unit has the typical β-can fold of FP and is composed of an 11-stranded β-barrel, with each β sheet linked by a loop region and the circularized chromophore consisting of a tripeptide (Gln60-Try61-Gly62) located in the middle part of the α2-helix motif penetrating the central axis of the β-barrel. The chromophore of the M-Velour-554, 4-(p-hydroxybenzylidene)-5-imidazolinone group with two rings consisted of a central imidazolinone moiety and *a p*-hydroxybenzylidene substituent (**Figure 15, 16**). Within the asymmetric unit, the Root mean square deviation (RMSD) between each strand of protomer B and the corresponding strands of protomer A, protomer C, and protomer D is less than 0.2 Å (for all C^{α} atoms). Thus, it is reasonable to assume that the overall structures of a β-barrel of eleven strands of the protomers are identical. In addition, the Protomer B of M-Velour-554 was almost identical to that of R-Velour, where strand 8 that containing S155T mutation exhibited the relatively higher deviation value (0.272 Å) with R-Velour (**Figure 17**).

In all protomers of M-Velour-554, the two-ring chromophore adopts both *trans*-conformation and *cis*-conformation between the Cα2-Cβ2 bond. The electron density map distinctly indicates that the phenoxy group is predominantly in a *trans*-noncoplanar configuration (**Figure 16**). The *cis-trans* ratio is 0.3/0.7, which was calculated from the B-factor value of the phenol side chain of tyrosine in the chromophore. Optimal M-Velour-554 crystals were obtained in buffer containing 17% PEG 3350, 200 mM tri-sodium citrate pH6.2, 600 mM NaCl, and 20 mM HEPES at a temperature of 20°C. Since the pH value of the harvesting buffer was closed to that of p*K*a M-Velour-554 (p*K*a=5.1), it was speculated that the *cis-trans* isomerization of the

M-Velour-554 chromophore phenolate ring might be related to its protonation [90,91], which is supported by the evidence of the *cis*-conformation of the Gamillus chromophore at pH3.0 [51]. It was unclear whether the detail structure between all protomer chromophores is same or not. The Electron density map was not enough to determine the structural coordinate (**Figure 16**). Compared with backbone, the electronic density in chromophore part is lower (**Figure 16**). Among all protomers, only protomer B has a very clear electron density that is independent of all other protomers (**Figure 16**). Thus, protomer B was used for the following analysis.

To study the 26 nm bathochromic shift of M-Velour-554 from R-Velour, I compared their structures. Firstly, I analyzed residues 138th -143rd in β7-strand and residues 154th-159th in β8-strand among Protomer A, B, C and D (**Figure 18**). The β7- and β8-strands in M-Velour-554 are locked under four hydrogen bonds (Hydrogen bonds form between Gly158-Leu138, T155-V141, and T154-H143) (**Figure 18A**). In the case of R-Velour, three hydrogen bonds are formed between Gly158-Leu138 and T154-H143 (**Figure 18B**). The hydroxy-methyl side chain of Thr155 in the M-Velour-554 structure forms a hydrogen bond with the Val141 in β7-strand with the distance of about 2.8 Å. However, Ser155 in R-Velour roughly 5.4 Å distant from Val141 shows no conceivable hydrogen bond between them. In addition, Ser155 in the β8-strand of the R-Velour directly formed hydrogen bond with chromophore (**Figure 19A**). However, around 6.8 Å distance between the side-chain of Thr155 and the phenolate oxygen of the M-Velour-554 chromophore, indicates no conceivable hydrogen bond between them (**Figure 19B**). Thus, in M-Velour-554, Thr155 forms hydrogen bonds only with Val141 but not with the phenolate oxygen of the chromophore. Apparently, the significant structural characteristic difference between M-Velour-554 and R-Velour is the presence or absence of hydrogen bonds between residues on 155 and phenolate oxygen. This difference in structural feature supports the mechanism of color tune of M-Velour-554 in **section 3.4**.

Table 8 Data collection and refinement statistics

	M-Velour
Data collection	
Light source	SPring-8 BL44XU
Wavelength (Å)	0.9000
Space group	$P2_12_12_1$
Cell dimensions	
a, b, c (Å)	105.0, 106.1, 157.3
α, β, γ (°)	90, 90, 90
Resolution (Å)	47.01-2.50(2.65-2.50)
R_{merge}	0.072(0.727)
R_{meas}	0.084(0.838)
$R_{p.i.m.}$	0.047（0.434）
$I/\sigma I$	10.45(1.68)
$CC_{1/2}$	0.996(0.709)
Completeness (%)	96.1(97.6)
Multiplicity	3.6(3.6)
Refinement	
Resolution (Å)	47.01-2.50
Number of reflections	
Observed	210897(34587)
Unique	59261(9563)
R_{work}/R_{free}	0.2092/0.2463
Number of atoms	
Protein	6938
Ligand/ion	0
Water	61
B-factors ($Å^2$)	
Protein	65.5
Ligand/ion	-
Water	49.8
R.m.s. deviations	
Bond lengths (Å)	0.0100
Bond angles (°)	2.0388
Ramachandran plot (%)	
Most favored	98.0
Allowed	2.0
Outliers	0

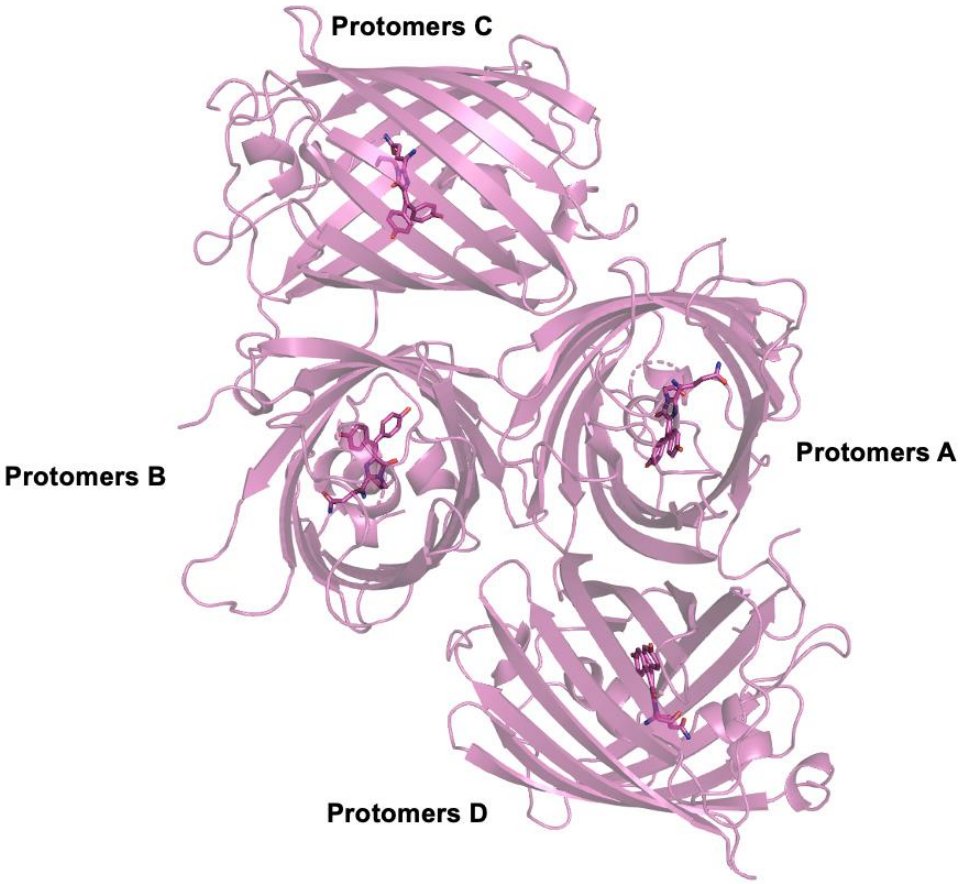

Figure 15. Crystal structure of M-Velour-554 (2.5 Å). *P*$2_12_12_1$ crystal contains 4 protomers in asymmetric unit was observed. The circularized chromophore consisting of a tripeptide (Gln60-Try61-Gly62) of four protomers located in the middle part of the α2-helix motif penetrating the central axis of the β-barrel.

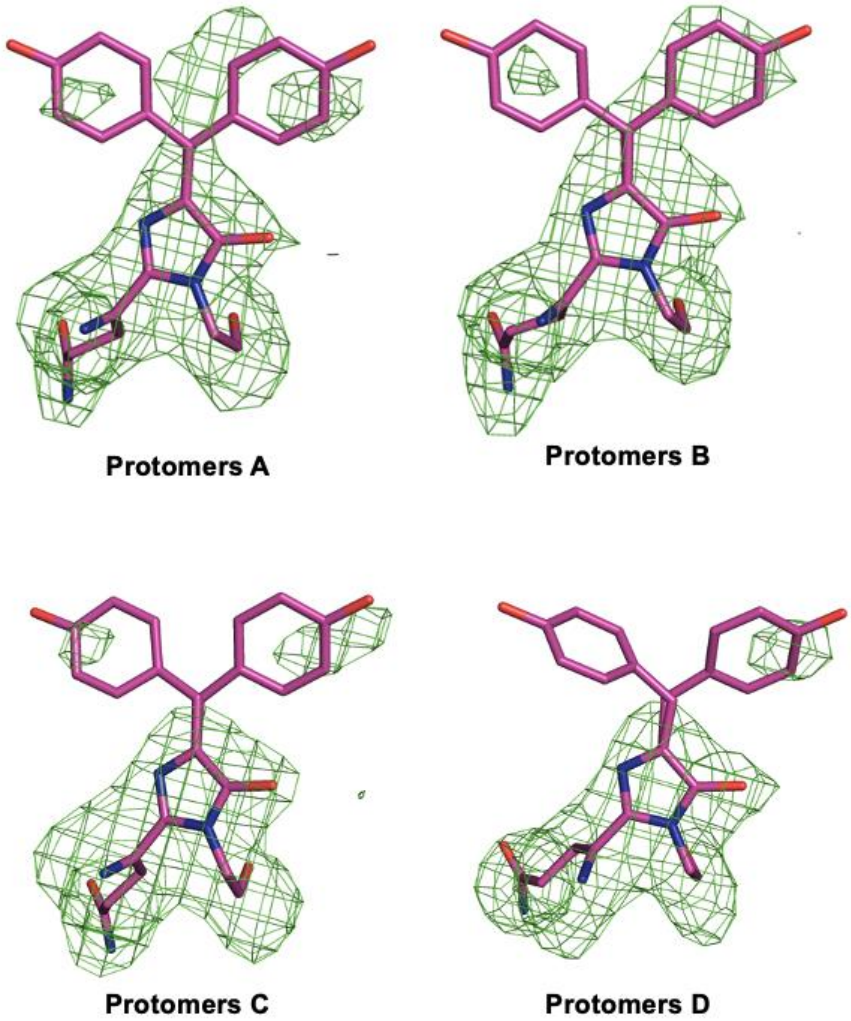

Figure 16. *Fo-Fc* map of the M-Velour-554 chromophores. Comparison of the electron density of M-Velour-554 chromophores in all protomers. The chromophores of all protomers are depicted as stick form. The omit map (*F*o-*F*c), contoured at 3.0σ, is depicted as a green mesh. The *cis-trans* chromophore conformation is colored by magenta.

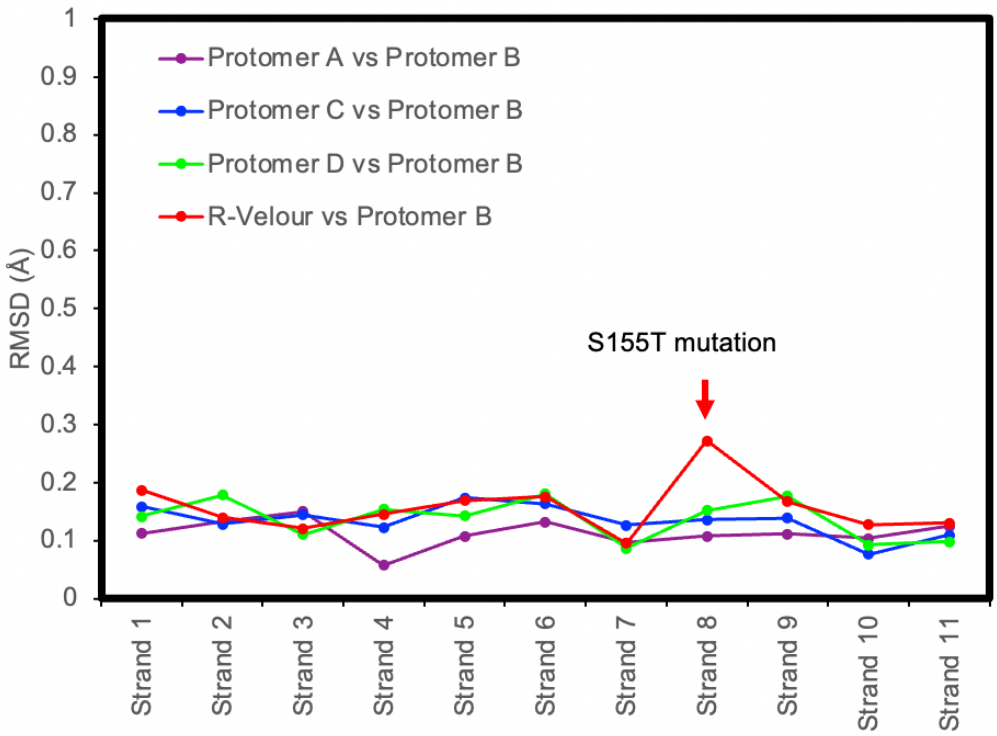

Figure 17. Root-mean-square deviation (RMSD) analysis between Protomer B with other three M-Velour-554 protomers and R-Velour, respectively. The slightly higher RMSD value for protomer B with R-Velour in strand 8 is due to allosteric changes induced by S155T mutation.

(A)

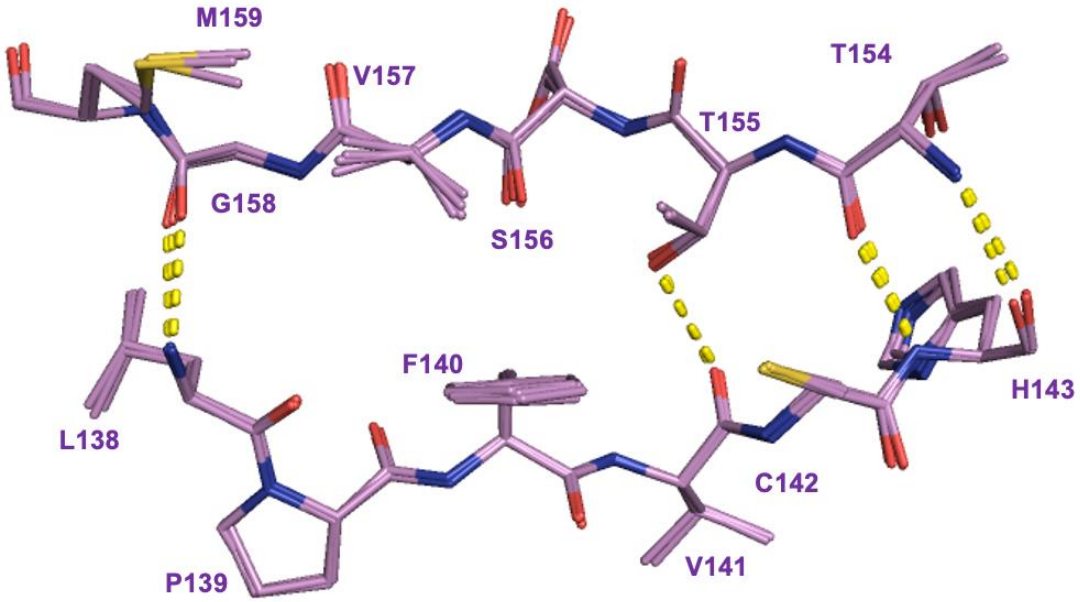

(B)

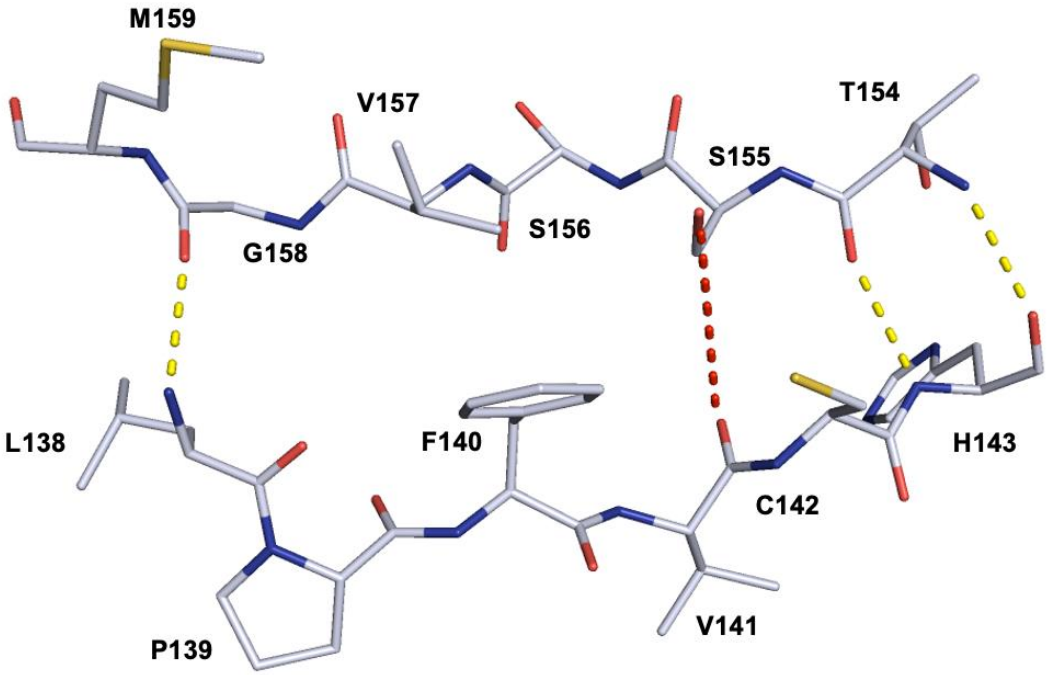

Figure 18. Ball and Stick Representation of residues 138th -143rd in β7-strand and residues 154th-159th in β8-strand in the M-Velour-554 and R-Velour. (A) Superposition of residues 138th -143rd in β7-strand and residues 154th-159th in β8-strand between all corresponding protomers of the M-Velour-554 structure (Magenta).

H-bond pattern bridging the β7-strand and β8-strand is described. Yellow dash lines represent hydrogen bonds. **(B)** Residues 138th -143rd in β7-strand and residues 154th-159th in β8-strand of R-Velour (Grey). H-bond pattern bridging the β7-strand and β8-strand in R-Velour is shown. The distance between hydroxymethyl side-chain of Ser155 with phenoxy oxygen is shown as red dash line (5.4 Å).

(A) (B)

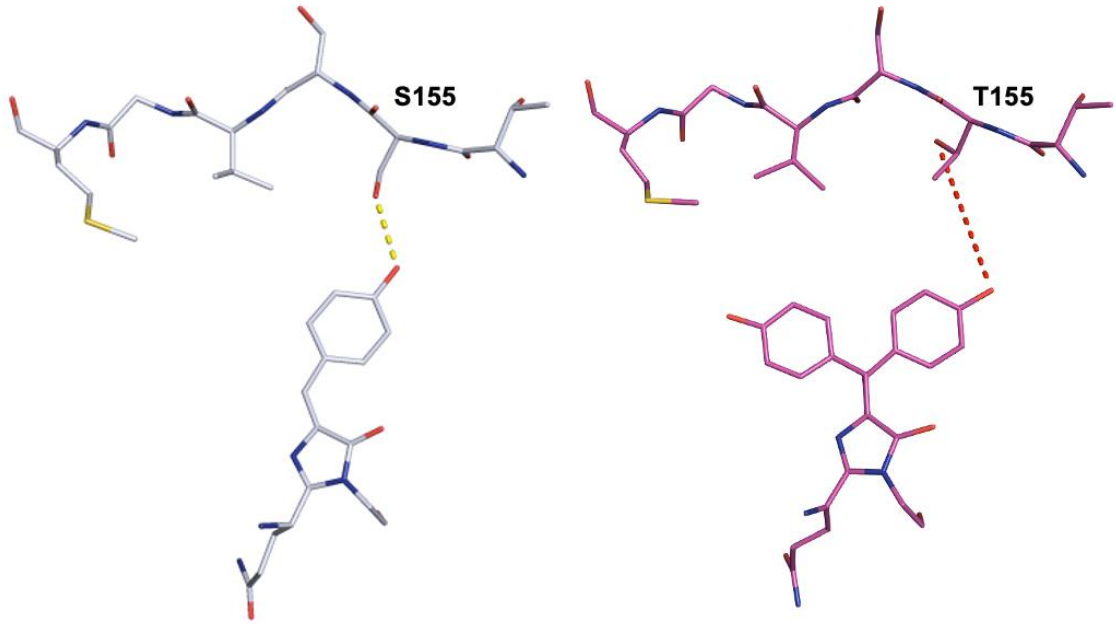

Figure 19. Ball and Stick Representation of chromophores. (A) In R-Velour, S155 forms hydrogen bonds (Yellow dash line, 2.8 Å) only with the phenolate oxygen of the chromophore. **(B)** In M-Velour-554, the long distance (Red dash line, 6.8 Å) between T155 with phenolate oxygen indicates the absence of hydrogen bond.

3.3.3 Dvelopment of the new yellow CPs from mTFP1 (dimTFP variants)

To develop the new yellow CP, mTFP1 was my first choice as a parental template for introducing site-directed mutations in combination with different rounds of random mutagenesis with library screening. I analyzed the crystal structure of mTFP1 for the efficient finding of mutation points without disturbing absorption spectrum features and higher molar extinction coefficient. The *cis*-type chromophore of mTFP1 forms a hydrogen bond with the imidazole of His168 with its phenolated oxygen. In addition, the amino acids Arg75, Glu153, His202, and Glu220 joined together to create a quadrupole salt-bridge network that is situated in close proximity to the mTFP1 chromophore. His168 and His202 have been reported to be the residues most responsible for hypsochromic shifting the fluorescence emission [82,92]. Moreover, it has also been demonstrated that the hydroxyl group of Thr78 is hydrogen-bonded to the guanidine group of Arg75 and is an important part of the quadruple salt bridge network that causes the blue shift in fluorescence [92] (**Figure 20**).

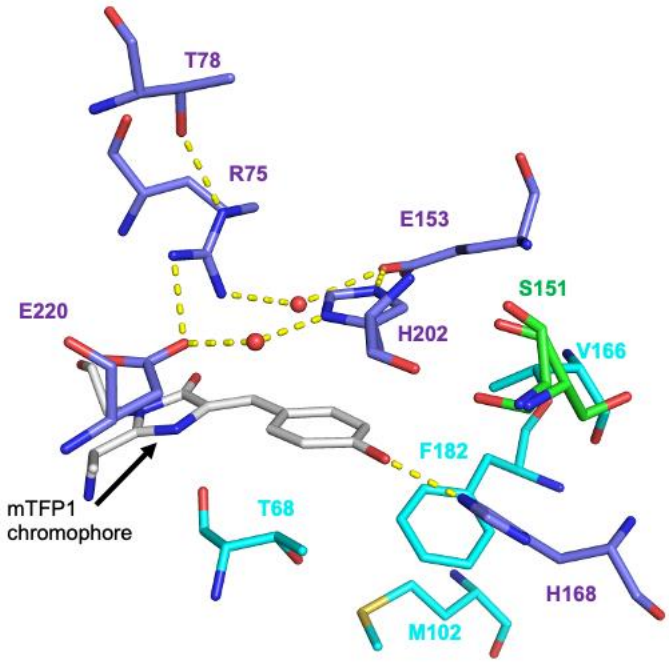

Figure 20. mTFP1 chromophore environment (PDB: 2hqk). The chromophore environment is depicted in a stick representation for mTFP1. The mTFP1 chromophore (Grey) is indicated with black arrow. The amino acids which are reported to be important for hypsochromic shifting are colored by purple. The amino acids which is

essential for blue shifting in this study is colored by green. The amino acids which are key for reducing the brightness and manufacture new CP variant in this study is colored by cyan color. Hydrogen bond interactions are shown as yellow dashed lines and water molecules as red spheres.

Previous research has shown that CP always uses a non-coplanar chromophore between its phenolic and imidazolinone moiety. In the case of DimVenus [3] and DrakVenus [30], Y145W and H148V introduced into the residues proximal to the phenolic ring might disrupt the coplanarity of the chromophore in Venus. Following that hypothesis, I targeted Ser151 close to the chromophore phenolic oxygen to reduce brightness. I introduced random mutations simultaneously at the position of 149^{th}-151^{st}. The mutant library was screened by employing a colony-based fluorescence imaging system. Contrary to my expectations, the screening process uncovered that the library contained both bright cyan- and green-fluorescent mutants. As can be easily predicted, mutants with bright cyan fluorescence have Serine at 151^{st} identical with mTFP1. The green fluorescent mutants with 482-483 nm excitation and 501-502 nm emission wavelengths contained Alanine, threonine, or glycine at the 151st residue (**Table 9**). I obtained one mutant with the brightest green fluorescence mTFP1-D149G/A150S/S151R named mTFP1-G. Photophysical analysis revealed that mTFP1-G has a higher extinction coefficient of 81,000 $M^{-1}cm^{-1}$ and a similar quantum yield of 0.89 compared with those of mTFP1. Excitation and emission peaks of mTFP1 are 483 nm and 502 nm, and those are around 19 nm bathochromic shifted from that of mTFP1. Next, I site-directly introduce bulky mutations (Try, Phe, and His) at the 151st residue intended to disrupt the planarity of the mTFP1 chromophore. Even after prolonged incubation at room temperature for approximately 48 hours, the colonies that expressed the mTFP1 mutant did not show any color and fluorescence under blue light excitation.

Table 9 Summary of mTFP1 mutants with introduced mutation at position 151st

FPs	151st	λ_{ex}[b] (nm)	λ_{em}[b] (nm)	Ɛ[c] ($M^{-1}cm^{-1}$)	Φ[d]
mTFP1	S	462	492	68,000	0.85
mTFP1-G	R	483	502	81,000	0.89
mTFP1-M1	A	483	502	No data	No data
mTFP1-M2	T	483	502	No data	No data
mTFP1-M3	G	482	501	No data	No data

[a]Maximum excitation wavelength.

[b]Maximum emission wavelength.

[c]Molar extinction coefficient determined by alkali-denaturation method.

[d]Absolute fluorescence quantum yield determined by integrating sphere.

Based on the mTFP1 evolution history from the previous report, I selected a few mutations which might affects the quantum yield of mTFP1. Residue of Thr68 is situated directly below the mTFP1 chromophore (**Figure. 20**). The 68th residue of the cFP484, which is the origin of mTFP1 with smaller QY 0.48, is Asparagine. To achieve my goal of reducing the QY of mTFP1, I introduced the T68N mutation and obtained a mutant (dimTFP1.0) with the decreased quantum yield from 0.89 to 0.35.

The molar extinction coefficient of dimTFP1.0 is slightly reduced from 64,000 $M^{-1}cm^{-1}$ to 56,000 $M^{-1}cm^{-1}$. Crucially, dimTFP1.0 preserves the blue light absorption with 450 nm absorption maximum, which is fit with my objectives. Residue of V166 is situated closed to the phenolate moiety, and the I166V has been reported to increase the quantum yield in mTFP1. Thus, I introduced V166I mutation and obtained the mutant of dimTFP1.1 with the decreased quantum yield at 0.27 and the improved molar extinction coefficient at 83,000 $M^{-1}cm^{-1}$. The absorption maximum of dimTFP1.1 at 448 nm is comparable with that of dimTFP1.0. To further reduce the quantum yield of dimTFP1.1, I preformed random mutagenesis. Mutants with decreased brightness under blue light excitation but exhibit vivid yellow color under the ambient light were screened. As a result, the variants of dimTFP1.2 (Mutation: T46A, M102L, K130E, and D229N, ε= 79,600 $M^{-1}cm^{-1}$; QY= 0.11, $\lambda_{max,\ abs}$= 462 nm), dimTFP1.3 (Mutation: F182W, ε= 58,000 $M^{-1}cm^{-1}$; QY= 0.036, $\lambda_{max,\ abs}$= 467 nm) and dimTFP1.4 (Mutation:

M102L, ε= 80,000 $M^{-1}cm^{-1}$, QY= 0.13, $\lambda_{max, abs}$= 459 nm) with the weak brightness were selected. To restore the extinction coefficient of dimTFP1.3 and reduce the quantum yield of dimTFP1.2 and dimTFP1.4, I conducted error prone PCR following colony screening by using them as the templates. Finally, I screened three yellow CP candidates, dimTFP-460 derived from dimTFP1.4 (Mutation: L102I, ε = 65,000 $M^{-1}cm^{-1}$, QY= 0.047, $\lambda_{max, abs}$= 460 nm), dimTFP-465 derived from dimTFP1.2 (Mutation: T46A and F182Y, ε = 67,000 $M^{-1}cm^{-1}$, QY= 0.053, $\lambda_{max, abs}$= 465 nm) and dimTFP-470 derived from dimTFP1.3 (Mutation: N26Y and N47S, ε = 70,000 $M^{-1}cm^{-1}$, QY= 0.018, $\lambda_{max, abs}$= 475 nm), with the weaker brightness and higher molar extinction coefficient (**Figure 21 and 22**).

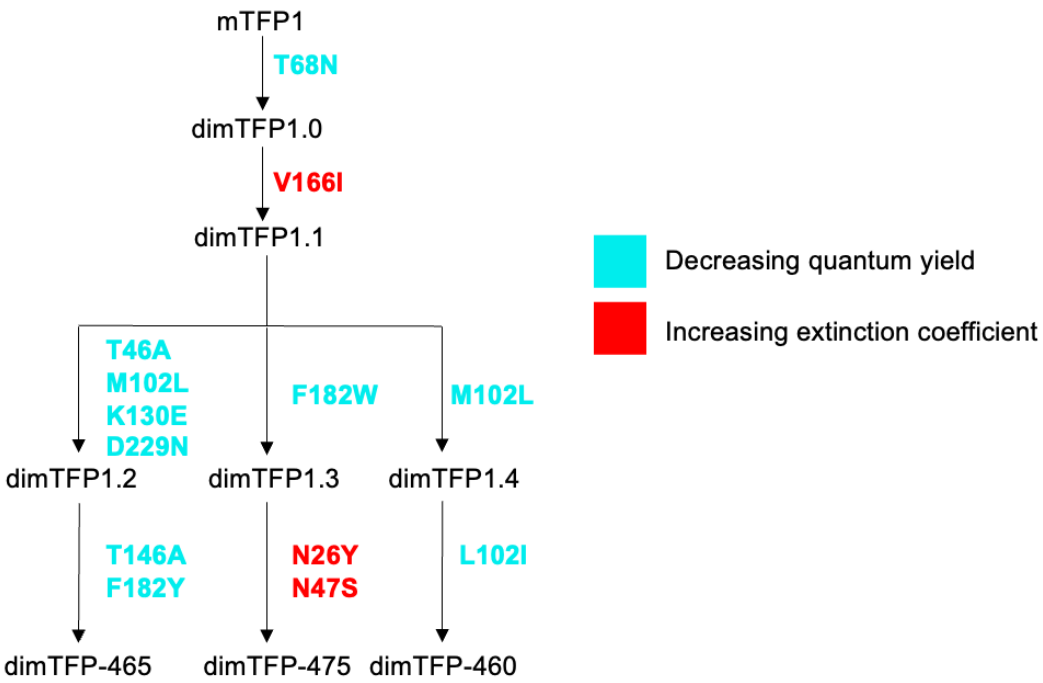

Figure 21. dimTFP lineage. Evolution of Y-Velour variants from mTFP1. Mutations colored by cyan decreased the quantum yield of mTFP1 variants. The mutations color by red increased the extinction coefficient of mTFP1 variants.

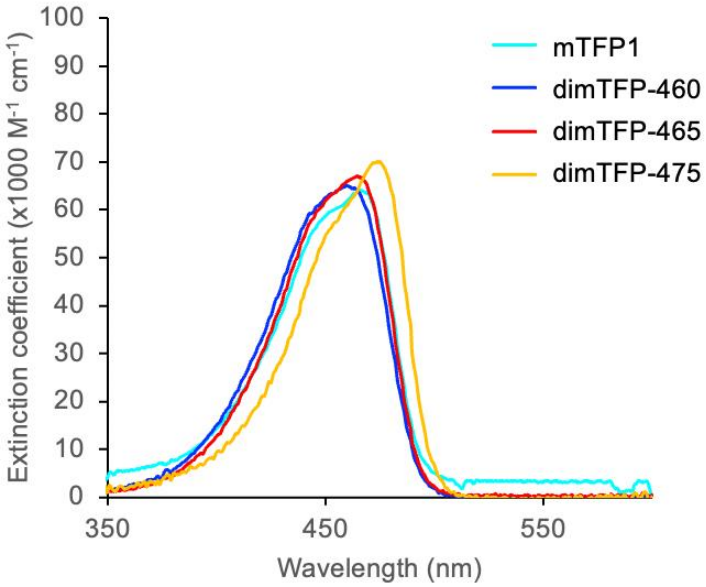

	Residues					QY	ε ($M^{-1}cm^{-1}$)	$\lambda_{max, abs}$ (nm)
	47	68	102	166	182			
mTFP1	N	T	M	V	F	0.85	64,000	466
dimTFP-460	-	N	I	I	-	0.047	65,000	460
dimTFP-465	-	N	L	I	Y	0.053	67,000	465
dimTFP-475	S	N	-	I	W	0.018	70,000	475

Figure 22. Y-Velour lineage. Upper: Molar extinction coefficient spectra of mTFP1 (cyan solid line), Y-Velour-460 (blue solid line), Y-Velour-465 (red solid line) and Y-Velour-475 (orange solid line), measured at 30 μM, pH7.5 at 25°C. **Below:** Photophysical analysis of mTFP1 and Y-Velour variants. Mutations colored by cyan decreased the quantum yield of mTFP1 variants. The mutations color by red increased the extinction coefficient of mTFP1 variants. (QY: Absolute fluorescence quantum yield determined by integrating sphere. ε: Molar extinction coefficient determined by alkali-denaturation method. $\lambda_{max, abs:}$ Maximum absorption wavelength.

3.4 Conclusion and Discussion

In the mutation study of R-Velour, the substitution of Ser155 near the phenolic acid portion of the chromophore effectively induced the absorption peak shift. Based on the aforementioned mutational studies on wild-type GFP (**Section 3.1.1**), I considered that significant absorption bathochromic-shift of R-Velour mutants by single-site mutations of S155V (M-Velour-553) and S155T (M-Velour-554) might cause by the destruction of the hydrogen bond between Ser155 and phenolic oxygen of chromophore, which decreased the localization of electron charge on the phenolic oxygen (**Figure 23**). Mutation to a smaller hydrophobic side-chain S155A (M-Velour-537) that might have difficulty forming hydrogen bonds and showing the smaller bathochromic-shift suggests less delocalization of electron charge on phenolate oxygen. O-Velour, which showed a 22 nm hypsochromic shift, contains double mutations of M153A/S155G. The difference between O-Velour and two M-Velour mutants (M-Velour-553 and M-Velour-554) lies in the 153rd and 155th residues. Mutations of M153A and S155G in O-Velour might cause a hydrogen bond with a water molecule that fills the larger space produced by the substitution of the smaller alanine and glycine. Such hydrogen bonds might maintain or enhance the effect of electron charge localized on the chromophore phenolic oxygen, resulting in a hypsochromic shift. Further determination of the structures of R-Velour color variants is required to support this assumption. As a result, the crystal structure of M-Velour-554 was determined to a 2.5 Å resolution. I found that there has no hydrogen bond between Thr155 with phenolate oxygen due to the far distance. Thus, in M-Velour-554 with red-shifted absorption Thr155 forms hydrogen bonds only with Val141 but not with the phenolate oxygen of the chromophore, which consistent with my speculation. However, the speculative evidence for the small bathochromic- or hypsochromic shift in M-Velour-537 and O-Velour needs to be supported by crystal structure analysis in the future.

Taken together, a single replacement of Ser155 with hydrophobic residues can optimize the absorption spectrum of R-Velour in the range of 528–554 nm. These new color variants can compensate for the gaps in the current CP color window. In addition, based on the recently proposed spectrum shift theory, I explained the spectrum shift

with the difference in the state of the hydrogen bonds from the chromophore phenolate oxygen. That was further supported by disruption of the hydrogen bond in the crystal structure of the variant M-Velour-554 with the bathochromic shift. These findings may support further development of R-Velour variants with useful absorption characteristics for bioimaging.

To develop CPs with shorter absorption wavelength, I selected mTFP1 as template for mutation evolution. Based on previous reported work, Thr68 is likely the key residue that contributes the most reduction in fluorescence quantum yield. Certainly, I have identified the substitutions T68N that significantly reduced the brightness of mTFP1. Following the mutagenesis using mTFP1 as template, I successfully obtained three yellow CP candidates, dimTFP-460, dimTFP465 and dimTFP475, which are expected to be particularly useful as FRET acceptors for blue FP donors in the FLIM-FRET measurement. In addition, I discovered that mutations to Ser151 of mTFP1 results in a bathochromic shift around 19 nm in the fluorescence emission of the mTFP1 chromophore. This information will be beneficial for expanding the diversity of new FP color variants derived from mTFP1.

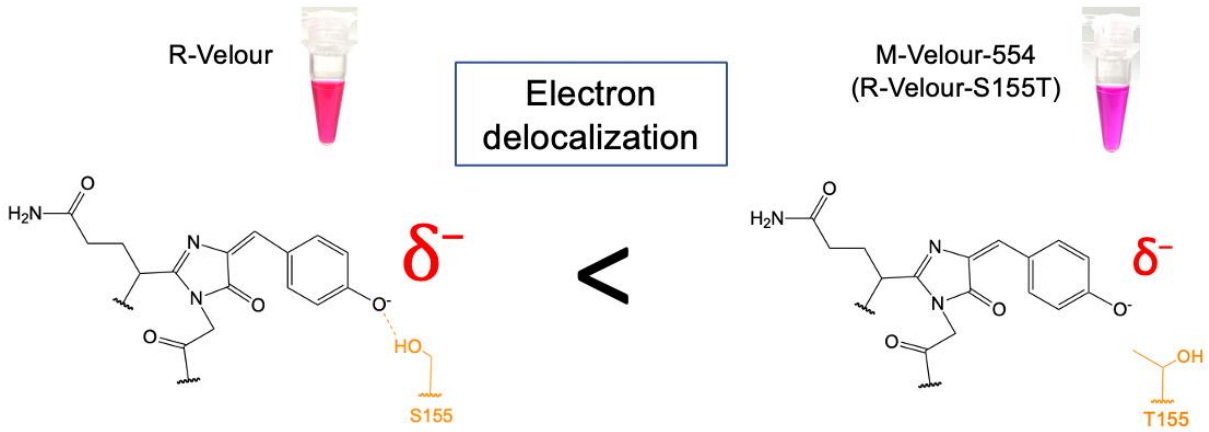

Residue	S155	T155
Absorption maximum (nm)	528	554

Figure 23. The chromophore environment of the M-Velour-554 color variant is depicted in a chemical structure. Disruption of the hydrogen bond leads to electron delocalization (Size of δ^-) on the phenolic oxygen of the chromophore, causing the bathochromic shifted absorption as observed.

CHAPTER 4

Development of yellow chromoproteins for FRET measurement with donor of violet fluorescence protein

4.1 Introduction

With FRET technology and genetically encoded FRET biosensors, signaling molecules in living cells can be seen with high spatiotemporal resolution [20]. As I mentioned above, CPs have been preferentially applied as acceptor or quencher for genetically encoded indicators in intensity based FRET imaging or fluorescence lifetime based FLIM-FRET imaging [3,16–19,93,94], which requires only donor fluorescence for FRET detection. There are several benefits by using the CPs in FRET imaging and FLIM: (1) By reducing fluorescence leakage from CP acceptor into the donor emission channel, the FRET dynamic range can be increased by more precise measurements of the donor fluorescence lifetime. (2) Since fluorescence contamination from FRET acceptors can be ignored, broader bandpass emission filters can be employed, which helps provide maximum attenuation of excitation light during the FLIM observation. By reducing the excitation intensity, CP acceptors can minimize the risk of phototoxicity. (3) Due to the fact that FRET pairs containing CPs occupy a small section of the wavelength spectrum, multiple FPs of different hues can be utilized concurrently for dual-color or multi-color imaging [95].

CP acceptors with the report of FLIM-FRET was generally used for the FRET donor of GFP- or RFP. Two dark YFP mutants were firstly engineered from a YFP with reduced quantum yield to act as FRET acceptors to mEGFP. This construct is known as REACh (Resonance Energy-Accepting Chromoprotein) [3]. Several years later, powerful FLIM-FRET acceptors for EGFP donor, ShadowG and ShadowY, were developed [17,18]. Their extremely low quantum yield is roughly 10 times lower than that of REACh. Thus, the EGFP-ShadowG FRET pair allows imaging free from the bleedthrough of the fluorescence of accepter into the detection channel for RFPs.

Under the two-photon excitation at 980 nm for both mEGFP and mCherry FPs, dual color imaging of intensity–based mCherry-ERK translocation and FLIM-FRET–based Ras indicator (Donor: mEGFP, Acceptor: ShadowG) was achieved [17]. To expand the CP application for FRET acceptor of RFP, a CP darkmCherry has been developed from mCherry. darkmCherry was used as the FRET acceptor for mRuby2 that is a bright RFP [16]. To simultaneously monitor Ca^{2+} dynamics and Rho GTPase activity in astrocytes, the author used a FRET-based RhoA indicator composed of mRuby2 and darkmCherry, which only required to detect the emission spectrum range of mRuby2 (550-650 nm) under the two-photon excitation for FLIM-FRET measurements, together with GFP based genetically encoded Ca^{2+} indicator G-GECO. Furthermore, the novel CP called ShadowR with the reduced interaction with non-specific binding to intracellular proteins and improved expression was creared, which can be paired with RFP of mRuby or mScarlet for FLIM-FRET measurement in living cells [19].

Although various CPs have already been developed as FRET acceptor for GFP or RFP, development of the new CP with shorter wavelength absorption as acceptor for violet fluorescent protein (VFP) has not been attempted. Recently, Sugiura K et al. of our laboratory developed the shortest emission wavelength of VFP named Sumire, which has the violet fluorescence emission of 414 nm from a hydrated chromophore [96]. Compared with another VFP Sirius [97], Sumire showed the higher extinction coefficient (Sumire: 20,000 M^{-1} cm^{-1}, Sirius: 15,000 M^{-1} cm^{-1}) value and enhanced quantum yield (Sumire: 0.70, Sirius: 0.24). Moreover, Sumire exhibited 3.3 times brighter fluorescence emission than Sirius when expressed in HeLa cells. It has also been demonstrated that FP FRET probe pairs can be established between Sumire and cp173-T-Sapphire (A circular permutation of Long stoke shift GFP) [96].

Here, I aim to develop a new CP as the FRET acceptor for Sumire. R-Velour type CPs with extremely lowest quantum yield and high extinction coefficient is considered as the good template for generating the new CP variants with the shorter wavelength absorption.

4.2 Materials and methods

Gene construction. For gene construction of FRET pairs construction, the cDNA of Sumire was amplified with restriction enzyme sites of *Bam*HI and *Kpn*I. The gene fragement of Y-Velour, Y-Velour-C22R, mTagBFP2, and mT-Sapphire was amplified with *Kpn*I/*Eco*RI sites. Vectors (Digested with BamHI/*Eco*RI) of pRSET$_B$ (Invitrogen) was used for the bacterial protein expression and pcDNA3.0 (Invitrogen) was used for mammalian expression. In the case of Ca^{2+} indicator, the calcium sensing domain derived from the C-terminal globular domain of toadfish Troponin C (TnC) was amplified from Twitch-2B [22] plasmid with the *Sph*I and *Sac*I restriction enzyme sites. In the gene construction of vyCa^{2+}, minimal calcium-binding moiety of TnC was fused between the Sumire and Y-Velour-C22R. The constructed genes were transformed into *E. coli* JM109(DE3) or XL-10 Gold and were cultured in the LB medium with 100 µg/mL carbenicillin for overnight incubation at 37ºC.

Protein expression and purification. (See **Section 2.2** for details)

Photophysical analysis of Y-Velour. Molar extinction coefficient (ε) of Y-Velour was calculated from the determined protein concentrations. Protein concentration was measured by the Bradford assay (Bio-Rad). The absorption spectrum was measured at 250-500 nm. According to Beer-Lambert's law, ε can be determined as: $A_{peak\text{-}CP}/cl$. "$A_{peak\text{-}CP}$" is the Y-Velour absorption at the peak wavelength, "*c*" is the protein concentration, and "l" is the optical path length (cm). The determination of absolute fluorescence quantum yield (Φ) and absorption spectrum were described in **Section 2.2**.

***In vitro* characterization.** Fluorescence spectrometer (F-7000, Hitachi High-Technologies) was used for the measurement of the fluorescent emission spectra of FRET pairs. FRET efficient was calculated under trypsin (FUJIFILM Wako Pure Chemical) treatment. 100 µg/mL trypsin was prepared as the stock with 0.01 M Tris-HCl pH8.0 buffer. Before the measurement, proteins were diluted in a 20 mM HEPES buffer (pH7.4) of 200 µL to 1 µM and loaded into a quartz cuvette. The fluorescence intensity of FP donor emission peak was measured in the presence of acceptor as F_{da}.

Later, 2 µL 100 µg/mL Trypsin was added into protein solution and incubate 10 min at room temperature. After proteolysis by trypsin, the donor fluorescence intensity was dequenched from F_{da} to F_{d}. The efficiency of FRET is given by the extent of dequenching of the donor when the acceptor is removed with the following equation: $FRET_{in\ vitro}$ = 1- (F_{da}/ F_{d}). At least three times repetition was required, and their average values were taken for subsequent analysis. Ca^{2+} titrations were done by the reciprocal dilution of Ca^{2+}-saturated and Ca^{2+}-free buffers comprising 10 mM MOPS, 100 mM KCl, and 10 mM EGTA with or without 10 mM Ca^{2+} added as $CaCO_3$ at pH7.2 and 25°C for fluorescence measurement. The peak of the donor fluorescence was used for the calculation. The apparent K_D value was calculated using a Ca^{2+} titration curve and nonlinear regression analysis. Sigmodal binding curves were fitted to the data using Origin7 software to derive the single Hill equation (OriginLab).

Random mutagenesis and staggered extension process (StEP). To generate a library of FRET pair mutants (Sumire-Y-Velour) with enhanced FRET efficient, random mutations were only introduced into the Y-Velour gene fragments by error-prone PCR, followed by StEP [88]. See **Section 4.2** for details of error PCR and StEP. As a result, approximately 15,000 colonies were prepared and screened with the naked eye under violet flashlight (GENUINE NICHIA LED) and ambient light. Colonies with more vivid yellow color with weak fluorescence were picked and inoculated in 2 ml LB media with 100 µg/ml carbenicillin, followed by mini scale preparations and sequencing determination.

Cell culture, transfection. HeLa cells were cultured with Dulbecco's modified Eagle medium (DMEM/F12 with phenol red; D6046, Sigma-Aldrich) supplemented with 10% fetal bovine serum (FBS; Biowest) in a 5% CO_2 incubator at 37°C. All the cell culture expriments were performed in 10 cm cell culture dishes (Thermo Scientific Nunc Petri dish) using 10 ml of DMEM/F12 as a medium. When the cell density reacheed 70-80% or higher, subculture was performed in the following procedure. We removed the DMEM medium with an aspirator and then wash the cells with 2 ml sterile Phosphate buffered saline solutions (PBS) solution. Next, 2 ml of Trypsin-

Ethylenediaminetetraacetic acid (EDTA) solution (gibco by life technologies) was added to dislodge the plated cells. Spread Trypsin-EDTA over the entire dish and incubate at 37°C for 2 minutes. Then 8ml of DMEM/F12 was added to suspend the cells. A portion of the suspension was transferred to a new dish for subculture. I seeded cells on glass bottom dishes and cultured them to 60–70% confluence prior to transfection. For the transfecion, I transfected 1.0 μg of plasmid DNA into HeLa cells following a polyethylenimine (PEI; 24765-1, Polysciences) transfection protocol [98]. Just before the florescence microscopy observation, I exchanged the culturing medium to DMEM/F12 (11039-021, ThermoFisher Scientific) without phenol red. In the case of two-photon FLIM experiment, the cell transfection was preformed following Lipofectamine 3000 (Invitrogen) protocol under 16 h incubation. To investigate whether the prolongation incubation time could improve the FRET performance under FLIM-FRET measurement. The FLIM observation was performed after 16 h transfection with additional 0h, 8 h and 24 h incubation in a 5% CO_2 incubator at 37°C, respectively.

Cell imaging. The Ti-2 (Nikon) epifluorescence microscope with the Fusion (Andor) control program was used for cell imaging. Nikon's CFI Plan Fluor 60XS Oil objective lens was chosen due to its superior transmission of 350 nm excitation light (~30%). Using an EM CCD camera (iXon Ultra; Andor), fluorescence images were obtained. A dichroic mirror (FF365-Di01-2536; Semrock), an excitation filter (F01-334/40-25; Semrock), and an emission filter (FF01-417/60-25; Semrock) were utilized for Sumire observations. As the excitation light, LedHUB (Omicron) LED line was used. For FRET imaging employing a pair of Sumire and Y-Velour-C22R, the same excitation light source, dichroic mirror, and excitation filter were used as in the previous Sumire observation. Immediately prior to observation, the cell culture medium was changed with observation medium (DMEM/F12; Gibco).

Quantification of the $FRET_{FLIM}$ efficiency and mature efficiency under two-photon FLIM. Two-photon FLIM-FRET was performed in HeLa cells at 730 nm excitation using Ti-sapphire laser (Mai Tai; Spectra-Physics) for Sumire, FF01-417/60-25 (Semrock) bandpass emission filter for Sumire fluorescence. The fluorescence lifetime image was generated by color-coding the mean lifetime values (τ_m) of each pixel. Time-correlated

single photon counting (TCSPC, SPC-150; Becker & Hickl) was used to obtain the fluorescence decay curve. The lifetime of fluorescence is the duration between fluorophore excitation and photon emission and is commonly measured in nanoseconds. The fluorescence of a free FP (Sumire) decays exponentially after a short pulse ($F(t)=F_0 \exp(-t/\tau_{FP})$, τ_{FP} is the fluorescence lifetime of FP). The fluorescence decay is double exponential when two types of fusion proteins (Donor with immature acceptor and donor with mature acceptor) are present together in the same cells ($F(t)= F_0 [P_D \exp(-t/\tau_D) + P_{DFRET} \exp(-t/\tau_{DFRET})]$. P_D is the proportions of donor FP fused with immature acceptor, P_{DFRET} is the proportion of donor fused with mature acceptor, τ_D is the fluorescence lifetime of donor fused with immature acceptor, τ_{DFRET} is the fluorescence lifetime of donor fused with mature acceptor. When FRET occurs, the fluorescence decay of the donor is accelerated because its excited state is now reduced by photon emission and FRET. The τ_D and τ_{DFRET} is related to the equation of mean FRET efficiency calculation ($FRET_{FLIM} = 1 - \tau_{DFRET}/\tau_D$). The P_D and P_{DFRET} are used for the maturation efficiency calculation (Maturation efficiency = P_D / (P_D + P_{DFRET})) [5,93,99,100].

4.3 Results and discussion

4.3.1 Development of a novel CP with shorter wavelength absorption

To fill in the color palette of CPs which can be used as the VFP Sumire's FRET acceptor. I developed Y-Velour from R-Velour variants. Altering the chromophore's covalent structure by replacing Tyr66 with another aromatic amino acid has shown to be an effective strategy for producing blue-shifted variants of the *Aequorea victoria* GFP (avGFP) [83,101]. The generation of an indole or imidazole-containing chromophore in avGFP that exhibited a blue light (400-450 nm) absorption spectrum takes place when tyrosine is replaced with tryptophan [91] or histamine. Following this strategy, I substitute the first two amino acids Gly60-Tyr61 of chromophore tripeptide with random mutations simultaneously into ofCP2.2, which is the origin of M-Velour-554, to generate the yellow variant of CP with blue shifted absorption. After the screening for bacterial colonies with the desired yellow color, I selected one colony for screening and photophysical analysis. As a result, ofCP2.2-Q60G/Y61W which has an absorption peak at 427 nm and molar extinction coefficient 43,000 $M^{-1}cm^{-1}$ was obtained. I designated it as Y-Velour abbreviated from "Yellow GFP-like chromoprotein with very low quantum yield and visible color with maximum absorption". The unmeasurable level of quantum yield of CP was preserved in Y-Velour (**Table 10 and Figure 24**).

(A) (B)

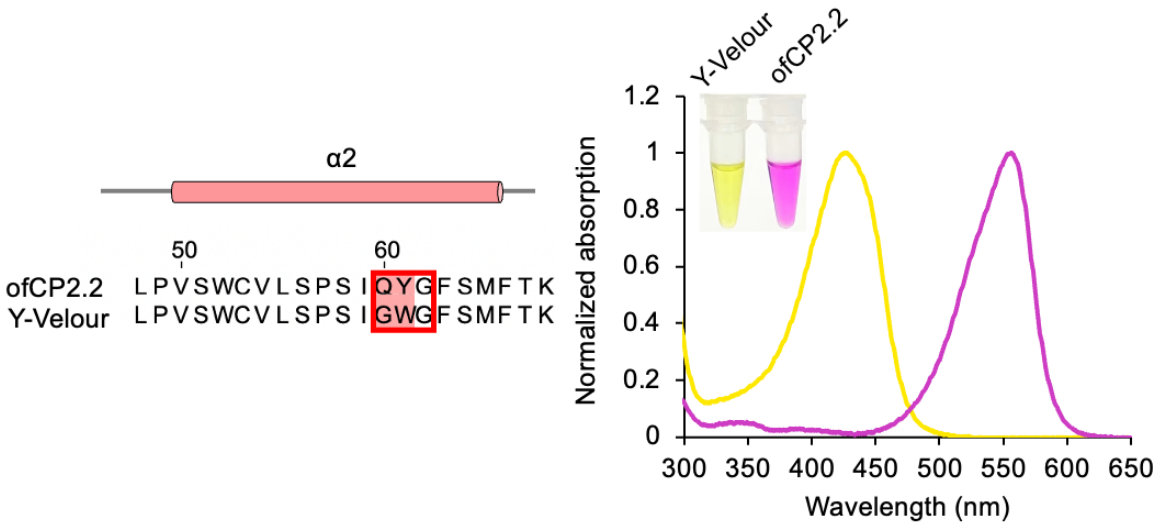

Figure 24. Evolution of new color variants of Y-Velour from ofCP2.2. (A) Amino acids sequence alignment (48th-68th). The chromophore of the tripeptide located in the α2-helix motif of R-Velour derived mutants is indicated by the bold red box. The mutations of Q60G and Y61W are highlighted in red. **(B)** Normalized absorption spectra of purified of Y-Velour and ofCP2.2, which were measured at 10 μM, pH7.5 at 25°C. The purified proteins of Y-Velour and ofCP2.2 exhibited yellow and magenta color.

Table 10. Physical properties of Y-Velour, ofCP2.2, and mTurquoise2

FPs	$\lambda_{max, abs}$[a]	λ_{em}[b]	ε ($mM^{-1} cm^{-1}$)[c]	Φ[d]
ofCP2.2	554	-	61,000	-
Y-Velour	427	-	43,000	-
mTurquoise2	434	474	30,000	0.93

[a]Maximum absorption wavelength.

[b]Maximum emission wavelength.

[c]Molar extinction coefficient determined by alkali-denaturation method.

[d]Absolute fluorescence quantum yield determined by integrating sphere.

4.3.2 FRET measurement

I then intended to use Y-Velour as an acceptor for FRET measurements, and Sumire was selected as the FRET donor. To determine whether Y-Velour is a good FRER acceptor, I compared it to other FRET acceptor candidates of mTagBFP2 and mT-Sapphire, whose absorption wavelengths (mTagBFP2 $\lambda_{max,\ abs}$ = 399 nm, mT-Sapphire $\lambda_{max,\ abs}$ = 399 nm) are likewise close to Sumire's fluorescence emission. I purified a tandem FRET construct consisting of Sumire and Y-Velour for *in vitro* FRET measurement. It has been reported that Lys238 in the C-terminal flexible region of mYPet (a YFP mutant) has been shown to be sensitive to trypsin digestion [102,103], and this cleavage could separate the FRET pair, which can be used for the calculation of FRET efficiency by investigating changes in fluorescence intensity of the donor and acceptor. In the case of Sumire, Lys239 was appeared at the corresponding position, thus, I fused Sumire in the N-terminal of all FRET constructs (**Figure 25**).

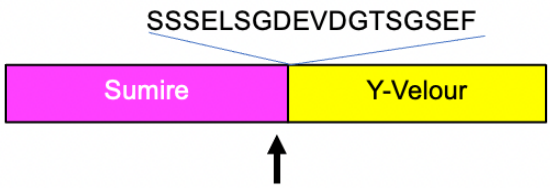

Figure 25. A diagram of the tandem FRET construct. 18 amino acids linker was inserted between donor and acceptor. Arrows indicate the putative trypsin sensitive sites.

The emission spectra of FRET constructs before and after trypsin cleavage are depicted in **Figure 26**. Apparently, the fluorescence emission spectra revealed that, for FRET construct of Sumire–Y-Velour, fluorescence can be detected in the narrow range from Sumire's fluorescence emission since Y-Velour did not have any fluorescence (**Figure 26B**). In the case of Sumire-mT-Sapphire and Sumire-mTagBFP2, the fluorescence spectra in the convolution of the emission from donor and acceptor occupied a wider range from 370 nm to 570 nm and 370 to 500 nm, respectively (**Figure 26C**). To evaluate the influence of trypsin digestion on the fluorophore of Sumire, firstly I digest the purified Sumire with trypsin independently and

confirmed there was no affection (**Figure 26A**). To investigate the performance of the Y-Velour as the quencher for Sumire, I compared the extent of dequenching of donor with that of other potential FP acceptors. The fluorescence intensity of FP donor emission peak was measured in the presence and absence of acceptor as F_{da} and F_d. After proteolysis by trypsin in Sumire-Y-Velour, the donor fluorescence intensity was dequenched from F_{da} to F_d, the increase was 32% of F_d, while the corresponding values of Sumire-mT-Sapphire and Sumire-mTagBFP2 were lower by 29% and 22%, respectively (**Figure 26D**). As a short conclusion, Y-Velour showed the good performance as the FRET quencher compared with the FPs of mTagBFP2 and mT-Sapphire. In addition, in comparison to Sumire-mT-Sapphire, the observation of Sumire-Y-Velour requires only a limited spectrum of wavelengths. In an attempt to improve the FRET efficiency, the Sumire-Y-Velour fusion library was created applying error-prone PCR together with StEP as random mutagenesis on Y-Velour fragment. Through with a process of mutagenesis and screening, one Sumire-Y-Velour FRET pair mutant (Y-Velour-C22R) with dimmed fluorescence emission under violet excitation and bright yellow color observed under ambient light from the whole library were selected for evolution. The donor emission in FRET pair of Sumire-Y-Velour-C22R was dequenched by 42% nearly 1.3-fold greater than that of Sumire-Y-Velour under the *in vitro* FRET measurement (**Figure 27**).

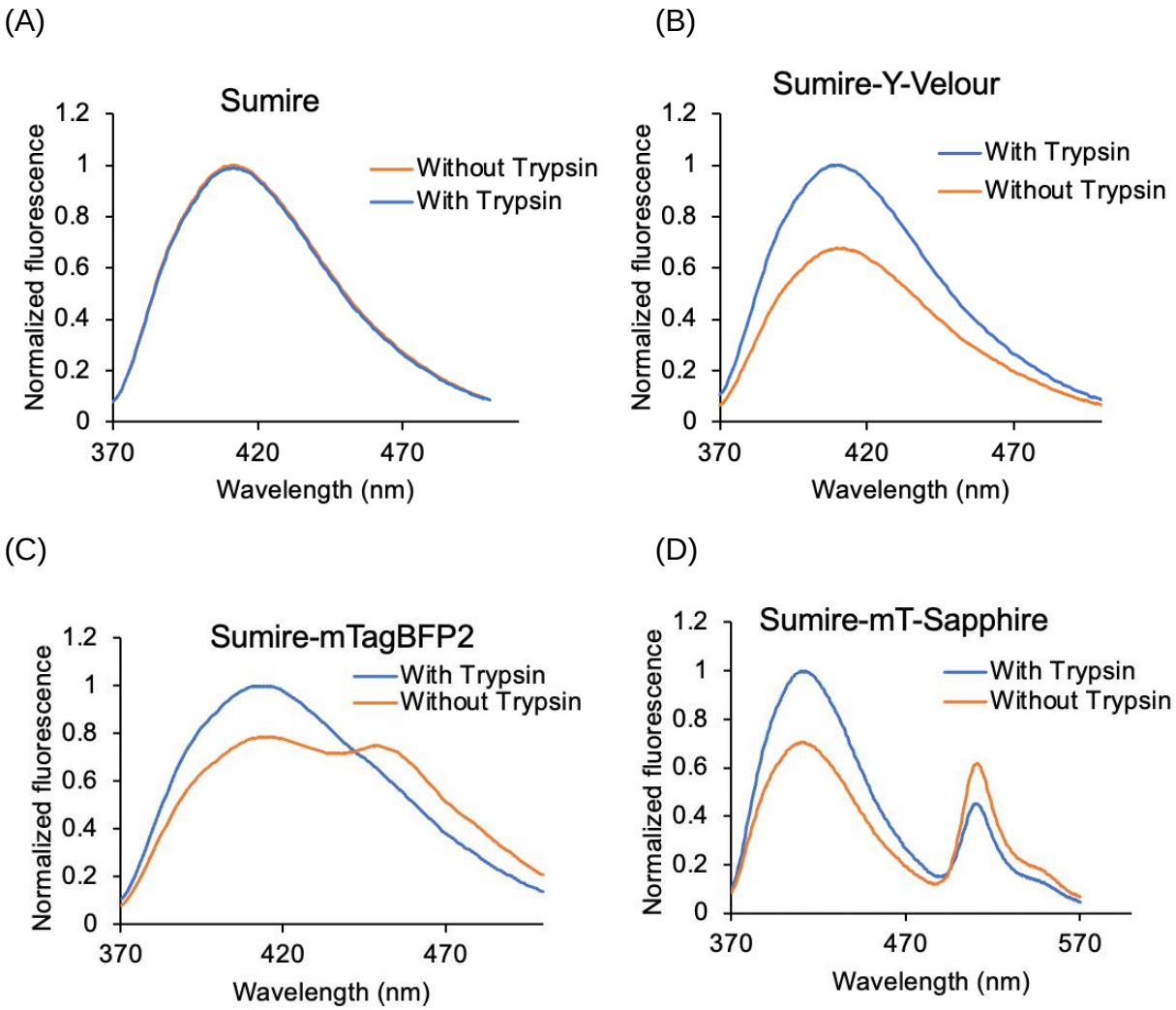

Figure 26. Emission spectra of the FRET constructs. (A, B, C, D) Samples before (orange) and after (blue) trypsin cleavage were excited at 340 nm and the relative emission intensities were measured at wavelengths from 370 to 500 nm in (A, B, C), and from 370 nm to 570 nm in (D)

(A)

Donor	Acceptor	Dequenching
Sumire	mT-Sapphire	29%
Sumire	mTagBFP2	22%
Sumire	Y-Velour	32%
Sumire	Y-Velour-C22R	42%

(B)

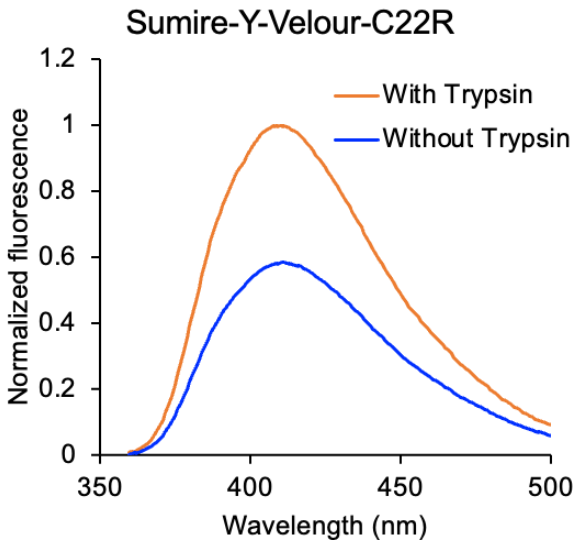

Figure 27. Evolution of FRET pair. (A) The extent of dequenching of the donor when the acceptor is removed among all FRET constructs in this study. **(B)** Samples before (orange) and after (blue) trypsin cleavage were excited at 340 nm and the relative emission intensities were measured at wavelengths from 370 to 500 nm.

Next, I compared the performance of Y-Velour-C22R as a FRET acceptor for Sumire with different acceptors in mammalian cells. Single Sumire and tandem FRET constructs were expressed in living HeLa cells, and the fluorescence lifetime of Sumire was determined using the two-photon FLIM (**Figure 28A**). Initially, FLIM measurement was performed immediately after 15 hours transfection. As a result, single Sumire showed the fluorescence lifetime of 2.56 ns, and the cells expressing FRET constructs showed a shorter fluorescence lifetime confirming the occurrence of FRET. Apparently, FRET pair of Sumire-Y-Velour-C22R showed the lowest average fluorescence lifetime of 2.07 ns which is lower than that of Sumire-mT-Sapphire (2.43 ns), Sumire-mTagBFP2 (2.28 ns) and Sumire-Y-Velour (2.10 ns), respectively (**Figure 28B**). However, compared to mT-Sapphie and mTagBFP2, both Y-Velour and Y-Velour-C22R displayed a relatively large cell-to-cell difference, which may be attributed to the immaturity of FRET acceptor as a result of the short incubation time after transfection. To further improve it, the incubation time of expressed FRET pairs in cell was prolonged (16 hours transfection with additional 8 hours and 24 hours incubation respectively) which was expected to remedy the relatively high heterogeneous maturation efficiency of cells expressing Sumire-Y-Velour and Sumire-Y-Velour-C22R.

Consequently, as cells were incubated for longer time, a decreasing trend in the cell-to-cell variability of FRET constructs was found under FLIM measurement (**Figure 29**). Protocol of 16 hours transfection with additional 24 hours incubation exhibited the highest FRET and smallest cell-to-cell difference (**Figure 29B**). Under this protocol, FRET pair of Sumire-Y-Velour-C22R showed the lowest average fluorescence lifetime of 1.90 ns, which is lower than that of Sumire-mT-Sapphire (2.28 ns) and Sumire-Y-Velour (1.93 ns), and exhibited reduced cell-to-cell variability with the best performance. In addition, because the fluorescence lifetime decay curves are convolution of both the acceptor maturation and $FRET_{FLIM}$ efficiency, we examined both parameters independently in order to obtain more specific data (Calculation details in **section 4.2**). Consequently, despite the fact that the FRET efficiencies between donor and mature acceptor of Sumire-Y-Velour ($FRET_{FLIM}$ efficiency = 55%) were lower than those of Sumire-mT-Sapphire ($FRET_{FLIM}$ efficiency = 60%), the maturity of Y-Velour was discovered to be significantly superior to the Sumire-mT-Sapphire. In the instance of Y-Velour-C22R, the $FRET_{FLIM}$ efficiency was equivalent to that of Y-Velour, but the maturation efficiency was somewhat enhanced. (**Figure 30**). Taken together, my research suggested that the Y-Velour-C22R is a suitable FRET acceptor for Sumire in FLIM.

(A)

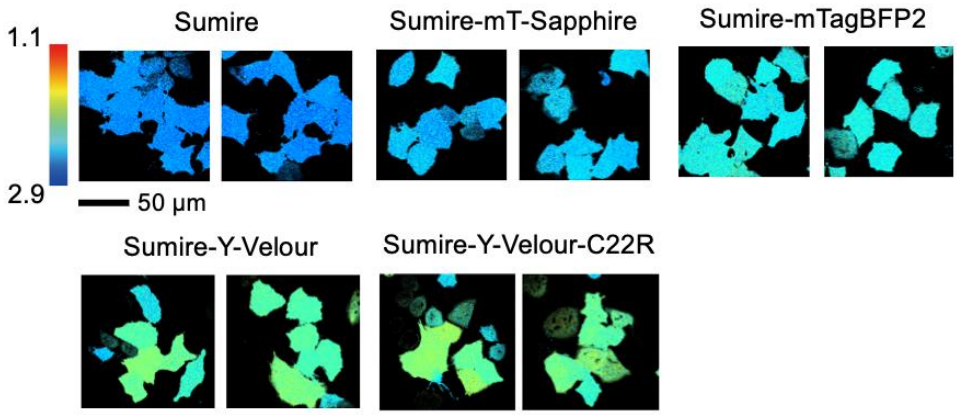

(B)

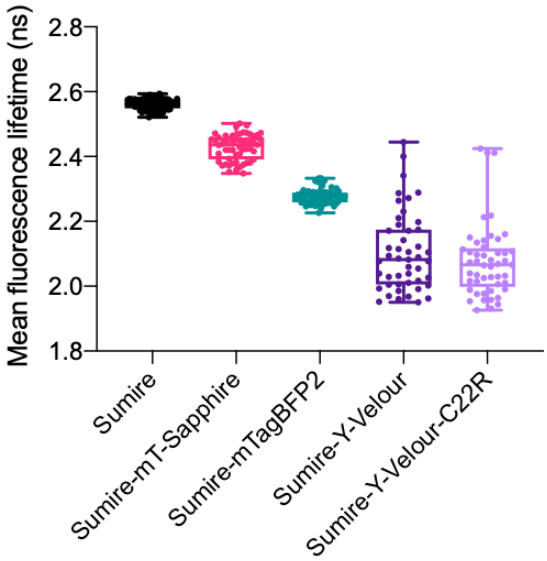

Figure 28. FLIM-FRET results of various FRET constructs with Sumire donor in HeLa cells. (A) The fluorescence lifetime image was generated by color-coding the mean lifetime values of each pixel. The color bar in the pseudo-color image represent the fluorescence lifetime value (1.1 - 2 .9 ns). **(B)** Box-plot of the mean fluorescence lifetime value of FLIM above for single Sumire FP (n = 72 cells) and different FRET pairs (Sumire-mT-Sapphire, n = 55 cells; Sumire-mTagBFP2, n = 65 cells; Sumire-Y-Velour, n = 47 cells; Sumire-Y-Velour-C22R, n = 49 cells). The centre line of a box plot represents the median, while the lower and upper hinges reflect the first and third quartiles. Whiskers run across the entire area of the data.

(A)

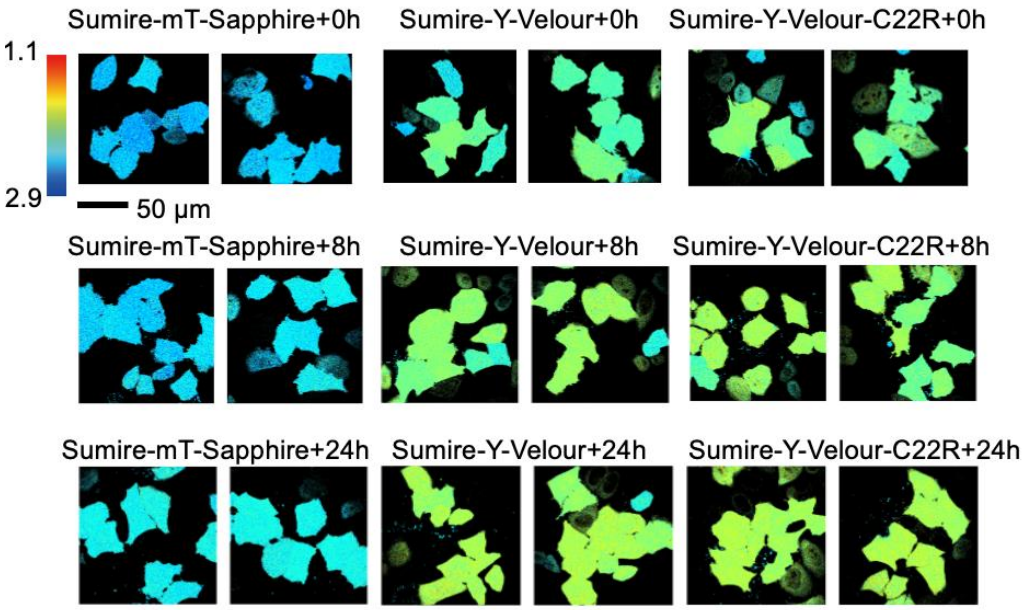

(B)

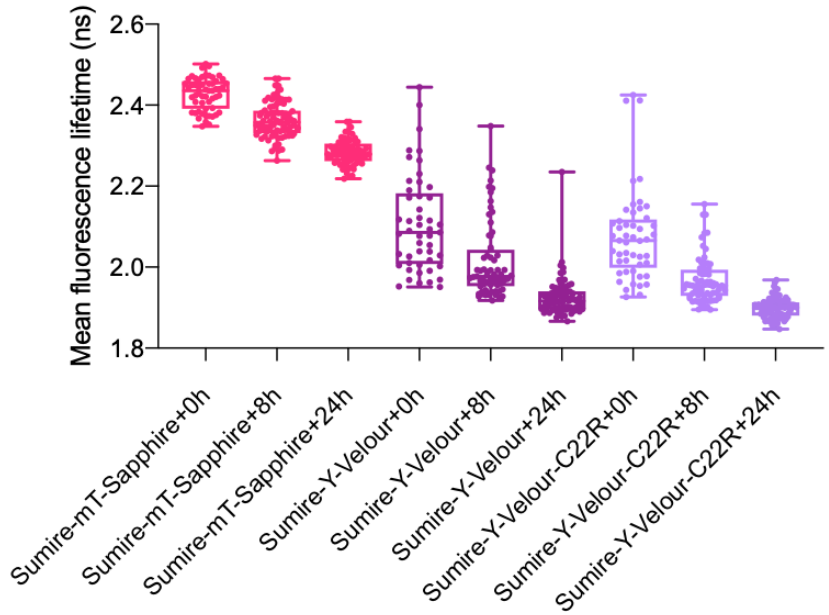

Figure 29. Investigation between the cell-to-cell difference with extending incubation time under the FLIM-FRET measuremnt in HeLa cells. (A) The fluorescence lifetime image was generated by color-coding the mean lifetime values of each pixel. The color bar in the pseudo-color image represent the fluorescence

lifetime value (1.1 - 2 .9 ns). From top to bottom, first transfect for 16 hours, then incubate for 0, 8, and 24 hours respectively, and then observe with FLIM. **(B)** Box-plot of the mean fluorescence lifetime value of FLIM above for different FRET pairs (Sumire-mT-Sapphire+0h, n = 55 cells; Sumire- mT-Sapphire+8h, n = 84 cells; Sumire-mT-Sapphire+24h, n = 69 cells; Sumire-Y-Velour+0h, n = 47 cells; Sumire-Y-Velour+8h, n = 67 cells; Sumire-Y-Velour+24h, n = 75 cells; Sumire-Y-Velour-C22R+0h, n = 49 cells; Sumire-Y-Velour-C22R+8h, n = 71 cells; Sumire-Y-Velour+24h, n = 83 cells). The centre line of a box plot represents the median, while the lower and upper hinges reflect the first and third quartiles. Whiskers run across the entire area of the data.

(A) (B)

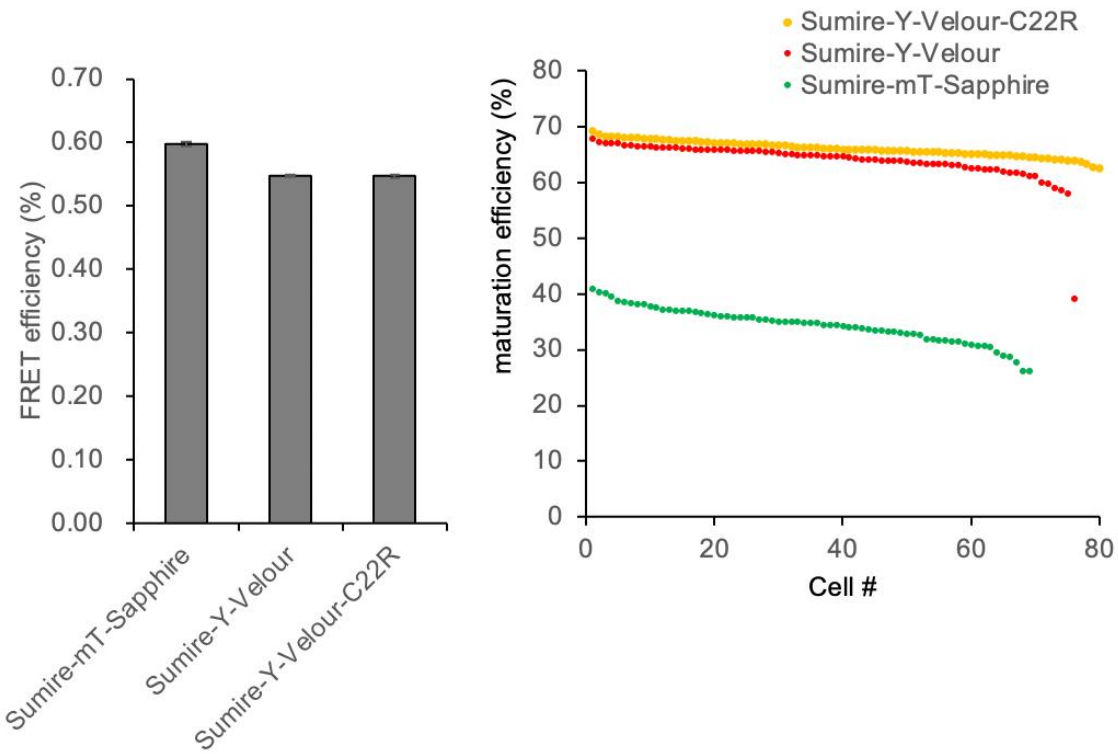

Figure 30. $FRET_{FLIM}$ efficiency and maturity of FRET acceptor in FRET pairs with donor of Sumire. (A) $FRET_{FLIM}$ efficiency between donor with mature acceptor among all FRET constructs in this study. Eight images were used in the analysis. The mean ± standard deviation (SD) are indicated in the figure **(B)** A comparison of the maturation

efficiency of an acceptor as measured in individual cells, with the results shown in descending order.

4.3.3 Performance of FRET pair of Sumire-Y-Velour-C22R in Ca^{2+} FRET indicator in live HeLa cells

To evaluate the Y-Velour-C22R's performance as FRET acceptor in single-molecule types of FRET indicator that was consists of a conformation changeable sensor domain with the FP donor and CP acceptor, I replace the CFP and YFP moieties of a FRET-based Ca^{2+} indicator, Twitch-2B [22,104], with Sumire and Y-Velour, respectively (**Figure 31A**), and developed a Ca^{2+} indicator (vyCa^{2+}). Ca^{2+} titration of purified vyCa^{2+} revealed that the K_d for Ca^{2+} is 298 nM with a Hill constant of 1.64 which is closed that of the Twitch-2B (K_d for Ca^{2+} was 250 nM with a Hill constant of 1.7) (**Figure 31B**). The dynamic range of vyCa^{2+} is 47% ($\Delta F/F$). Next, I demonstrated cytosolic Ca^{2+} imaging in HeLa cells expressing vyCa^{2+}. 3 μM Thapsigargin caused a continuous decrease of fluorescence intensity (Maximum $\Delta F/F$, 46%) (**Figure 32**) In addition, as an alternative approach to affect Ca^{2+} concentration in the cytosolim, histamine was added. Histamine-induced Ca^{2+} oscillations were successfully reported by vyCa^{2+}. After histamine stimulation, an acute Ca^{2+} spike followed by Ca^{2+} oscillations in fluorescent intensity change were observed (Maximum $\Delta F/F$, 79%) (**Figure 33**).

(A) (B)

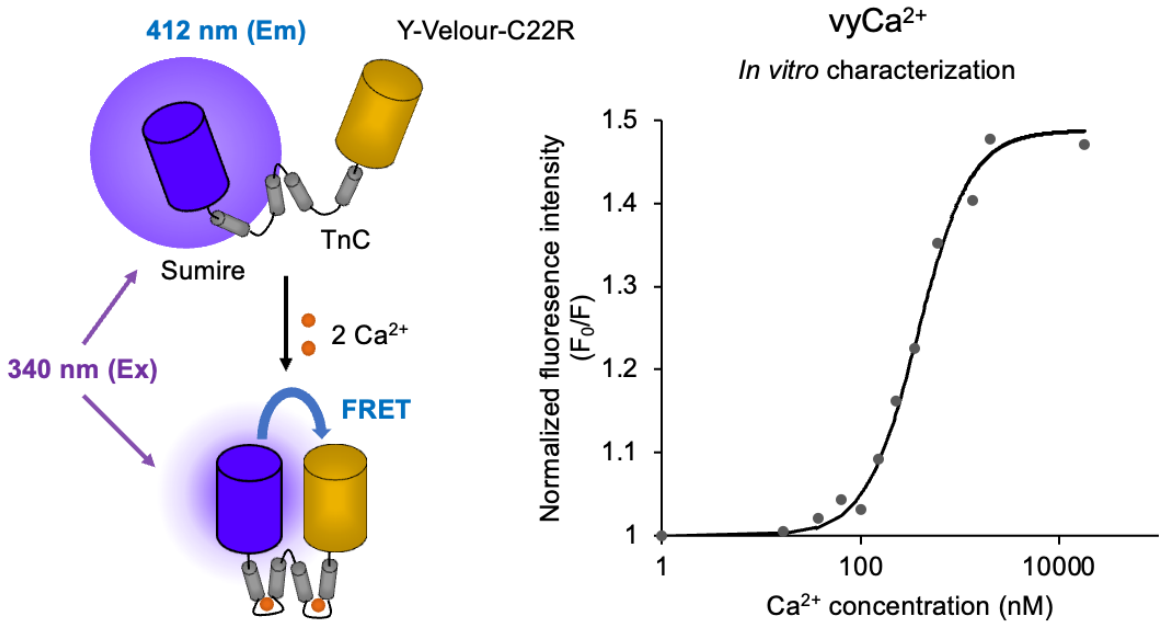

Figure 31. Schematic representation of the Ca^{2+} sensing mechanism of vyCa^{2+}. **(A)** TnC, Ca^{2+}-binding moiety of Twitch-2B derived from from the C-terminal globular domain of toadfish Troponin C (TnC). Sumire with C-terminal 11 amino acids deleted. **(B)** Ca^{2+} titration curve for the indicator.

(A) (B)

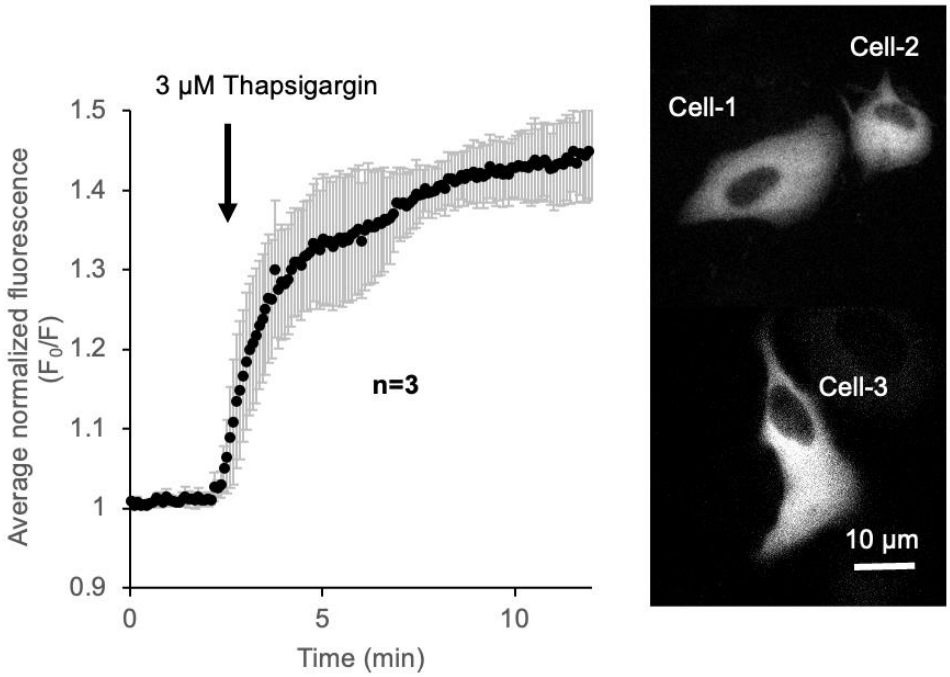

Figure 32. Ca^{2+} imaging with vyCa^{2+} in HeLa cells. (**A**) Time course of the normalized fluorescence intensity with 3 μM Thapsigargin stimulation to inhibit ER Ca^{2+} influx. **(B)** Fluorescence images of measured HeLa cells expressing vyCa^{2+} before adding 3 μM Thapsigargin.

(A) (B)

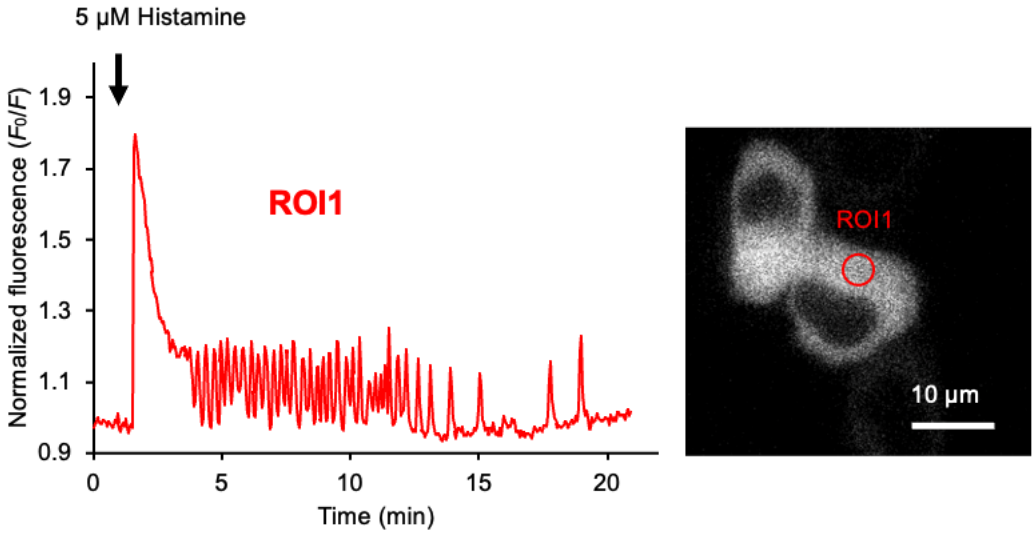

Figure 33. Ca^{2+} imaging with vyCa^{2+} in HeLa cells. **(A)** Time course of the normalized fluorescence intensity with 5 μM Histamine stimulation for Ca^{2+} oscillation (Red, ROI1). **(B)** Fluorescence images of HeLa cells expressing vyCa^{2+} (Red, ROI1).

4.4 Conclusion

GFP-like CPs with non-fluorescence and high light absorption ability have been used for FRET based indicators for bioimaging. In this study, I constructed a new yellow CP, Y-Velour, with the more shorter absorption maximum (427 nm) compared with other reported CPs. Y-Velour has the tryptophan-based chromophore and has the extinction coefficient at 43,000 M^{-1} cm^{-1}. The extinction coefficient value of Y-Velour is comparable to that of other FPs containing tryptophan-based chromophore (mTurquoise2 showed the extinction coefficient value at 30,000 M^{-1} cm^{-1}) (**Table 10**). Y-Velour can be paired with the donor of VFP (Sumire) as a FRET receptor. Under the comparison with other FPs (mTagBFP2 and mT-Sapphire) that act as FRET acceptor, Sumire-Y-Velour exhibited the best performance in the aspect of quenching donor fluorescence. For further improve the FRET efficiency between Sumire with Y-Velour, I performed random mutagenesis and selected the best FRET pair (Sumire-Y-Velour-C22R). Under two-photon FLIM, all FRET constructs were examined. Y-Velour-C22R demonstrated superior FRET performance in comparison to others. In addition, the $FRET_{FLIM}$ efficiency and maturation efficiency of all FRET construct was calculated under the fluorescence lifetime curve fitting (**Details see section 4.2**). In reality, free Sumire (Sumire fused with immature acceptor) and Sumire undergoing FRET (Sumire fused with mature acceptor) generally coexist in cells. The $FRET_{FLIM}$ efficiency value between Sumire and mature acceptor was calculated to be greater than that of $FRET_{\textit{in vitro}}$ between donor with immature/mature acceptors. In terms of maturation efficiency, both Y-Velour and Y-Velour-C22R displayed a high proportion of the maturation fraction, but with a greater cell-to-cell variation than the others. Prolonged incubation improves the performances of the FRET pairs likely due to the increased maturation of the acceptors. Moreover, to quantify the performance of Y-Velour-C22R, I applied this FRET pair in the FRET-based Ca^{2+} indicator. As a result, my FRET pair was also useful as a Ca^{2+} indicator (vyCa^{2+}) based on FRET technology in the live HeLa cells, which should also be applicable to future FLIM-FRET measurement. Moreover, due to FRET pairs based on Sumire-Y-Velour-C22R can be detected in narrow-spectrum bandpass, there is great potential for their application to multi-parameter imaging together with BFP-, GFP- or RFP based indicators in the near future. And by reducing the excitation intensity and employing broader optical filters for the FP donor of Sumire,

Y-Velour-C22R acceptor was expected to decrease the risk of phototoxicity in the future cell imaging.

CHAPTER 5
CONCLUSION AND PERSPECTIVES

5.1 Conclusion

In this research, I sucessfully analyzed the 3D-protein sturcture of non-fluorescent red CP, namely R-Velour, from the flower hat jellyfish (*Olindias formosa*) under X-ray crystallography. To analyze the photophysical properties from a structural aspect, I determined the crystal structure of R-Velour at a 2.1 Å resolution. R-Velour has a *trans*-chromophore similar to the GFP, Gamillus, derived from the same jellyfish. However, in contrast to the two coplanar chromophoric rings in Gamillus, R-Velour has a large torsion inducing non-fluorescence property. The side chains of Phe140 and Arg89 directly press the phenoxy (Tyr61) moiety of their chromophore out of the plane. Through structural analysis, I proposed that the non-fluorescence property of R-Velour with almost zero quantum yield might be attributed to the combination of the large torsion of the two chromophoric rings and higher motility of the phenoxy (Tyr61) moiety. Additionally, based on the site-directed mutagenesis study, I found that the 140th and 142nd residues are vital to fluorescence properties. Two key mutations of F140W/C142G could convert the ofCP2.2 (the prototype of M-Velour-554) into a FP.

To expanding the CP's diversity, I developed new color variants of O-Velour (λ_{max}= 392, 506 nm) and M-Velour-554 (λ_{max}= 554 nm) with orange and magenta colors through site-directed mutagenesis. Through the survey for residues surrounding the chromophore by mutagenesis, we found a key residue, S155, which is responsible for R-Velour color change. The substitution of Ser155 near the phenolic acid portion of the chromophore effectively affected the absorption peak shift. A single replacement of Ser155 with hydrophobic residues can optimize the absorption spectrum of R-Velour in the range of 528–553 nm. Based on the recently proposed spectrum shift theory, I explained the spectrum shift with the difference in the state of the hydrogen bonds from the chromophore phenolate oxygen. That was further supported by disruption of the hydrogen bond in the new crystal structure of the variants M-Velour-554 with the bathochromic shift. In addition to developing new CP variants from R-Velour, I

performed rationally-designed mutagenesis employing mTFP1 as a template to construct three yellow CPs (dimTFP-460, dimTFP-465, and dimTFP-470) to fill the current CP's optical window gap (440nm-480nm wavelength). The development of this three yellow CPs with blue-cyan light absorption can be potentially used as the BFP FRET acceptor for the future FRET measurement. These findings and information support the development of novel CP color variants for multi-color imaging to satisfy the demand of biosensors with wider color variation to visualize multiple physiological events by multimodal imaging using conventional optical imaging, FLIM, and PAI.

Finally, a new yellow CP, Y-Velour, with the more shorter absorption maximum (427 nm) was constructed. As a FRET acceptor, Y-Velour can be coupled with the donor of VFP (Sumire). Compared with other FRET acceptor FPs (mTagBFP2 and mT-Sapphire), Sumire-Y-Velour demonstrated the best performance in terms of donor fluorescence quenching. After the optimization, new FRET pair (Sumire-Y-Velour-C22R) with the highest FRET performance that measured under *in vitro* and in cells (two-photon FLIM) was developed, which can be applied as the FRET-based Ca^{2+} indicator in living HeLa cells. Due to the fact that FRET pairs based on FP-CP can be detected in a narrow-spectrum bandpass, their future application to multi-parameter active imaging holds tremendous promise.

As a conclusion, I reported 9 new CPs (Y-Velour, dimTFP-460, dimTFP-465, dimTFP-475, O-Velour, R-Velour, M-Velour-537, M-Velour-553 and M-Velour-554) which perfectly compensate the gap of the CPs optical absorption window ranging from 400 nm-480 nm, 500 nm-560 nm. Color tuning mechanism was analyzed under the structure aspect from R-Velour and M-Velour-554. This information supports the development of novel CP color variants for multi-color imaging to satisfy the demand of biosensors with wider color variation to visualize multiple physiological events by multimodal imaging using conventional optical imaging, FLIM, and PAI.

5.2 Perspectives

5.2.1 Y-Velour

In the case of the conventional FLIM-FRET, several different CPs have been designed as FRET acceptors for GFP and RFP in the optical window with larger wavelength, but no efforts have been made to design a CP acceptor for the FRET donor of VFP or BFP donor with shorter wavelength characteristic. In my study, I successfully obtained the two types of yellow CPs. The Y-Velour-C22R with the shorter wavelength absorption has been demonstrated to be the good FRET acceptor with VFP Sumire. In addition, another yellow CP, dimTFP-465, derived from mTFP1, exhibiting the blue-cyan light absorption, which can potentially be used as the FRET acceptor for the blue fluorescence protein, such as, EBFP2 or mTagBFP2. Due to the Sumire's unique photophysical feature with shortest emission wavelength, the dual color imaging between Sumire with BFPs which only utilize shorter wavelength channel could be attainable in the future. Thus, there is great potential for their application to multi-parameter active imaging together with other reported indicator based on GFP or RFP in the near future

5.2.2 R-Velour

R-Velour exhibits strong light absorption and is completely non-fluorescent and can therefore be a potential acceptor paired with the donor of GFP such as Gamillus. During the aforementioned mutagenesis study, I discovered a novel red mutant with a more brilliant red color. The photophysical property analysis revealed that the new R-Velour variant (R-Velour-Q60G) has the more higher molar extinction coefficient at 127,000 M^{-1} cm^{-1}, absorption maximum at 520 nm and the same undetectable quantum yield ($\Phi < 0.001$). Compared with ShadowY (ε= 136,000 M^{-1} cm^{-1}, $\Phi = 0.01$) [18] which is an already reported famous CP, R-Velour-Q60G has the comparable molar extinction coefficient but lower quantum yield, which has great potential as a great reporter gene or FRET acceptor in the field of PAI or FLIM-FRET imaging, respectively. In addition, it's also useful to separately express R-Velour color variants in different types of cells (e.g. tumor and immune cells [105,106]) for monitoring cells migration or other complex activities of cells under multicolor photoacoustic imaging [42,107]. For the improvement of the PAI signal, one of the recent papers reported a new directed

evolution method for screening CPs mutant based their photoacoustic signal level and make it a possible to directly evolve CPs with enhanced photophysical properties [33]. In the future, these kinds of new methods will be considered for the screening of improved R-Velour variants to applicable for photoacoustic imaging.

5.2.3 M-Velour

M-Velour-554 has been considered as the good FRET acceptor for the orange fluorescence protein, such as mKO_K, mOrange2 and CyOFP1 because the emission spectra of these proteins significantly overlap with the absorption spectrum of M-Velour-554. Although various CPs have already been developed as FRET acceptor for GFP and RFP, the CP acceptor developed for the orange fluorescent protein (OFP) donor has not been attempted. To investigate the M-Velour-554's performance as the OFP CP acceptor, two-photon FLIM-FRET was performed in HeLa cells (1000 nm excitation (Ti-sapphire laser) for all OFPs, FF01-625/90 (Semrock) bandpass emission filter for OFP fluorescence (**Figure 34**). Results were supported from Hideji Murakoshi, Associate Professor from National Institute for Physiological Sciences, and student Hiromo Ueda, from Department of Physiological Sciences, SOKENDAI (The Graduate University for Advanced Studies). As a result, mKOκ-M-Velour-554 exhibted the best $FRET_{FLIM}$ efficiency (66%) with small cell-to-cell difference. Based on this data, it should be possible to create a novel OFP-CP FRET pair as a practical genetically encoded FRET indicator in the near future.

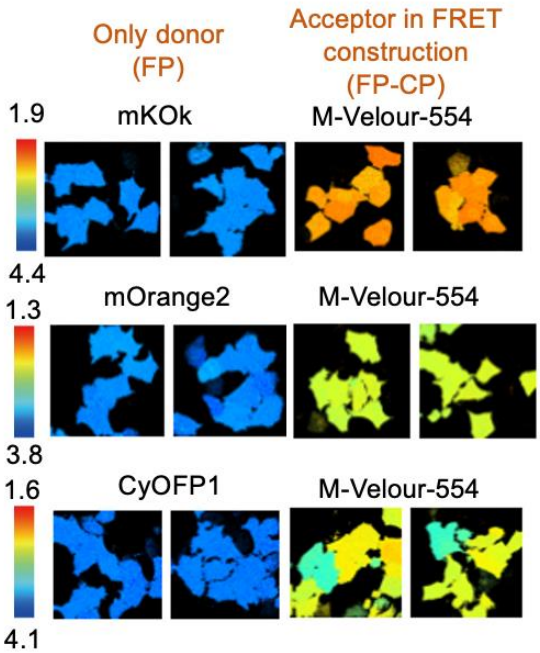

Figure 34. FLIM-FRET results of various OFP-CP construction in HeLa cells. The different OFPs were fushed with M-Velour-554 via the amino acid linker of Gly-Thr. The fluorescence lifetime image was generated by color-coding the mean lifetime values (τ_m) of each pixel. The color bar in the pseudo-color image represent the fluorescence lifetime value. Time-correlated single photon counting (TCSPC) was used to obtain the fluorescence decay curve. The fluorescence liftetime of all FRET pairs showed a decreased fluorescence lifetime, indicating FRET from donor of mKOκ, mOrange2 and CyOFP1 to M-Velour-554 resepectively. The formula ($1 - \tau_{FRET}/\tau_{OFP}$) was used to determine the average $FRET_{FLIM}$ efficiency, where τ_{FRET} means the fluorescence lifetime of OFP fused with mature CP acceptor, and τ_{OFP} is the fluorescence lifetime of OFP. Details of the two-photon FLIM-FRET imaging and data analysis are reported in the past [93,100].

REFERENCES

[1] E.A. Rodriguez, R.E. Campbell, J.Y. Lin, M.Z. Lin, A. Miyawaki, A.E. Palmer, X. Shu, J. Zhang, R.Y. Tsien, The Growing and Glowing Toolbox of Fluorescent and Photoactive Proteins, Trends in Biochemical Sciences. 42 (2017) 111–129. https://doi.org/10.1016/j.tibs.2016.09.010.

[2] T. Matsuda, K. Horikawa, K. Saito, T. Nagai, Highlighted Ca 2+ imaging with a genetically encoded “caged” indicator, Scientific Reports. 3 (2013) 2–5. https://doi.org/10.1038/srep01398.

[3] S. Ganesan, S.M. Ameer-Beg, T.T.C. Ng, B. Vojnovic, F.S. Wouters, A dark yellow fluorescent protein (YFP)-based Resonance Energy-Accepting Chromoprotein (REACh) for Förster resonance energy transfer with GFP, Proceedings of the National Academy of Sciences of the United States of America. 103 (2006) 4089–4094. https://doi.org/10.1073/pnas.0509922103.

[4] T. Laviv, B.B. Kim, J. Chu, A.J. Lam, M.Z. Lin, R. Yasuda, Simultaneous dual-color fluorescence lifetime imaging with novel red-shifted fluorescent proteins, Nature Methods. 13 (2016) 989–992. https://doi.org/10.1038/nmeth.4046.

[5] R. Yasuda, C.D. Harvey, H. Zhong, A. Sobczyk, L. Van Aelst, K. Svoboda, Supersensitive Ras activation in dendrites and spines revealed by two-photon fluorescence lifetime imaging, Nature Neuroscience. 9 (2006) 283–291. https://doi.org/10.1038/nn1635.

[6] K.A. Lukyanov, A.F. Fradkov, N.G. Gurskaya, M. V. Matz, Y.A. Labas, A.P. Savitsky, M.L. Markelov, A.G. Zaraisky, X. Zhao, Y. Fang, W. Tan, S.A. Lukyanov, Natural animal coloration can be determined by a nonfluorescent green fluorescent protein homolog, Journal of Biological Chemistry. 275 (2000) 25879–25882. https://doi.org/10.1074/jbc.C000338200.

[7] S.G. Dove, M. Takabayashi, O. Hoegh-Guldberg, Isolation and Partial Characterization of the Pink and Blue Pigments of Pocilloporid and Acroporid Corals, The Biological Bulletin. 189 (1995) 288–297. https://doi.org/10.2307/1542146.

[8] N.G.G. Y, A.F.F. Y, A. Terskikh, M.V.M. Y, Y.A. Labas, V.I. Martynov, Y.G. Yanushevich, K.A. Lukyanov, S.A.L. Y, GFP-like chromoproteins as a source of far-red £ uorescent proteins 1, 507 (2001) 16–20.

[9] M.A. Shkrob, Y.G. Yanushevich, D.M. Chudakov, N.G. Gurskaya, Y.A. Labas, S.Y. Poponov, N.N. Mudrik, S. Lukyanov, K.A. Lukyanov, Far-red fluorescent proteins evolved from a blue chromoprotein from Actinia equina, Biochemical Journal. 392 (2005) 649–654. https://doi.org/10.1042/BJ20051314.

[10] M.C.Y. Chan, S. Karasawa, H. Mizuno, I. Bosanac, D. Ho, G.G. Privé, A. Miyawaki, M. Ikura, Structural characterization of a blue chromoprotein and its yellow mutant from the sea anemone Cnidopus japonicus, Journal of Biological Chemistry. 281 (2006) 37813–37819. https://doi.org/10.1074/jbc.M606921200.

[11] A. Pettikiriarachchi, L. Gong, M.A. Perugini, R.J. Devenish, M. Prescott, Ultramarine, a chromoprotein acceptor for förster resonance energy transfer, PLoS ONE. 7 (2012). https://doi.org/10.1371/journal.pone.0041028.

[12] M. Prescott, M. Ling, T. Beddoe, A.J. Oakley, S. Dove, O. Hoegh-Guldberg, R.J. Devenish, J. Rossjohn, The 2.2 Å crystal structure of a pocilloporin pigment reveals a nonplanar chromophore conformation, Structure. 11 (2003) 275–284. https://doi.org/10.1016/S0969-2126(03)00028-5.

[13] C.Y. Chiang, C.C. Lee, S.Y. Lo, A.H.J. Wang, H.J. Tsai, Chromophore deprotonation state alters the optical properties of blue chromoprotein, PLoS ONE. 10 (2015) 1–15. https://doi.org/10.1371/journal.pone.0134108.

[14] H.Y. Chang, T.P. Ko, Y.C. Chang, K.F. Huang, C.Y. Lin, H.Y. Chou, C.Y. Chiang, H.J. Tsai, Crystal structure of the blue fluorescent protein with a Leu-Leu-Gly tri-peptide

chromophore derived from the purple chromoprotein of Stichodactyla haddoni, International Journal of Biological Macromolecules. 130 (2019) 675–684. https://doi.org/10.1016/j.ijbiomac.2019.02.138.

[15] P.G. Wilmann, J. Petersen, A. Pettikiriarachchi, A.M. Buckle, S.C. Smith, S. Olsen, M.A. Perugini, R.J. Devenish, M. Prescott, J. Rossjohn, The 2.1 Å crystal structure of the far-red fluorescent protein HcRed: Inherent conformational flexibility of the chromophore, Journal of Molecular Biology. 349 (2005) 223–237. https://doi.org/10.1016/j.jmb.2005.03.020.

[16] Y. Nakahata, J. Nabekura, H. Murakoshi, Dual observation of the ATP-evoked small GTPase activation and Ca2+ transient in astrocytes using a dark red fluorescent protein, Scientific Reports. 6 (2016) 1–10. https://doi.org/10.1038/srep39564.

[17] H. Murakoshi, A.C.E. Shibata, Y. Nakahata, J. Nabekura, A dark green fluorescent protein as an acceptor for measurement of Förster resonance energy transfer, Scientific Reports. 5 (2015) 1–12. https://doi.org/10.1038/srep15334.

[18] H. Murakoshi, A.C.E. Shibata, ShadowY: A dark yellow fluorescent protein for FLIM-based FRET measurement, Scientific Reports. 7 (2017) 1–10. https://doi.org/10.1038/s41598-017-07002-4.

[19] H. Murakoshi, H. Horiuchi, T. Kosugi, M. Onda, A. Sato, N. Koga, J. Nabekura, ShadowR: a novel chromoprotein with reduced non-specific binding and improved expression in living cells, Scientific Reports. 9 (2019) 1–11. https://doi.org/10.1038/s41598-019-48604-4.

[20] K. Terai, A. Imanishi, C. Li, M. Matsuda, Two decades of genetically encoded biosensors based on förster resonance energy transfer, Cell Structure and Function. 44 (2019) 153–169. https://doi.org/10.1247/csf.18035.

[21] K. Horikawa, Y. Yamada, T. Matsuda, K. Kobayashi, M. Hashimoto, T. Matsu-Ura, A. Miyawaki, T. Michikawa, K. Mikoshiba, T. Nagai, Spontaneous network activity

visualized by ultrasensitive Ca^{2+} indicators, yellow Cameleon-Nano, Nature Methods. 7 (2010) 729–732. https://doi.org/10.1038/nmeth.1488.

[22] T. Thestrup, J. Litzlbauer, I. Bartholomäus, M. Mues, L. Russo, H. Dana, Y. Kovalchuk, Y. Liang, G. Kalamakis, Y. Laukat, S. Becker, G. Witte, A. Geiger, T. Allen, L.C. Rome, T.W. Chen, D.S. Kim, O. Garaschuk, C. Griesinger, O. Griesbeck, Optimized ratiometric calcium sensors for functional in vivo imaging of neurons and T lymphocytes, Nature Methods. 11 (2014) 175–182. https://doi.org/10.1038/nmeth.2773.

[23] K. Maeshima, T. Matsuda, Y. Shindo, H. Imamura, S. Tamura, R. Imai, S. Kawakami, R. Nagashima, T. Soga, H. Noji, K. Oka, T. Nagai, A Transient Rise in Free Mg^{2+} Ions Released from ATP-Mg Hydrolysis Contributes to Mitotic Chromosome Condensation, Current Biology. 28 (2018) 444-451.e6. https://doi.org/10.1016/j.cub.2017.12.035.

[24] H. Bischof, M. Rehberg, S. Stryeck, K. Artinger, E. Eroglu, M. Waldeck-Weiermair, B. Gottschalk, R. Rost, A.T. Deak, T. Niedrist, N. Vujic, H. Lindermuth, R. Prassl, B. Pelzmann, K. Groschner, D. Kratky, K. Eller, A.R. Rosenkranz, T. Madl, N. Plesnila, W.F. Graier, R. Malli, Novel genetically encoded fluorescent probes enable real-Time detection of potassium in vitro and in vivo, Nature Communications. 8 (2017) 1–11. https://doi.org/10.1038/s41467-017-01615-z.

[25] S. Burgstaller, H. Bischof, T. Gensch, S. Stryeck, B. Gottschalk, J. Ramadani-Muja, E. Eroglu, R. Rost, S. Balfanz, A. Baumann, M. Waldeck-Weiermair, J.C. Hay, T. Madl, W.F. Graier, R. Malli, PH-Lemon, a Fluorescent Protein-Based pH Reporter for Acidic Compartments, ACS Sensors. 4 (2019) 883–891. https://doi.org/10.1021/acssensors.8b01599.

[26] K. Takemoto, T. Nagai, A. Miyawaki, M. Miura, Spatio-temporal activation of caspase revealed by indicator that is insensitive to environmental effects, Journal of Cell Biology. 160 (2003) 235–243. https://doi.org/10.1083/jcb.200207111.

[27] H. Imamura, K.P. Huynh Nhat, H. Togawa, K. Saito, R. Iino, Y. Kato-Yamada, T. Nagai,

H. Noji, Visualization of ATP levels inside single living cells with fluorescence resonance energy transfer-based genetically encoded indicators, Proceedings of the National Academy of Sciences of the United States of America. 106 (2009) 15651–15656. https://doi.org/10.1073/pnas.0904764106.

[28] A.W. Nguyen, P.S. Daugherty, Evolutionary optimization of fluorescent proteins for intracellular FRET, Nature Biotechnology. 23 (2005) 355–360. https://doi.org/10.1038/nbt1066.

[29] M. Tramier, M. Zahid, J.C. Mevel, M.J. Masse, M. Coppey-Moisan, Sensitivity of CFP/YFP and GFP/mCherry pairs to donor photobleaching on FRET determination by fluorescence lifetime imaging microscopy in living cells, Microscopy Research and Technique. 69 (2006) 933–939. https://doi.org/10.1002/jemt.20370.

[30] S. Kwok, C. Lee, S.A. Sánchez, T.L. Hazlett, E. Gratton, Y. Hayashi, Genetically encoded probe for fluorescence lifetime imaging of CaMKII activity, Biochemical and Biophysical Research Communications. 369 (2008) 519–525. https://doi.org/10.1016/j.bbrc.2008.02.070.

[31] R. Yasuda, Imaging spatiotemporal dynamics of neuronal signaling using fluorescence resonance energy transfer and fluorescence lifetime imaging microscopy, Current Opinion in Neurobiology. 16 (2006) 551–561. https://doi.org/10.1016/j.conb.2006.08.012.

[32] J. Brunker, J. Yao, J. Laufer, S.E. Bohndiek, Photoacoustic imaging using genetically encoded reporters: a review, Journal of Biomedical Optics. 22 (2017) 070901. https://doi.org/10.1117/1.jbo.22.7.070901.

[33] Y. Li, A. Forbrich, J. Wu, P. Shao, R.E. Campbell, R. Zemp, Engineering Dark Chromoprotein Reporters for Photoacoustic Microscopy and FRET Imaging, Scientific Reports. 6 (2016) 1–12. https://doi.org/10.1038/srep22129.

[34] J. Laufer, A. Jathoul, M. Pule, P. Beard, In vitro characterization of genetically expressed

absorbing proteins using photoacoustic spectroscopy, Biomedical Optics Express. 4 (2013) 2477. https://doi.org/10.1364/boe.4.002477.

[35] T. Hirasawa, R.J. Iwatate, M. Kamiya, S. Okawa, Y. Urano, M. Ishihara, Multispectral photoacoustic imaging of tumours in mice injected with an enzyme-activatable photoacoustic probe, Journal of Optics (United Kingdom). 19 (2017). https://doi.org/10.1088/2040-8978/19/1/014002.

[36] D. Razansky, M. Distel, C. Vinegoni, R. Ma, N. Perrimon, R.W. Köster, V. Ntziachristos, Multispectral opto-acoustic tomography of deep-seated fluorescent proteins in vivo, Nature Photonics. 3 (2009) 412–417. https://doi.org/10.1038/nphoton.2009.98.

[37] G.S. Filonov, A. Krumholz, J. Xia, J. Yao, L. V. Wang, V. V. Verkhusha, Deep-tissue photoacoustic tomography of a genetically encoded near-infrared fluorescent probe, Angewandte Chemie - International Edition. 51 (2012) 1448–1451. https://doi.org/10.1002/anie.201107026.

[38] S. Tzoumas, A. Nunes, N.C. Deliolanis, V. Ntziachristos, Effects of multispectral excitation on the sensitivity of molecular optoacoustic imaging, Journal of Biophotonics. 8 (2015) 629–637. https://doi.org/10.1002/jbio.201400056.

[39] A. Krumholz, D.M. Shcherbakova, J. Xia, L. V. Wang, V. V. Verkhusha, Multicontrast photoacoustic in vivo imaging using near-infrared fluorescent proteins, Scientific Reports. 4 (2014) 1–7. https://doi.org/10.1038/srep03939.

[40] R.B. Vegh, K.B. Bravaya, D.A. Bloch, A.S. Bommarius, L.M. Tolbert, M. Verkhovsky, A.I. Krylov, K.M. Solntsev, Chromophore photoreduction in red fluorescent proteins is responsible for bleaching and phototoxicity, Journal of Physical Chemistry B. 118 (2014) 4527–4534. https://doi.org/10.1021/jp500919a.

[41] J. Zhu, D.M. Shcherbakova, Y. Hontani, V. V. Verkhusha, J.T.M. Kennis, Ultrafast excited-state dynamics and fluorescence deactivation of near-infrared fluorescent proteins engineered from bacteriophytochromes, Scientific Reports. 5 (2015) 1–8.

https://doi.org/10.1038/srep12840.

[42] M. Ishihara, T. Hirasawa, Z. Le, M. Miyashita, T. Matsuda, H. Murakoshi, T. Nagai, Photoacoustic microscopy using supercontinuum light for imaging of chromoproteins in living cells, SPIE. PC11960 (2022). https://doi.org/doi.org/10.1117/12.2610957.

[43] A. Hense, K. Nienhaus, G.U. Nienhaus, Exploring color tuning strategies in red fluorescent proteins, Photochemical and Photobiological Sciences. 14 (2015) 200–212. https://doi.org/10.1039/c4pp00212a.

[44] H. Hoi, E.S. Howe, Y. Ding, W. Zhang, M.A. Baird, B.R. Sell, J.R. Allen, M.W. Davidson, R.E. Campbell, An engineered monomeric zoanthus sp. yellow fluorescent protein, Chemistry and Biology. 20 (2013) 1296–1304. https://doi.org/10.1016/j.chembiol.2013.08.008.

[45] J. Goedhart, D. Von Stetten, M. Noirclerc-Savoye, M. Lelimousin, L. Joosen, M.A. Hink, L. Van Weeren, T.W.J. Gadella, A. Royant, Structure-guided evolution of cyan fluorescent proteins towards a quantum yield of 93%, Nature Communications. 3 (2012). https://doi.org/10.1038/ncomms1738.

[46] T. Brakemann, G. Weber, M. Andresen, G. Groenhof, A.C. Stiel, S. Trowitzsch, C. Eggeling, H. Grubmüller, S.W. Hell, M.C. Wahl, S. Jakobs, Molecular basis of the light-driven switching of the photochromic fluorescent protein padron, Journal of Biological Chemistry. 285 (2010) 14603–14609. https://doi.org/10.1074/jbc.M109.086314.

[47] J.M. Battad, D.A.K. Traore, E. Byres, J. Rossjohn, R.J. Devenish, S. Olsen, M.C.J. Wilce, M. Prescott, A Green Fluorescent Protein Containing a QFG Tri-Peptide Chromophore: Optical Properties and X-Ray Crystal Structure, PLoS ONE. 7 (2012) 1–14. https://doi.org/10.1371/journal.pone.0047331.

[48] C. Chiang, C. Lin, Y. Chen, H. Tsai, Blue fl uorescent protein derived from the mutated purple chromoprotein isolated from the sea anemone Stichodactyla haddoni, 29 (2016) 523–530. https://doi.org/10.1093/protein/gzw041.

[49] O.M. Subach, I.S. Gundorov, M. Yoshimura, F. V Subach, D. Grüenwald, E.A. Souslova, D.M. Chudakov, V. Vladislav, NIH Public Access, 15 (2009) 1116–1124. https://doi.org/10.1016/j.chembiol.2008.08.006.Conversion.

[50] J. Liljeruhm, S.K. Funk, S. Tietscher, A.D. Edlund, S. Jamal, P. Wistrand-Yuen, K. Dyrhage, A. Gynnå, K. Ivermark, J. Lövgren, V. Törnblom, A. Virtanen, E.R. Lundin, E. Wistrand-Yuen, A.C. Forster, Engineering a palette of eukaryotic chromoproteins for bacterial synthetic biology, Journal of Biological Engineering. 12 (2018) 1–10. https://doi.org/10.1186/s13036-018-0100-0.

[51] H. Shinoda, Y. Ma, R. Nakashima, K. Sakurai, T. Matsuda, T. Nagai, Acid-Tolerant Monomeric GFP from Olindias formosa, Cell Chemical Biology. 25 (2018) 330-338.e7. https://doi.org/10.1016/j.chembiol.2017.12.005.

[52] H. Shinoda, K. Lu, R. Nakashima, T. Wazawa, K. Noguchi, T. Matsuda, T. Nagai, Acid-Tolerant Reversibly Switchable Green Fluorescent Protein for Super-resolution Imaging under Acidic Conditions, Cell Chemical Biology. 26 (2019) 1469-1479.e6. https://doi.org/10.1016/j.chembiol.2019.07.012.

[53] L. Zhai, R. Nakashima, H. Shinoda, Y. Ike, T. Matsuda, T. Nagai, Structure-based analysis and evolution of a monomerized red-colored chromoprotein from the Olindias formosa jellyfish, Protein Science. 31 (2022) 1–12. https://doi.org/10.1002/pro.4285.

[54] K. Takemoto, T. Matsuda, N. Sakai, D. Fu, M. Noda, S. Uchiyama, I. Kotera, Y. Arai, M. Horiuchi, K. Fukui, T. Ayabe, F. Inagaki, H. Suzuki, T. Nagai, SuperNova, a monomeric photosensitizing fluorescent protein for chromophore-assisted light inactivation, Scientific Reports. 3 (2013) 1–7. https://doi.org/10.1038/srep02629.

[55] W. Kabsch, XDS, Acta Crystallographica Section D Biological Crystallography. D66 (2010) 125–132. https://doi.org/10.1107/s090744499201028x.

[56] A.A. Vagin, R.A. Steiner, A.A. Lebedev, L. Potterton, S. McNicholas, F. Long, G.N. Murshudov, REFMAC5 dictionary: Organization of prior chemical knowledge and

guidelines for its use, Acta Crystallographica Section D: Biological Crystallography. D60 (2004) 2184–2195. https://doi.org/10.1107/S0907444904023510.

[57] M.D. Winn, C.C. Ballard, K.D. Cowtan, E.J. Dodson, P. Emsley, P.R. Evans, R.M. Keegan, E.B. Krissinel, A.G.W. Leslie, A. McCoy, S.J. McNicholas, G.N. Murshudov, N.S. Pannu, E.A. Potterton, H.R. Powell, R.J. Read, A. Vagin, K.S. Wilson, Overview of the CCP4 suite and current developments, Acta Crystallographica Section D: Biological Crystallography. 67 (2011) 235–242. https://doi.org/10.1107/S0907444910045749.

[58] P. Emsley, K. Cowtan, Coot: Model-building tools for molecular graphics, Acta Crystallographica Section D: Biological Crystallography. 60 (2004) 2126–2132. https://doi.org/10.1107/S0907444904019158.

[59] Z. Sun, Q. Liu, G. Qu, Y. Feng, M.T. Reetz, Utility of B-Factors in Protein Science: Interpreting Rigidity, Flexibility, and Internal Motion and Engineering Thermostability, Chemical Reviews. (2019). https://doi.org/10.1021/acs.chemrev.8b00290.

[60] A.B. Cubitt, R. Heim, S.R. Adams, A.E. Boyd, L.A. Gross, R.Y. Tsien, Understanding, improving and using green fluorescent proteins, Trends in Biochemical Sciences. 20 (1995) 448–455. https://doi.org/10.1016/S0968-0004(00)89099-4.

[61] D.P. Barondeau, J.A. Tainer, E.D. Getzoff, Structural evidence for an enolate intermediate in GFP fluorophore biosynthesis, Journal of the American Chemical Society. 128 (2006) 3166–3168. https://doi.org/10.1021/ja0552693.

[62] N. V. Pletneva, V.Z. Pletnev, K.A. Lukyanov, N.G. Gurskaya, E.A. Goryacheva, V.I. Martynov, A. Wlodawer, Z. Dauter, S. Pletnev, Structural evidence for a dehydrated intermediate in green fluorescent protein chromophore biosynthesis, Journal of Biological Chemistry. 285 (2010) 15978–15984. https://doi.org/10.1074/jbc.M109.092320.

[63] L. Muslinkina, A. Roldán-Salgado, P. Gaytán, V.R. Juárez-González, E. Rudiño, N. Pletneva, V. Pletnev, Z. Dauter, S. Pletnev, Structural Factors Enabling Successful

GFP-Like Proteins with Alanine as the Third Chromophore-Forming Residue, Journal of Molecular Biology. 431 (2019) 1397–1408. https://doi.org/10.1016/j.jmb.2019.02.013.

[64] T.D. Craggs, Green fluorescent protein: Structure, folding and chromophore maturation, Chemical Society Reviews. 38 (2009) 2865–2875. https://doi.org/10.1039/b903641p.

[65] C. Don Paul, C. Kiss, D.A.K. Traore, L. Gong, M.C.J. Wilce, R.J. Devenish, A. Bradbury, M. Prescott, Phanta: A Non-Fluorescent Photochromic Acceptor for pcFRET, PLoS ONE. 8 (2013) 1–9. https://doi.org/10.1371/journal.pone.0075835.

[66] C. Don Paul, D.A.K. Traore, S. Olsen, R.J. Devenish, D.W. Close, T.D.M. Bell, A. Bradbury, M.C.J. Wilce, M. Prescott, X-ray crystal structure and properties of phanta, a weakly fluorescent photochromic GFP-like protein, PLoS ONE. 10 (2015) 1–23. https://doi.org/10.1371/journal.pone.0123338.

[67] E. Padan, E. Bibi, M. Ito, T.A. Krulwich, Alkaline pH homeostasis in bacteria: New insights, Biochimica et Biophysica Acta - Biomembranes. 1717 (2005) 67–88. https://doi.org/10.1016/j.bbamem.2005.09.010.

[68] A. Brune, M. Kühl, pH profiles of the extremely alkaline hindguts of soil-feeding termites (Isoptera: Termitidae) determined with microelectrodes, Journal of Insect Physiology. 42 (1996) 1121–1127. https://doi.org/10.1016/S0022-1910(96)00036-4.

[69] T. Lemke, U. Stingl, M. Egert, M.W. Friedrich, A. Brune, Physicochemical Conditions and Microbial Activities in the Highly Alkaline Gut of the Humus-Feeding Larva of Pachnoda ephippiata (Coleoptera: Scarabaeidae), Applied and Environmental Microbiology. 69 (2003) 6650–6658. https://doi.org/10.1128/AEM.69.11.6650-6658.2003.

[70] H. Wang, T. Takano, S. Liu, Screening and evaluation of saline⇓alkaline tolerant germplasm of rice (Oryza sativa l.) in soda saline⇓alkali soil, Agronomy. 8 (2018) 2–3. https://doi.org/10.3390/agronomy8100205.

[71] L.Y. Chen, D.Q. Shi, W.J. Zhang, Z.S. Tang, J. Liu, W.C. Yang, The Arabidopsis alkaline

ceramidase TOD1 is a key turgor pressure regulator in plant cells, Nature Communications. 6 (2015) 1–10. https://doi.org/10.1038/ncomms7030.

[72] R.K.W. Chee, Y. Li, W. Zhang, R.E. Campbell, In vivo photoacoustic difference-spectra imaging of bacteria using photoswitchable chromoproteins, Journal of Biomedical Optics. 23 (2018) 1. https://doi.org/10.1117/1.jbo.23.10.106006.

[73] J. Yao, A.A. Kaberniuk, L. Li, D.M. Shcherbakova, R. Zhang, L. Wang, G. Li, V. V. Verkhusha, L. V. Wang, Multiscale photoacoustic tomography using reversibly switchable bacterial phytochrome as a near-infrared photochromic probe, Nature Methods. 13 (2015) 67–73. https://doi.org/10.1038/nmeth.3656.

[74] R. Gao, F. Liu, W. Liu, S. Zeng, J. Chen, R. Gao, L. Wang, C. Fang, Background-suppressed tumor-targeted photoacoustic imaging using bacterial carriers Rongkang, Pnas. 119 (2022) 1–11. https://doi.org/10.1073/pnas.2121982119/-/DCSupplemental.Published.

[75] A.D. Kummer, J. Wiehler, H. Rehaber, C. Kompa, B. Steipe, M.E. Michel-Beyerle, Effects of threonine 203 replacements on excited-state dynamics and fluorescence properties of the green fluorescent protein (GFP), Journal of Physical Chemistry B. 104 (2000) 4777–4781. https://doi.org/10.1021/jp9942522.

[76] C.Y. Lin, M.G. Romei, L.M. Oltrogge, I.I. Mathews, S.G. Boxer, Unified Model for Photophysical and Electro-Optical Properties of Green Fluorescent Proteins, Journal of the American Chemical Society. 141 (2019) 15250–15265. https://doi.org/10.1021/jacs.9b07152.

[77] M.G. Romei, C. Lin, I.I. Mathews, S.G. Boxer, Electrostatic control of photoisomerization pathways in proteins, Science. 367 (2020) 76–79.

[78] G.E.O. Borgstahl, D.W.R. Williams, E.D. Getzoff, 1.4 Å Structure of Photoactive Yellow Protein, a Cytosolic Photoreceptor: Unusual Fold, Active Site, and Chromophore, Biochemistry. 34 (1995) 6278–6287. https://doi.org/10.1021/bi00019a004.

[79] M. Yoda, H. Houjou, Y. Inoue, M. Sakurai, Spectral tuning of photoactive yellow protein. Theoretical and experimental analysis of medium effects on the absorption spectrum of the chromophore, Journal of Physical Chemistry B. 105 (2001) 9887–9895. https://doi.org/10.1021/jp011722v.

[80] M. Sugishima, N. Tanimoto, K. Soda, N. Hamada, F. Tokunaga, K. Fukuyama, Structure of photoactive yellow protein (PYP) E46Q mutant at 1.2 Å resolution suggests how Glu46 controls the spectroscopic and kinetic characteristics of PYP, Acta Crystallographica Section D: Biological Crystallography. 60 (2004) 2305–2309. https://doi.org/10.1107/S0907444904024084.

[81] A.F. Philip, K.T. Eisenman, G.A. Papadantonakis, W.D. Hoff, Functional tuning of photoactive yellow protein by active site residue 46, Biochemistry. 47 (2008) 13800–13810. https://doi.org/10.1021/bi801730y.

[82] H.W. Ai, J.N. Henderson, S.J. Remington, R.E. Campbell, Directed evolution of a monomeric, bright and photostable version of Clavularia cyan fluorescent protein: Structural characterization and applications in fluorescence imaging, Biochemical Journal. 400 (2006) 531–540. https://doi.org/10.1042/BJ20060874.

[83] R. Heim, R.Y. Tsien, Engineering green fluorescent protein for improved brightness, longer wavelengths and fluorescence resonance energy transfer, Current Biology. 6 (1996) 178–182. https://doi.org/10.1016/S0960-9822(02)00450-5.

[84] G.J. Kremers, J. Goedhart, E.B. Van Munster, T.W.J. Gadella, Cyan and yellow super fluorescent proteins with improved brightness, protein folding, and FRET förster radius, Biochemistry. 45 (2006) 6570–6580. https://doi.org/10.1021/bi0516273.

[85] M.A. Rizzo, D.W. Piston, High-contrast imaging of fluorescent protein FRET by fluorescence polarization microscopy, Biophysical Journal. 88 (2005) L14–L16. https://doi.org/10.1529/biophysj.104.055442.

[86] M.L. Markwardt, G.J. Kremers, C.A. Kraft, K. Ray, P.J.C. Cranfill, K.A. Wilson, R.N. Day,

R.M. Wachter, M.W. Davidson, M.A. Rizzo, An improved cerulean fluorescent protein with enhanced brightness and reduced reversible photoswitching, PLoS ONE. 6 (2011). https://doi.org/10.1371/journal.pone.0017896.

[87] J.N. Henderson, S.J. Remington, Crystal structures and mutational analysis of amFP486, a cyan flourescent protein from Anemonia majano, Proceedings of the National Academy of Sciences of the United States of America. 102 (2005) 12712–12717. https://doi.org/10.1073/pnas.0502250102.

[88] H. Zhao, W. Zha, In vitro “sexual” evolution through the PCR-based staggered extension process (StEP), Nature Protocols. 1 (2006) 1865–1871. https://doi.org/10.1038/nprot.2006.309.

[89] C.Y. Chiang, Y.L. Chen, H.J. Tsai, Different Visible Colors and Green Fluorescence Were Obtained from the Mutated Purple Chromoprotein Isolated from Sea Anemone, Marine Biotechnology. 16 (2014) 436–446. https://doi.org/10.1007/s10126-014-9563-2.

[90] V.Z. Pletnev, N. V. Pletneva, K.S. Sarkisyan, A.S. Mishin, K.A. Lukyanov, E.A. Goryacheva, R.H. Ziganshin, Z. Dauter, S. Pletnev, Structure of the green fluorescent protein NowGFP with an anionic tryptophan-based chromophore, Acta Crystallographica Section D: Biological Crystallography. 71 (2015) 1699–1707. https://doi.org/10.1107/S1399004715010159.

[91] G. Gotthard, D. Von Stetten, D. Clavel, M. Noirclerc-Savoye, A. Royant, Chromophore Isomer Stabilization Is Critical to the Efficient Fluorescence of Cyan Fluorescent Proteins, Biochemistry. 56 (2017) 6418–6422. https://doi.org/10.1021/acs.biochem.7b01088.

[92] H.W. Ai, S.G. Olenych, P. Wong, M.W. Davidson, R.E. Campbell, Hue-shifted monomeric variants of Clavularia cyan fluorescent protein: Identification of the molecular determinants of color and applications in fluorescence imaging, BMC Biology. 6 (2008) 1–13. https://doi.org/10.1186/1741-7007-6-13.

[93] D.R. Coates, J.M. Chin, S.T.L. Chung, Highly sensitive and quantitative FRET-FLIM imaging in single dendritic spines using improved non-radiative YFP, Bone. 23 (2011) 1–7. https://doi.org/10.1007/s11068-008-9024-9.Highly.

[94] A.C.E. Shibata, H.H. Ueda, K. Eto, M. Onda, A. Sato, T. Ohba, J. Nabekura, H. Murakoshi, Photoactivatable CaMKII induces synaptic plasticity in single synapses, Nature Communications. 12 (2021) 1–15. https://doi.org/10.1038/s41467-021-21025-6.

[95] B.T. Bajar, E.S. Wang, S. Zhang, M.Z. Lin, J. Chu, A guide to fluorescent protein FRET pairs, Sensors (Switzerland). 16 (2016) 1–24. https://doi.org/10.3390/s16091488.

[96] K. Sugiura, T. Nagai, Extension of the short wavelength side of fluorescent proteins using hydrated chromophores, and its application, Communications Biology. 5 (2022) 1–6. https://doi.org/10.1038/s42003-022-04153-7.

[97] W. Tomosugi, T. Matsuda, T. Tani, T. Nemoto, I. Kotera, K. Saito, K. Horikawa, T. Nagai, An ultramarine fluorescent protein with increased photostability and pH insensitivity, Nature Methods. 6 (2009) 351–353. https://doi.org/10.1038/nmeth.1317.

[98] A. Manuscript, Transient mammilian cell transfection with PEI, Changes. 29 (2012) 997–1003. https://doi.org/10.1016/B978-0-12-418687-3.00018-5.Transient.

[99] R. Yasuda, Studying signal transduction in single dendritic spines, Cold Spring Harbor Perspectives in Biology. 4 (2012). https://doi.org/10.1101/cshperspect.a005611.

[100] K. Fushimi, R. Narikawa, Optogenetic Imaging of Protein Activity 18 Using Two-Photon Fluorescence Lifetime Imaging Microscopy, 2021. https://doi.org/10.1007/978-981-15-8763-4_10.

[101] T.T. Yang, P. Sinai, G. Green, P.A. Kitts, Y.T. Chen, L. Lybarger, R. Chervenak, G.H. Patterson, D.W. Piston, S.R. Kain, Improved fluorescence and dual color detection with enhanced blue and green variants of the green fluorescent protein, Journal of Biological Chemistry. 273 (1998) 8212–8216. https://doi.org/10.1074/jbc.273.14.8212.

[102] A. Miyawaki, R.Y. Tsien, Monitoring protein conformations and interactions by

fluorescence resonance energy transfer between mutants of green fluorescent protein, Methods in Enzymology. 327 (2000) 472–500. https://doi.org/10.1016/S0076-6879(00)27297-2.

[103] T. Ohashi, S.D. Galiacy, G. Briscoe, H.P. Erickson, An experimental study of GFP-based FRET, with application to intrinsically unstructured proteins, Protein Science. 16 (2007) 1429–1438. https://doi.org/10.1110/ps.072845607.

[104] P. Trigo-Mourino, T. Thestrup, O. Griesbeck, C. Griesinger, S. Becker, Dynamic tuning of FRET in a green fluorescent protein biosensor, Science Advances. 5 (2019) 1–9. https://doi.org/10.1126/sciadv.aaw4988.

[105] T. Torcellan, J. Stolp, T. Chtanova, In vivo imaging sheds light on immune cell migration and function in cancer, Frontiers in Immunology. 8 (2017) 1–7. https://doi.org/10.3389/fimmu.2017.00309.

[106] L. Perrin, B. Bayarmagnai, B. Gligorijevic, Frontiers in intravital multiphoton microscopy of cancer, Cancer Reports. (2019) 1–22. https://doi.org/10.1002/cnr2.1192.

[107] A. Sun, Y. Ji, Y. Li, W. Xie, Z. Liu, T. Li, T. Jin, W. Qi, K. Li, C. Wu, L. Xi, Multicolor Photoacoustic Volumetric Imaging of Subcellular Structures, ACS Nano. 16 (2022) 3231–3238. https://doi.org/10.1021/acsnano.1c11103.

ACKNOWLEDGEMENTS

I would want to use this opportunity to show my appreciation for everybody who has been there for me during my PhD studies. Firstly, I would like to acknowledge the invaluable help of my supervisor Professor Takeharu Nagai with my deep and sincere gratitude. I acquired a lot under his enthusiastic and professional guidance during my years of researcher life. Without his incredibly helpful direction, financial backing, encouragement, kindness, and patience, I would never have been capable of completing my thesis. I am unable to adequately express my gratitude in words.

I am also indebted to Assistant Professor Tomoki Matsuda who gave me continuous encouragement and useful instruction all through my research study. His meticulous and serious attitude to science is also my role model and motivation for progress in my future research life.

My heartfelt thanks go to Assistant Professor Ryousuke Nakashima for his support in the crystallography experiment. Every encouragement is the key to the success of my crystallization experiment. I wish to express my appreciation to Professor Miya Ishihara from National Defense Medical College, who supported the photoacoustic imaging data. The rigorous attitude towards the experiment makes me admire. Furthermore, I also would like to thank Associate Professor Hideji Murakoshi from National Institute for Physiological Sciences, and his student Hiromo Ueda for the support of two-photon FLIM measurement and data collection.

My profound appreciation also extends to Nagai laboratory secretaries for their graciousness and kindly assistance in preparing the documents, Kazunori Sugiura for the support of Sumire information. Furthermore, this work would not have been possible without the help of Yoshimasa Ike as my student tutor who was the one who discovered ofCP and developed it into ofCP2. Finally, I must conclude by expressing my deepest thanks to my family members, particularly my father Zhengsun Zhai, my momther Yarong Huang, relatives, friends. XieXie!

LIST OF ACADEMIC ACCOMPLISHMENTS

Publications

1. Zhai L, Nakashima R, Shinoda H, Ike Y, Matsuda T, Nagai T. Structure-based analysis and evolution of a monomerized red-colored chromoprotein from the *Olindias formosa* jellyfish. Protein Sci. 2022;31(5):e4285. doi:10.1002/pro.4285

Poster presentations

1. Zhai L, Nakashima R, Shinoda H, Ike Y, Matsuda T and Nagai T. The problem of protein crystallization: A case study of crystallization of novel chromoprotein from flower hat jelly fish. The 23rd SANKEN International Symposium, 2020.1, Japan

2. Zhai L, Nakashima R, Shinoda H, Ike Y, Matsuda T and Nagai T. Structure-based analysis and evolution of a monomerized red-color chromoprotein from jellyfish *Olindias formosa* for bioimaging. The 59th Annual Meeting of the Biophysical Society of Japan, 2021/11, Japan

3. Zhai L, Nakashima R, Matsuda T and Nagai T. Structure mechanism for color tuning of red-colored chromoprotein, R-Velour. The 60th Annual Meeting of the Biophysical Society of Japan, 2022/09, Japan

4. Miya Ishihara, Takeshi Hirasawa, Zhai Le, Manami Miyashita, Tomoki Matsuda, Hideji Murakoshi, and Takeharu Nagai "Photoacoustic microscopy using supercontinuum light for imaging of chromoproteins in living cells", Proc. SPIE PC11960, Photons Plus Ultrasound: Imaging and Sensing 2022, PC119601R (7 March 2022); https://doi.org/10.1117/12.2610957